Supporting Information

Experimental and computational insights into the mechanism of FLP mediated selective C–F bond activation

Richa Gupta†, Dániel Csókás†, Kenneth Lye and Rowan D. Young*

Department of Chemistry, National University of Singapore, 3 Science Drive 3, Singapore 117543

**Corresponding Author, †Equal contribution*

Table of Contents

Experimental

General information

Experiments were performed under inert conditions using standard Schlenk techniques or a glove box (Vacuum Atmospheres Company) as appropriate. Subsequent manipulation of air-stable products was carried out under ambient conditions. Dichloromethane (DCM) and *n*-hexane were purified using an LC Technology Solution Inc. SP-1 Solvent Purification System, deoxygenated and stored over 4 Å molecular sieves prior to use. Chloroform-d ($CDCl_3$), 1,2-dichlorobenzene (1,2-DCB) solvents were stirred over CaH_2 at room temperature under nitrogen atmosphere overnight prior to distillation under reduced pressure. Tetrahydrofuran (THF) was distilled under nitrogen from sodium and benzophenone and stored over 4 Å molecular sieves. Glassware for reactions were oven-dried overnight prior to use in experiments. Column chromatography using silica (230-400 mesh) was carried out using analytical grade eluent mixtures of *n*-hexane and ethyl acetate. ^{1}H, ^{13}C, ^{19}F and ^{31}P NMR spectra were all carried out at 298 K and recorded using Bruker AV-400 and AV-500 spectrometers. The chemical shifts (δ) for ^{1}H and ^{13}C spectra are given in ppm relative to solvent signals, and $^{31}P\{^{1}H\}$, $^{19}F\{^{1}H\}$ and $^{11}B\{^{1}H\}$ spectra were referenced to external 85% H_3PO_4, $CFCl_3$ or $BF_3.OEt_2$ standards, respectively. Data are reported as follows: chemical shift, multiplicity (s = singlet, d = doublet, t = triplet, q = quartet, m = multiplet, br = broad), coupling constants (Hz) and integration. HRMS spectra were obtained using an Agilent Technologies 6230 TOF MS (ESI-TOF) and a Bruker micrOTOF-Q II (APCI-TOF).

The starting materials $B(C_6F_5)_3$[1] (BCF) and 2,4,6-triphenylpyridine[2] (TPPy) were prepared using reported methods. Tris(*ortho*-tolyl)phosphine ($P(o\text{-}Tol)_3$ or PTol) and tetrahydrothiophene (THT) were purchased commercially and used as received. Fluorocarbon substrates **1**-**3** were purchased from commercial sources or prepared using reported methods.[3] All other reagents were obtained commercially and used as received.

Order in TPPy

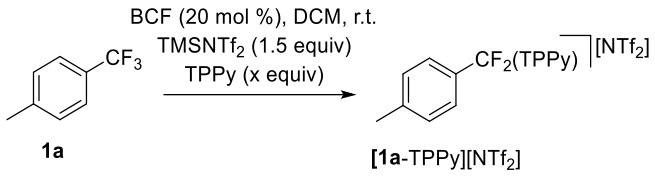

BCF (0.2 equiv) and TPPy (0.5, 1.0, 1.5 or 2.0 equiv) were dissolved in DCM (0.3 mL). The solution was added to a J. Young's NMR tube containing **1a** (24.0 mg, 0.15 mmol, 0.382 M) and $TMSNTf_2$ (1.5 equiv) was added. The reaction was monitored at 298 K by ^{19}F NMR spectroscopy to determine the concentration of the product [**1a**-TPPy][NTf_2] and the remaining starting material (**1a**).

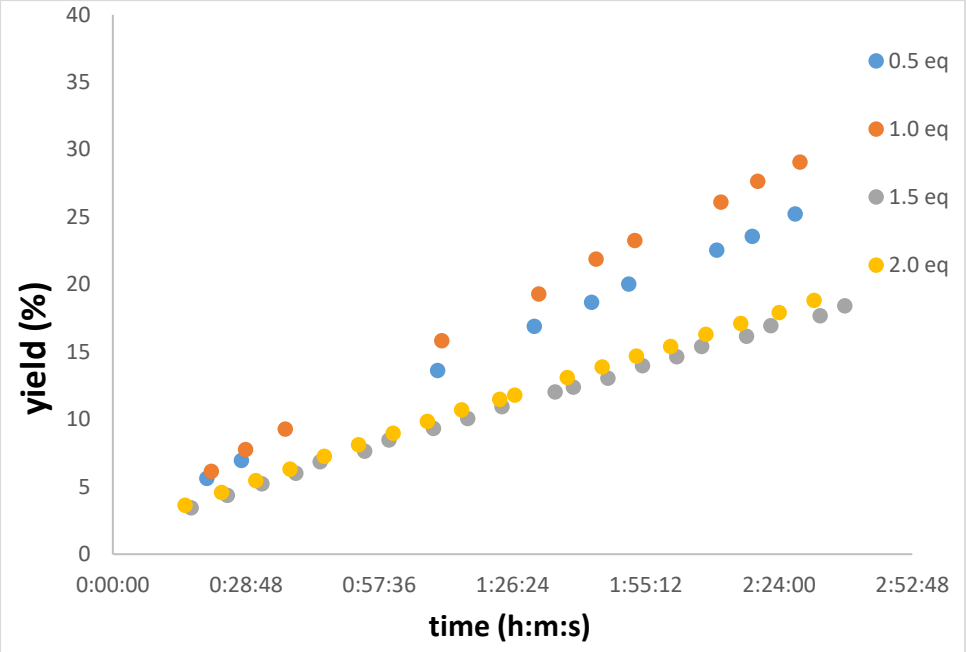

Figure S1. Effect of TPPy concentration on reaction rate with **1a**.

Eq. TPPy	k_{obs}
0.50	$9.72x10^{-06}$
1.0	$1.1x10^{-05}$
1.50	$6.65x10^{-06}$
2.0	$7.05x10^{-06}$

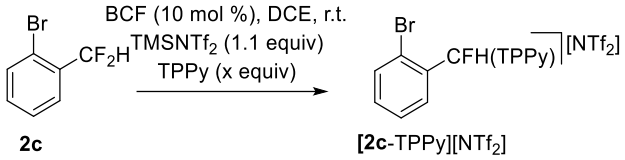

2c **[2c**-TPPy][NTf_2]

BCF (0.1 equiv) and TPPy (0.5, 1.1, 1.5 or 1.75 equiv) were dissolved in DCE (0.6 mL). The solution was added to a J. Young's NMR tube containing **2c** (12.4 mg, 0.06 mmol, 0.096 M) and $TMSNTf_2$ (1.1 equiv) was added. The reaction was monitored at 298 K by ^{19}F NMR spectroscopy to determine the concentration of the product [**2c**-TPPy][NTf_2] and the remaining starting material (**2c**).

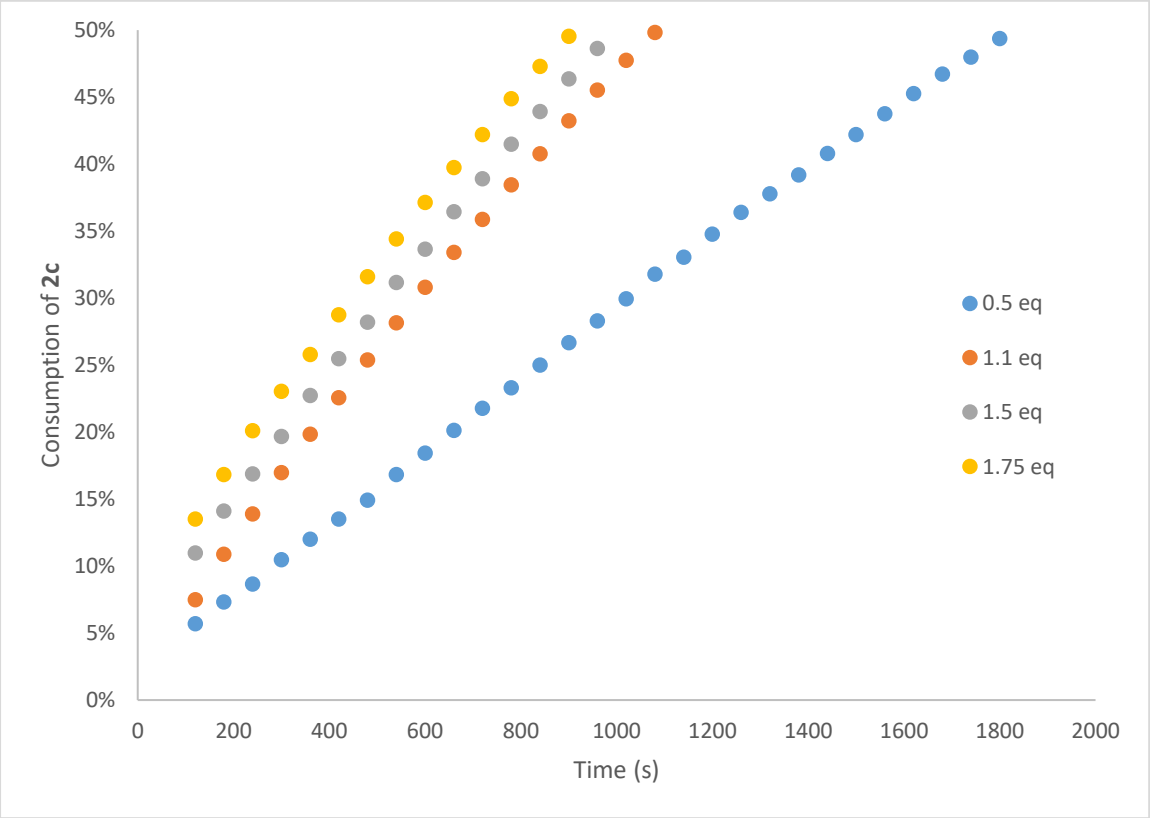

Figure S2. Effect of TPPy concentration on reaction rate with **2c**.

TPPy eq.	k_{obs}
0.50	$2.36x10^{-05}$
1.10	$4.42x10^{-05}$
1.50	$4.40x10^{-05}$
1.75	$4.48x10^{-05}$

Note: The rate of conversion of **2c**-NTf_2 to [**2c**-TPPy][NTf_2] is base dependent and becomes significantly slow (as compared to C-F activation) with 0.5 equiv. TPPy.

Order in P(o-Tol)$_3$

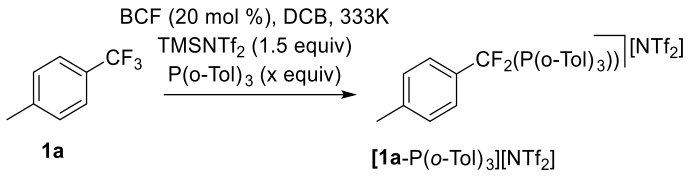

1a [**1a**-P(*o*-Tol)$_3$][NTf$_2$]

BCF (0.2 equiv) and P(*o*-Tol)$_3$ (0.5, 1.0, 1.5 or 2.0 equiv) were dissolved in DCB (0.35 mL). The solution was added to a J. Young's NMR tube containing **1a** (24.0 mg, 0.15 mmol, 0.348 M) and TMSNTf$_2$ (1.5 equiv) was added. The reaction was monitored at 333 K by ^{19}F NMR spectroscopy to determine the concentration of the product [**1a**-P(*o*-Tol)$_3$][NTf$_2$] and the remaining starting material (**1a**).

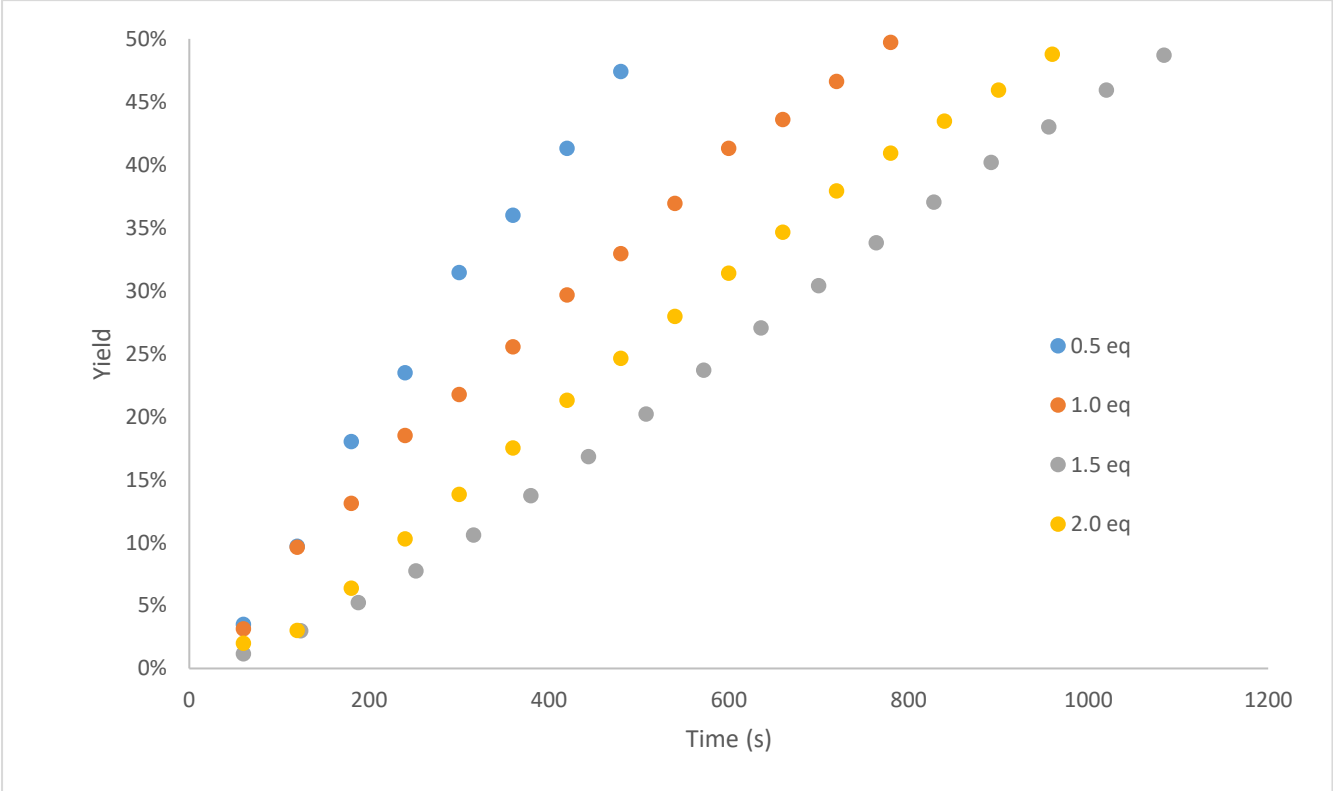

Figure S3a. Effect of P(*o*-Tol)$_3$ concentration on reaction rate with **1a** in DCB.

Eq. P(o-Tol)$_3$	k_{obs}
0.5	3.42×10^{-04}
1.0	2.36×10^{-04}
1.5	1.59×10^{-04}
2.0	1.99×10^{-04}

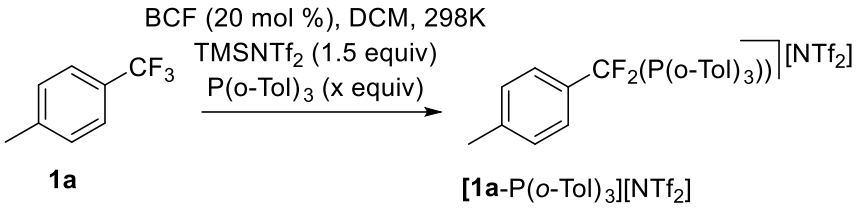

BCF (0.2 equiv) and P(*o*-Tol)$_3$ (0.5, 1.0, 1.5 or 2.0 equiv) were dissolved in DCM (0.35 mL). The solution was added to a J. Young's NMR tube containing **1a** (24.01 mg, 0.15 mmol) and $TMSNTf_2$ (1.5 equiv) was added. The reaction was monitored at 298 K by ^{19}F NMR spectroscopy to determine the concentration of the product [**1a**-P(*o*-Tol)$_3$][NTf_2] and the remaining starting material (**1a**).

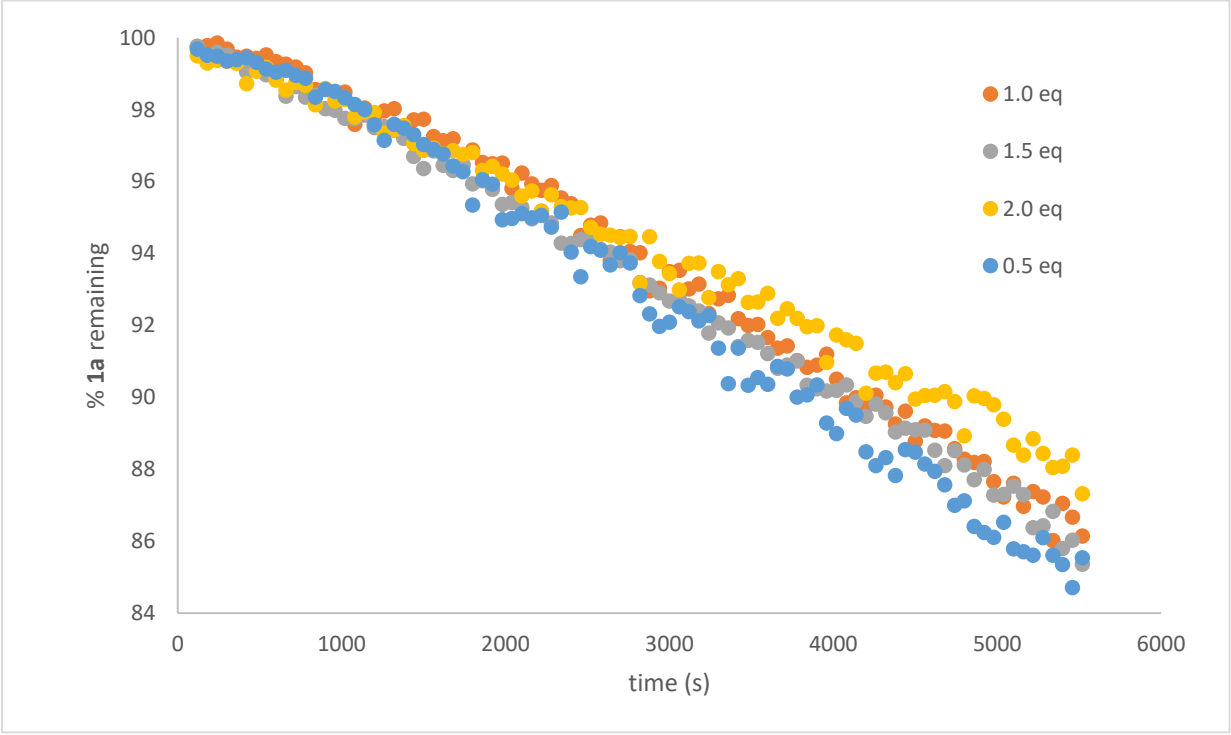

Figure S3b. Effect of P(*o*-Tol)$_3$ concentration on reaction rate with **1a** in DCM.

Eq. P(o-Tol)$_3$	k_{obs}
0.5	1.03×10^{-05}
1.0	9.37×10^{-06}
1.5	9.16×10^{-06}
2.0	7.81×10^{-06}

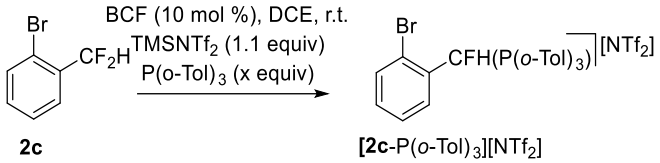

2c **[2c**-P(*o*-Tol)$_3$][NTf$_2$]

BCF (0.1 equiv) and P(*o*-Tol)$_3$ (0.6, 1.1, 1.6 or 2.1 equiv) were dissolved in DCM (0.6 mL). The solution was added to a J. Young's NMR tube containing **2c** (12.4 mg, 0.06 mmol, 0.096 M) and TMSNTf$_2$ (1.1 equiv) was added. The reaction was monitored at 298 K by ^{19}F NMR spectroscopy to determine the concentration of the product [**2c**-P(*o*-Tol)$_3$][NTf$_2$] and the remaining starting material (**2c**).

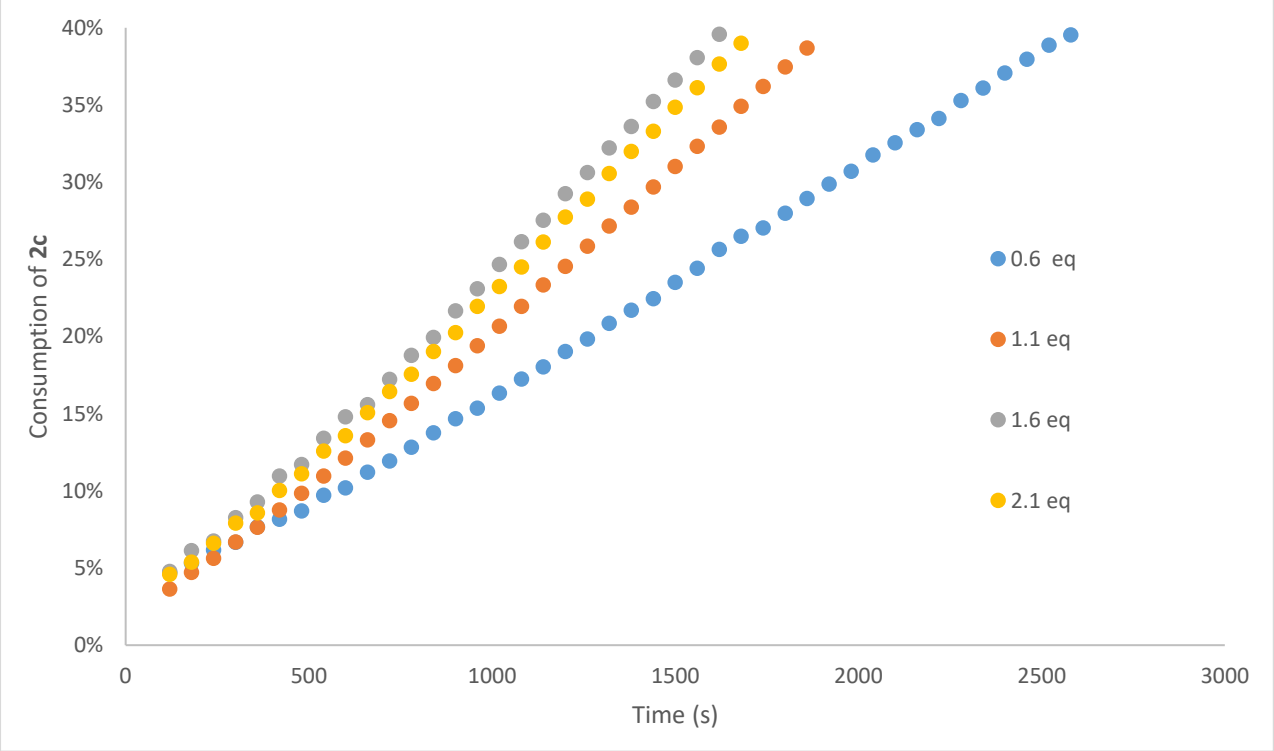

Figure S4. Effect of P(*o*-Tol)$_3$ concentration on reaction rate with **2c**.

Eq P(o-Tol)$_3$	k_{obs}
0.60	1.40×10^{-05}
1.10	2.00×10^{-05}
1.60	2.15×10^{-05}
2.10	2.20×10^{-05}

Order in THT

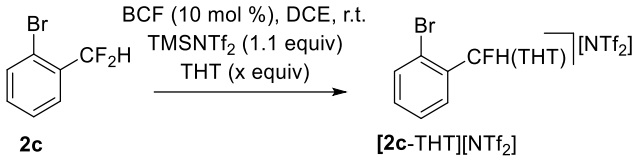

2c **[2c**-THT][NTf_2]

BCF (0.1 equiv) and THT (0.5, 1.1 or 1.5 equiv) were dissolved in DCE (0.6 mL). The solution was added to a J. Young's NMR tube containing **2c** (12.4 mg, 0.06 mmol) and $TMSNTf_2$ (1.1 equiv) was added. The reaction was monitored at 298 K by ^{19}F NMR spectroscopy to determine the concentration of the product [**2c**-THT][NTf_2] and the remaining starting material (**2c**).

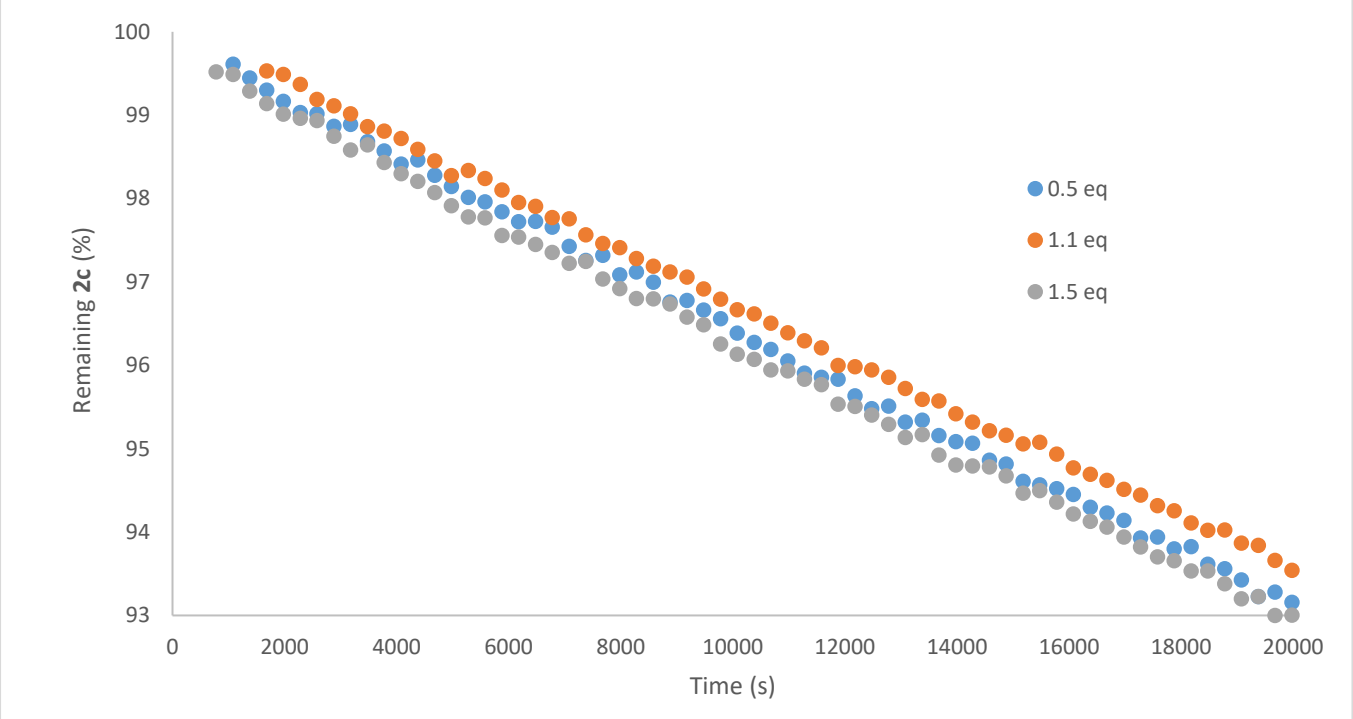

Figure S5. Effect of THT concentration on reaction rate with **2c**.

Eq. of THT	k_{obs}
0.5	$3.14x10^{-07}$
1.1	$3.05x10^{-07}$
1.5	$3.04x10^{-07}$

Order in Me_3SiNTf_2

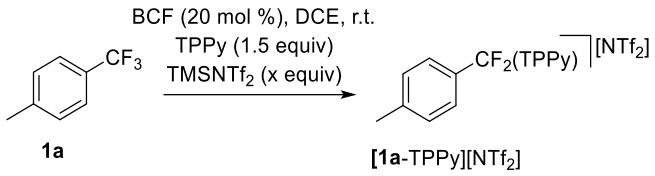

1a **[1a**-TPPy][NTf_2]

BCF (0.2 equiv) and TPPy (1.5 equiv) were dissolved in DCE (0.3 mL). The solution was added to a J. Young's NMR tube containing **1a** (24.0 mg, 0.15 mmol) and $TMSNTf_2$ (0.5, 1.0, 1.5 or 2.0 equiv) was added. The reaction was monitored at 298 K by ^{19}F NMR spectroscopy to determine the concentration of the product [**1a**-TPPy][NTf_2] and the remaining starting material (**1a**). Note: due to constant DCE volume used, the reaction molarity was diluted slightly with addition of extra $TMSNTf_2$ from 0.42 M (0.5 equiv $TMSNTf_2$) to 0.35 M (2.0 equiv $TMSNTf_2$) resulting in a slight observed rate reduction.

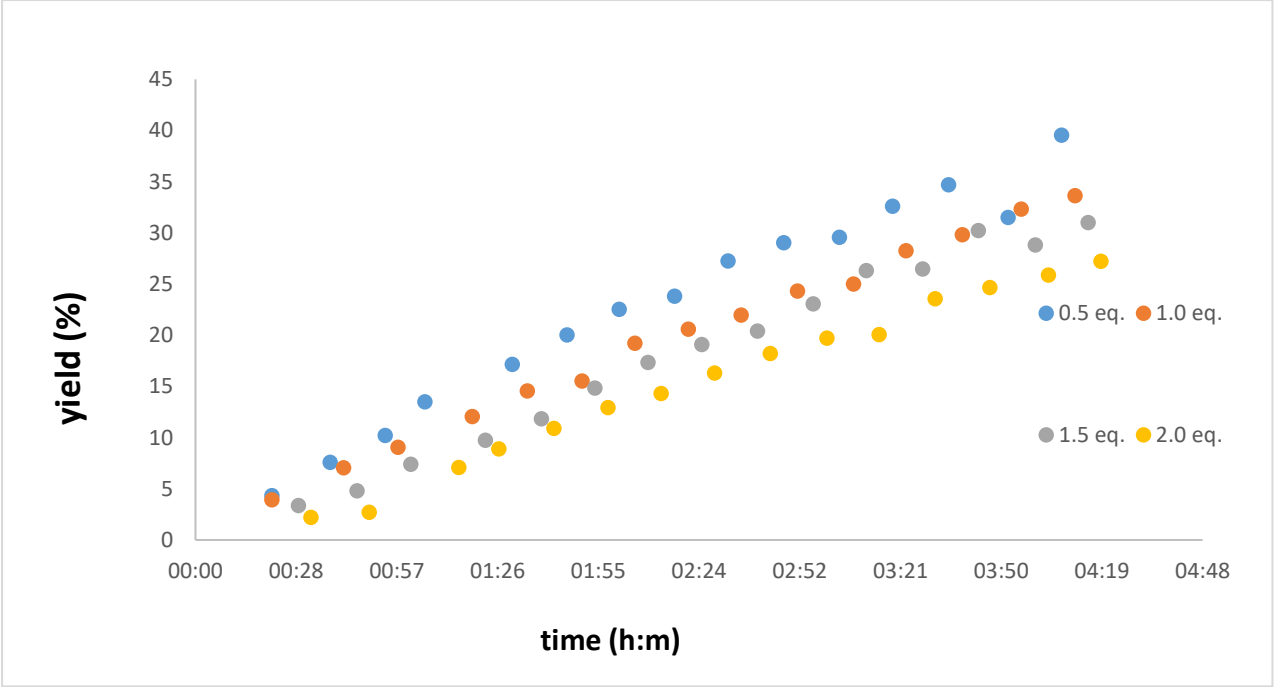

Figure S6. Effect of $TMSNTf_2$ concentration on reaction rate with **FLP-I** and **1a**.

Eq $TMSNTf_2$	k_{obs}
0.5	$1.38x10^{-04}$
1.0	$1.23x10^{-04}$
1.5	$1.25x10^{-04}$
2.0	$1.09x10^{-04}$

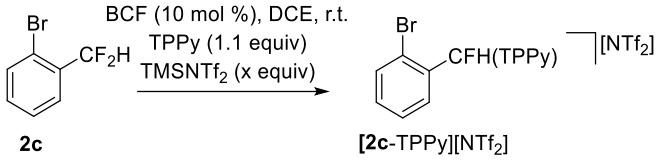

2c **[2c**-TPPy][NTf_2]

BCF (0.1 equiv) and TPPy (1.1 equiv) were dissolved in DCE (0.3 mL). The solution was added to a J. Young's NMR tube containing **2c** (12.4 mg, 0.6 mmol, 0.096 M) and $TMSNTf_2$ (0.6, 1.1, 1.6 or 2.1 equiv) was added. Additional DCE was added to make the total reaction volume 0.625 mL. The reaction was monitored at 298 K by ^{19}F NMR spectroscopy to determine the concentration of the product [**2c**-TPPy][NTf_2] and the remaining starting material (**2c**).

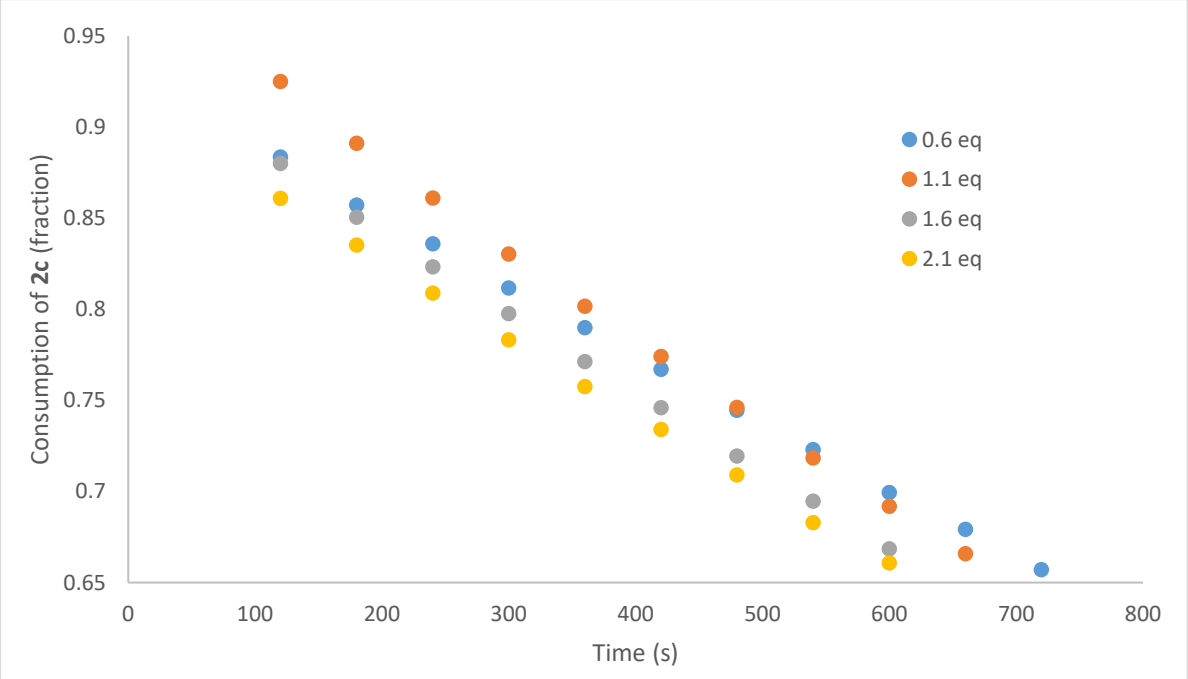

Figure S7. Effect of $TMSNTf_2$ concentration on reaction rate with **FLP-I** and **2c**.

Eq $TMSNTf_2$	k_{obs}
0.60	$3.42x10^{-05}$
1.10	$4.32x10^{-05}$
1.60	$4.02x10^{-05}$
2.10	$3.84x10^{-05}$

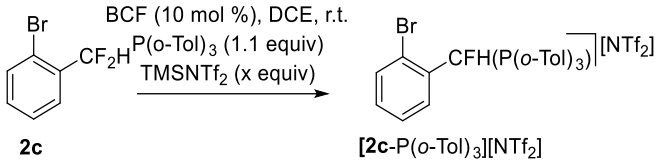

2c **[2c**-P(*o*-Tol)$_3$][NTf$_2$]

BCF (0.1 equiv) and P(*o*-Tol)$_3$ (1.1 equiv) were dissolved in DCE (0.3 mL). The solution was added to a J. Young's NMR tube containing **2c** (12.4 mg, 0.6 mmol, 0.096 M) and TMSNTf$_2$ (0.6, 1.1, 1.6 or 2.1 equiv) was added. Additional DCE was added to make the total reaction volume 0.625 mL. The reaction was monitored at 298 K by ^{19}F NMR spectroscopy to determine the concentration of the product [**2c**-P(*o*-Tol)$_3$][NTf$_2$] and the remaining starting material (**2c**).

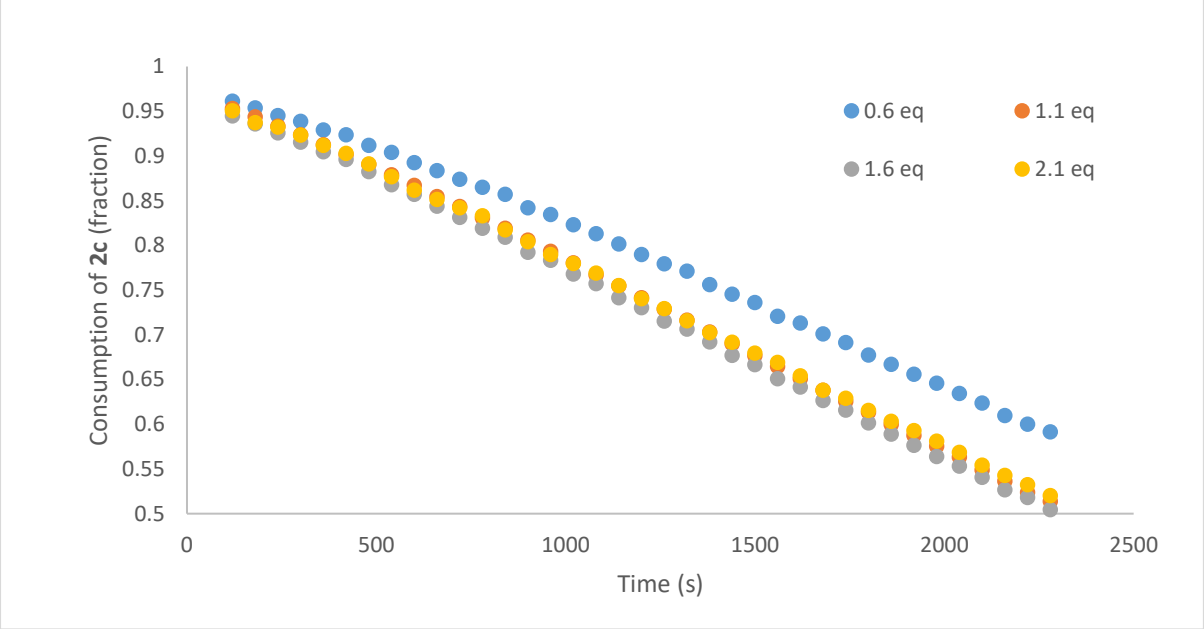

Figure S8. Effect of TMSNTf$_2$ concentration on reaction rate with **FLP-II** and **1a**.

Eq TMSNTf$_2$	k_{obs}
0.60	1.69×10^{-05}
1.10	1.96×10^{-05}
1.60	2.00×10^{-05}
2.10	2.00×10^{-05}

Order in BCF

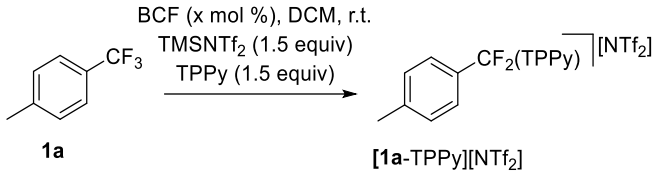

BCF (0.1, 0.2, 0.3 equiv) and TPPy (1.5 equiv) were dissolved in DCM (0.35 mL). The solution was added to a J. Young's NMR tube containing **1a** (24.01 mg, 0.15 mmol, 0.348 M) and $TMSNTf_2$ (1.5 equiv) was added. The reaction was monitored at 298 K by ^{19}F NMR spectroscopy to determine the concentration of the product [**1a**-TPPy][NTf_2] and the remaining starting material (**1a**).

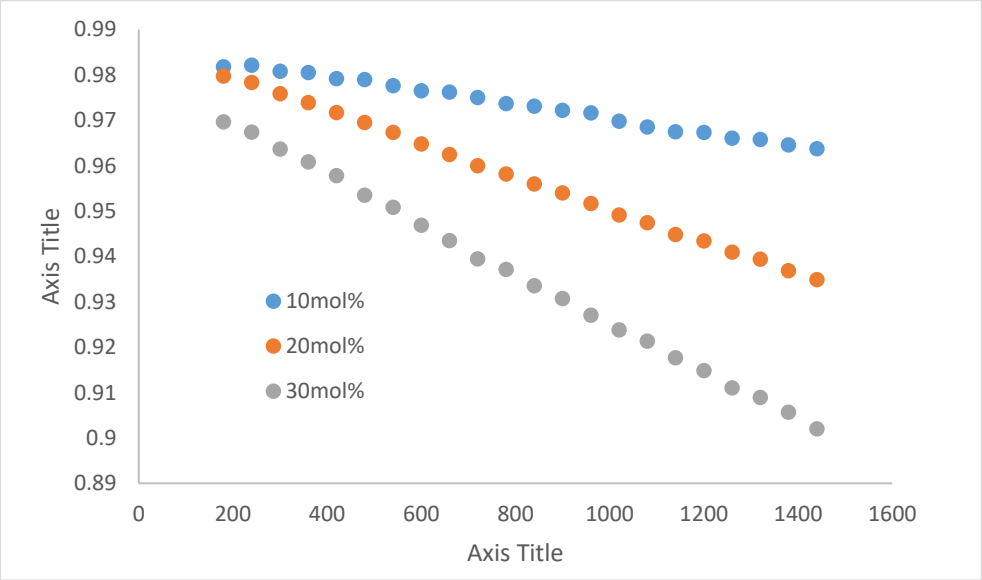

Figure S9. Effect of BCF concentration on reaction rate with **FLP-I** and **1a.**

BCF (mol %)	k_{obs}
10	$5.20x10^{-06}$
20	$1.21x10^{-05}$
30	$1.69x10^{-05}$

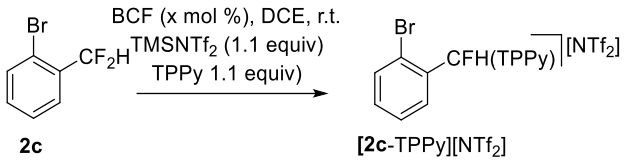

BCF (0.05, 0.1, 0.15 or 0.2 equiv) and TPPy (1.1 equiv) were dissolved in DCE (0.6 mL). The solution was added to a J. Young's NMR tube containing **2c** (12.4 mg, 0.06 mmol, 0.096 M) and $TMSNTf_2$ (1.1 equiv) was added. The reaction was monitored at 298 K by ^{19}F NMR spectroscopy to determine the concentration of the product [**2c**-TPPy][NTf_2] and the remaining starting material (**2c**).

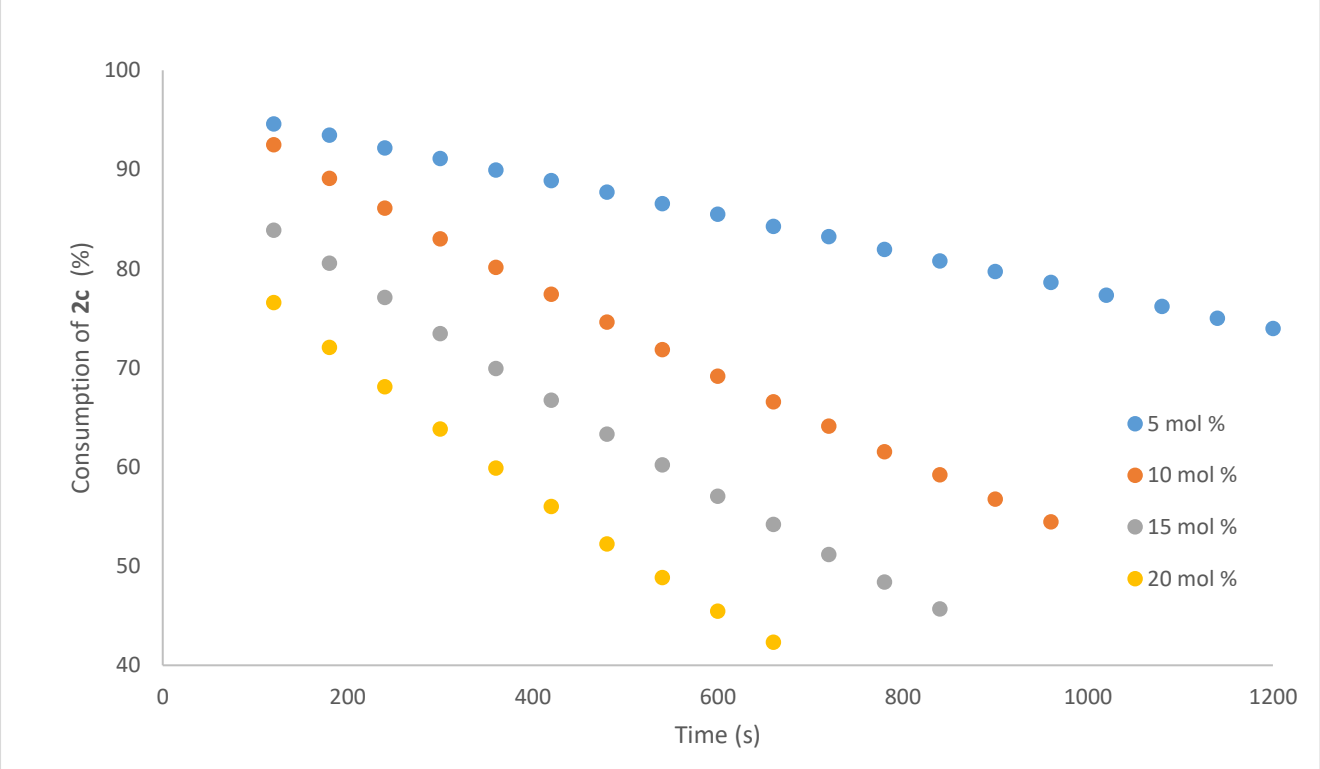

Figure S10. Effect of BCF concentration on reaction rate with **FLP-I** and **2c.**

BCF (mol %)	k_{obs}
5	$1.83x10^{-05}$
10	$4.32x10^{-05}$
15	$5.13x10^{-05}$
20	$5.97x10^{-05}$

Order in fluorocarbon substrate

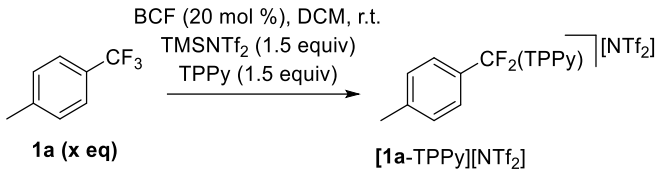

BCF (0.2 equiv) and TPPy (1.5 equiv) were dissolved in DCM (0.35 mL). The solution was added to a J. Young's NMR tube containing **1a** (24.01 mg, 0.15 mmol, 1.0 eq) and $TMSNTf_2$ (1.5 equiv) was added. The reaction was monitored at 298 K by ^{19}F NMR spectroscopy to determine the concentration of the product [**1a**-TPPy][NTf_2] and the remaining starting material (**1a**). The reaction was repeated using 0.5 and 1.5 equiv of **1a** (all other reagents the same).

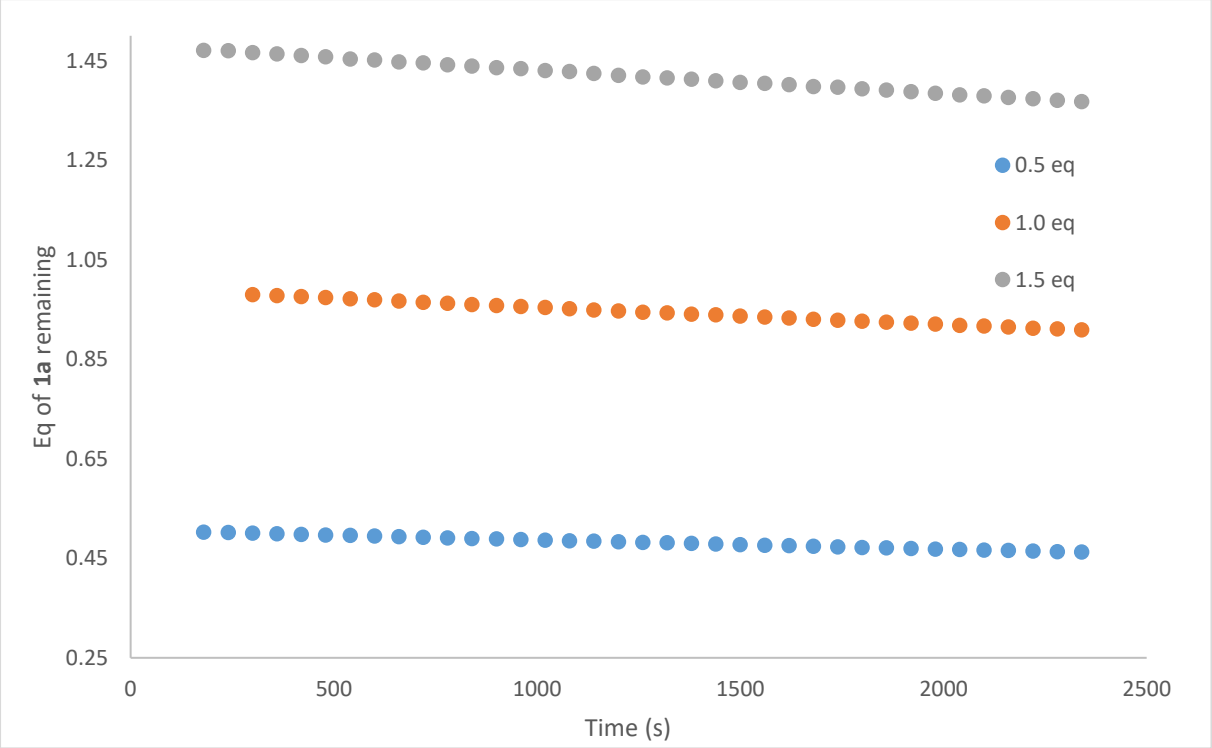

Figure S11. Effect of substrate **1a** concentration on reaction rate with **FLP-I.**

Eq. fluorocarbon (1a)	k_{obs}
0.50	$6.53x10^{-06}$
1.00	$1.21x10^{-05}$
1.50	$1.67x10^{-05}$

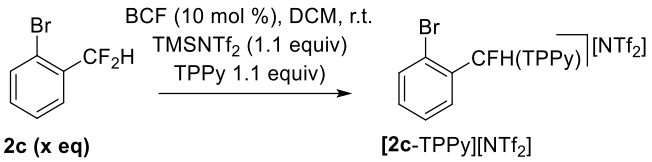

2c (x eq) **[2c-TPPy][NTf$_2$]**

BCF (0.1 equiv) and TPPy (1.1 equiv) were dissolved in DCE (0.3 mL). The solution was added to a J. Young's NMR tube containing **2c** (12.4 mg, 0.06 mmol, 1 eq, 0.096 M) and $TMSNTf_2$ (1.1 equiv) was added. The volume was made up to 0.625 mL with additional DCE. The reaction was monitored at 298 K by ^{19}F NMR spectroscopy to determine the concentration of the product [**2c**-TPPy][NTf_2] and the remaining starting material (**2c**). The reaction was repeated using 0.5, 1.5 and 2.0 equiv of **2c** (all other reagents the same except DCE volume).

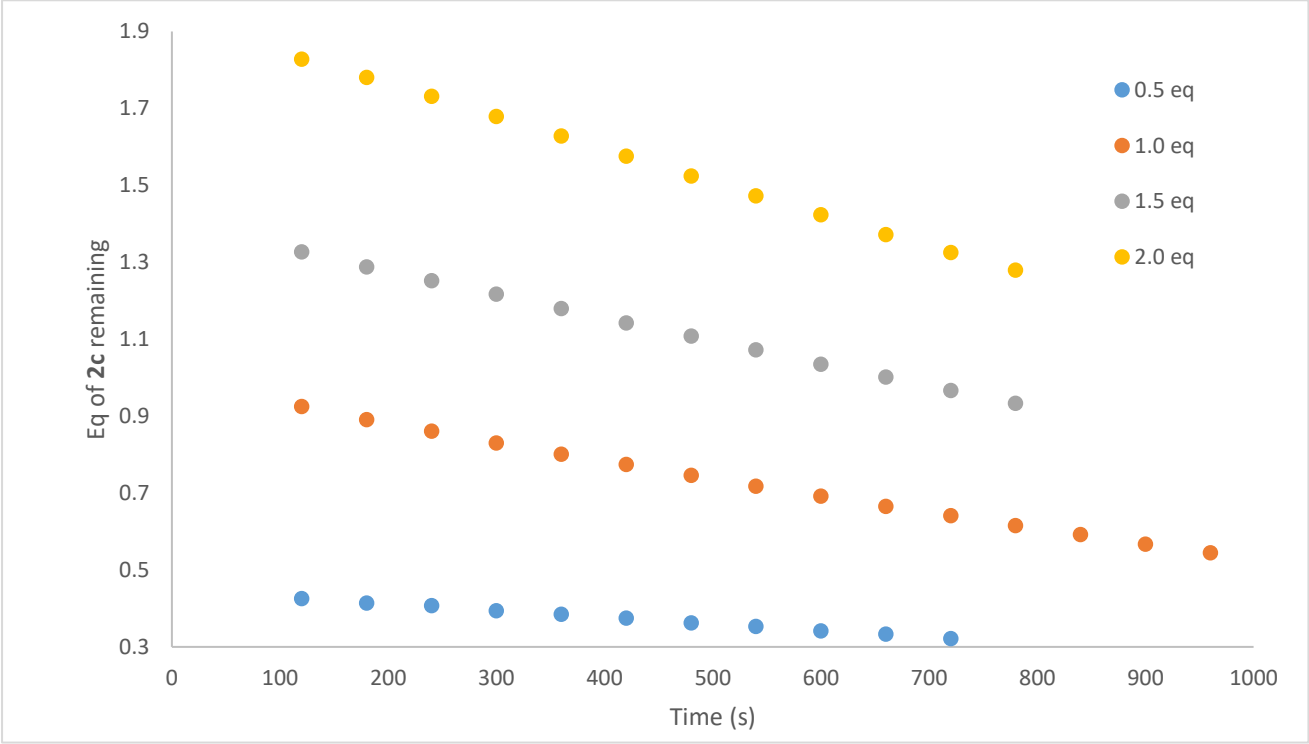

Figure S11. Effect of substrate **2c** concentration on reaction rate with **FLP-I.**

Eq. fluorocarbon (2c)	k_{obs}
0.5	$1.66x10^{-05}$
1	$4.32x10^{-05}$
1.5	$5.73x10^{-05}$
2	$8.08x10^{-05}$

Hammett plot analysis

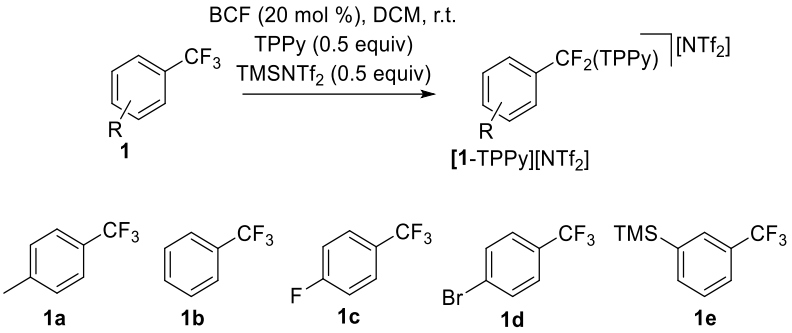

BCF (0.2 equiv) and TPPy (0.5 equiv) were dissolved in DCM (0.3 mL). The solution was added to a J. Young's NMR tube containing a combinations of compounds **1a**, **1b**, **1c**, **1d** and **1e** such that the combined concentration of compounds **1** was equal to 1.0 equiv. Then $TMSNTf_2$ (0.5 equiv) was added. The reaction was monitored at 298 K by ^{19}F NMR spectroscopy to determine the ratio of the products [**1**-TPPy][NTf_2] and the remaining starting materials (**1**).

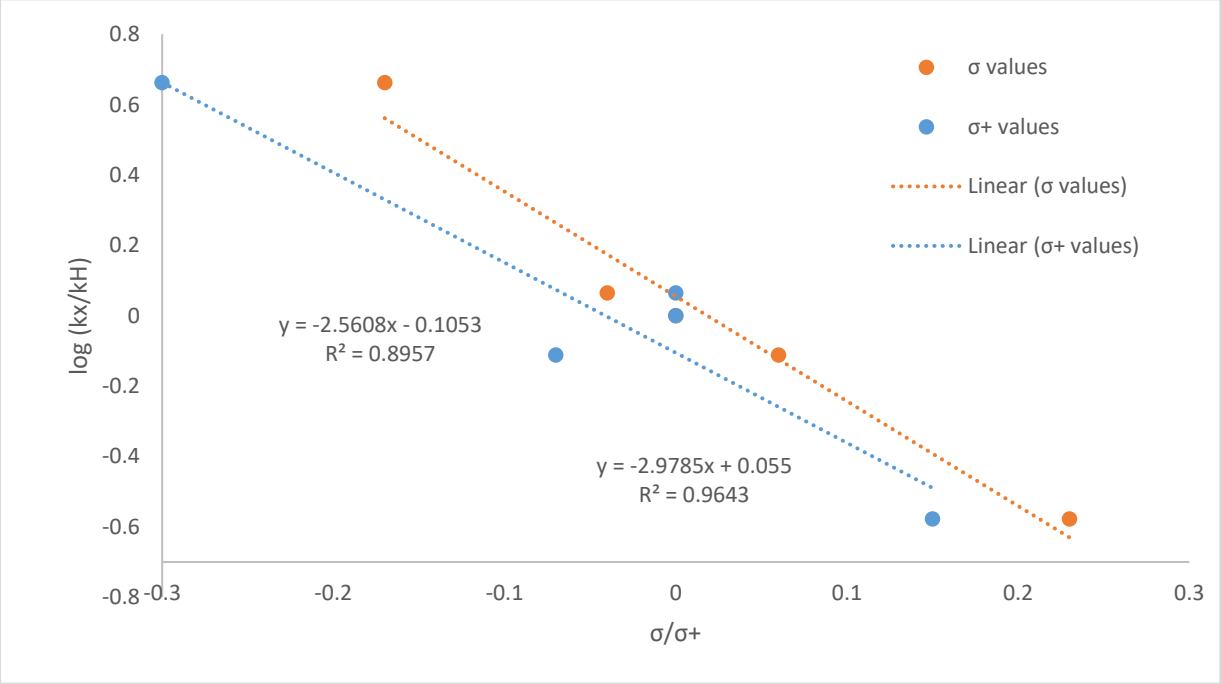

Figure S12. Hammett plot for benzotrifluorides (**1**) with **FLP-I.** ρ = 2.97±0.33; ρ^+ = 2.56±0.50

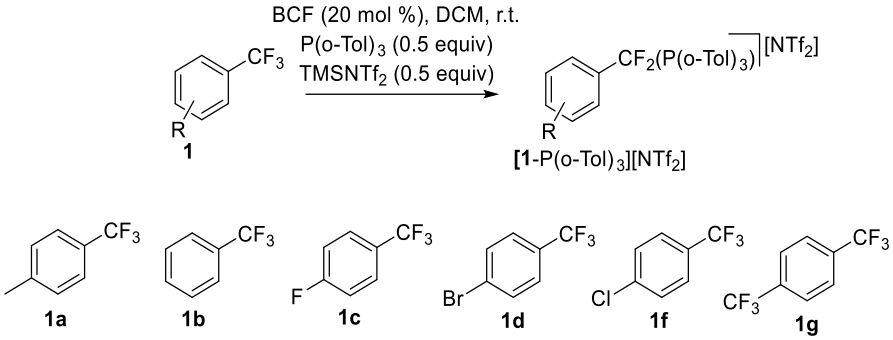

BCF (0.2 equiv) and P(*o*-Tol)$_3$ (0.5 equiv) were dissolved in DCM (0.25 mL). The solution was added to a J. Young's NMR tube containing a combinations of compounds **1a**, **1b**, **1c**, **1d**, **1f** and **1g** such that the combined concentration of compounds **1** was equal to 1.0 equiv. Then $TMSNTf_2$ (0.5 equiv) was added. The reaction was monitored at 298 K by ^{19}F NMR spectroscopy to determine the ratio of the products [**1**-P(*o*-Tol)$_3$][NTf_2] and the remaining starting materials (**1**).

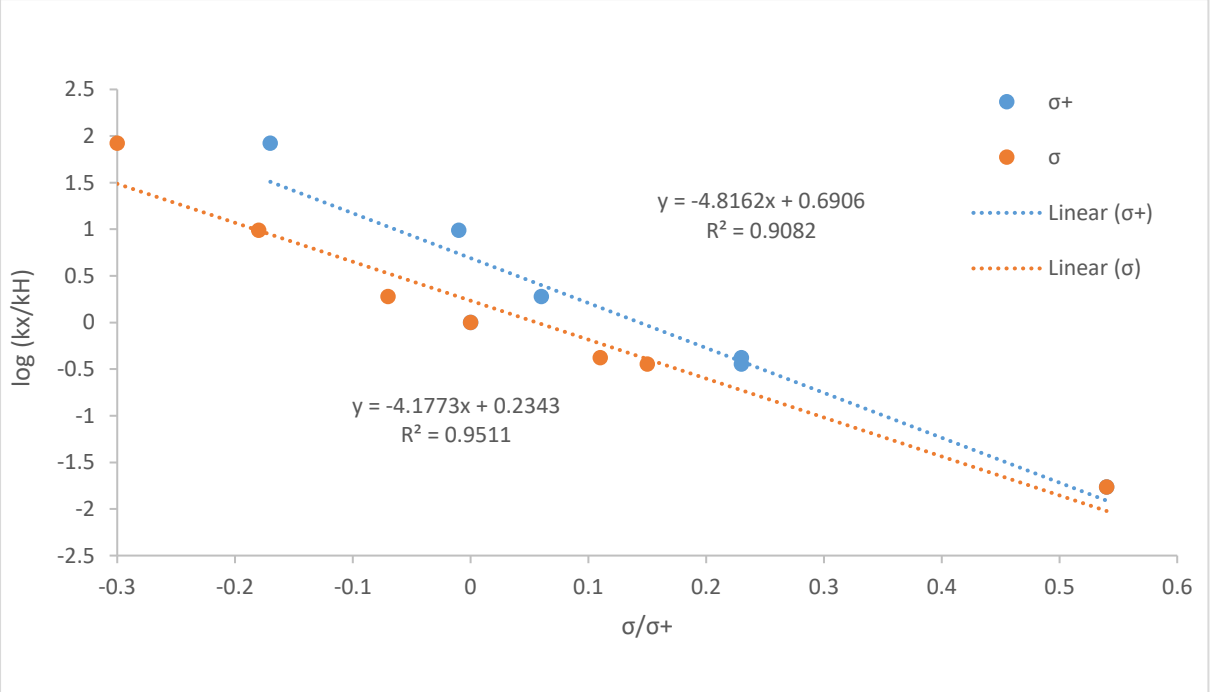

Figure S13. Hammett plot for benzotrifluorides (**1**) with **FLP-II.** ρ = 4.82±0.68; ρ$^+$ = 4.18±0.42

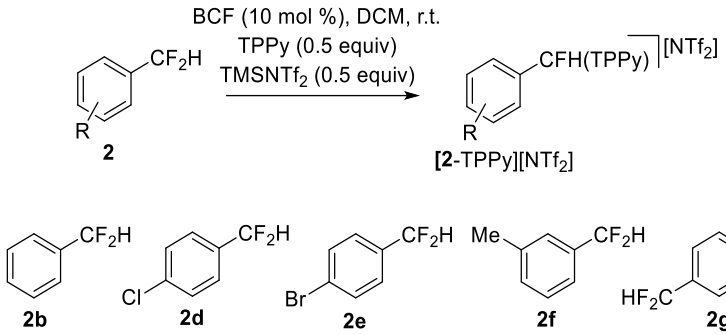

BCF (0.1 equiv) and TPPy (0.5 equiv) were dissolved in DCM (0.25 mL). The solution was added to a J. Young's NMR tube containing a combinations of compounds **2b**, **2d**, **2e**, **2f** and **2g** such that the combined concentration of compounds **2** was equal to 1.0 equiv. Then $TMSNTf_2$ (0.5 equiv) was added. The reaction was monitored at 298 K by ^{19}F NMR spectroscopy to determine the ratio of the products [**2**-TPPy][NTf_2] and the remaining starting materials (**2**).

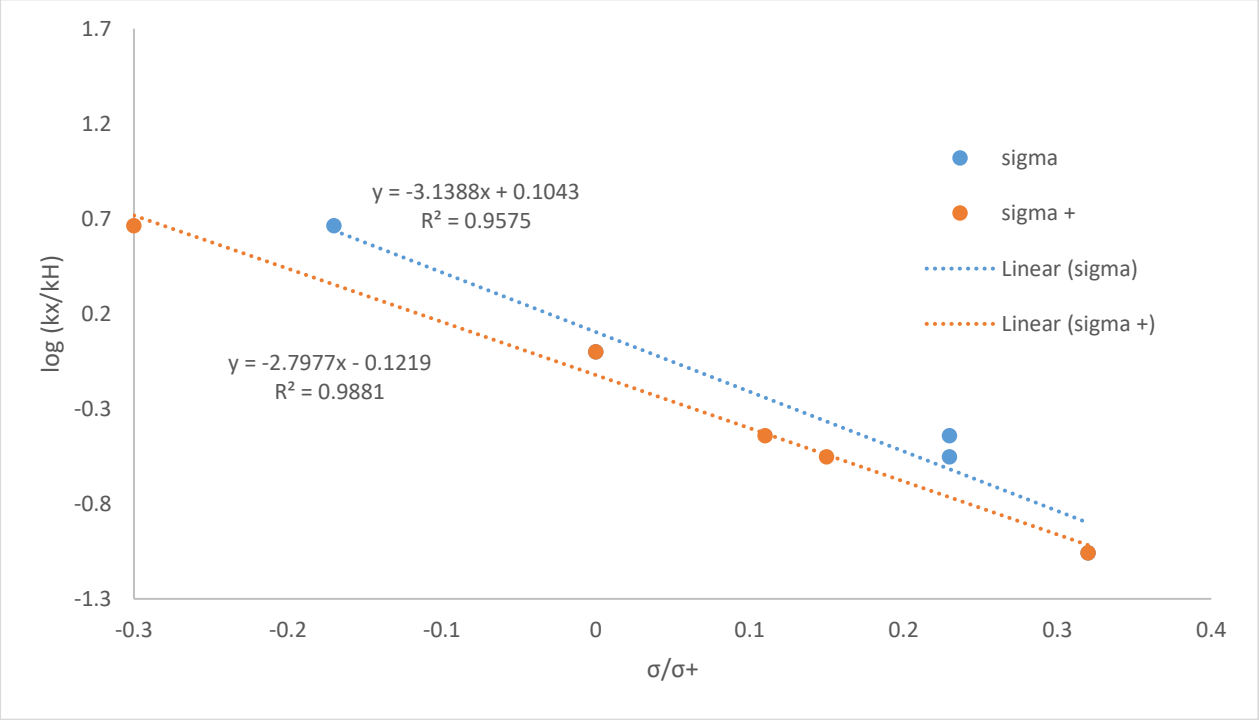

Figure S14. Hammett plot for benzodifluorides (**2**) with **FLP-I.** ρ = 3.14±0.38; ρ^+ = 2.80±0.18

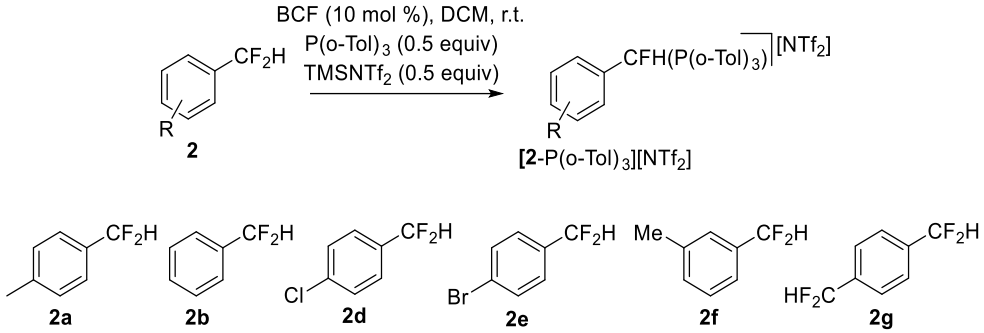

BCF (0.1 equiv) and P(*o*-Tol)$_3$ (0.5 equiv) were dissolved in DCM (0.25 mL). The solution was added to a J. Young's NMR tube containing a combinations of compounds **2a**, **2b**, **2d**, **2e**, **2f** and **2g** such that the combined concentration of compounds **2** was equal to 1.0 equiv. Then $TMSNTf_2$ (0.5 equiv) was added. The reaction was monitored at 298 K by ^{19}F NMR spectroscopy to determine the ratio of the products [**2**-P(*o*-Tol)$_3$][NTf_2] and the remaining starting materials (**2**).

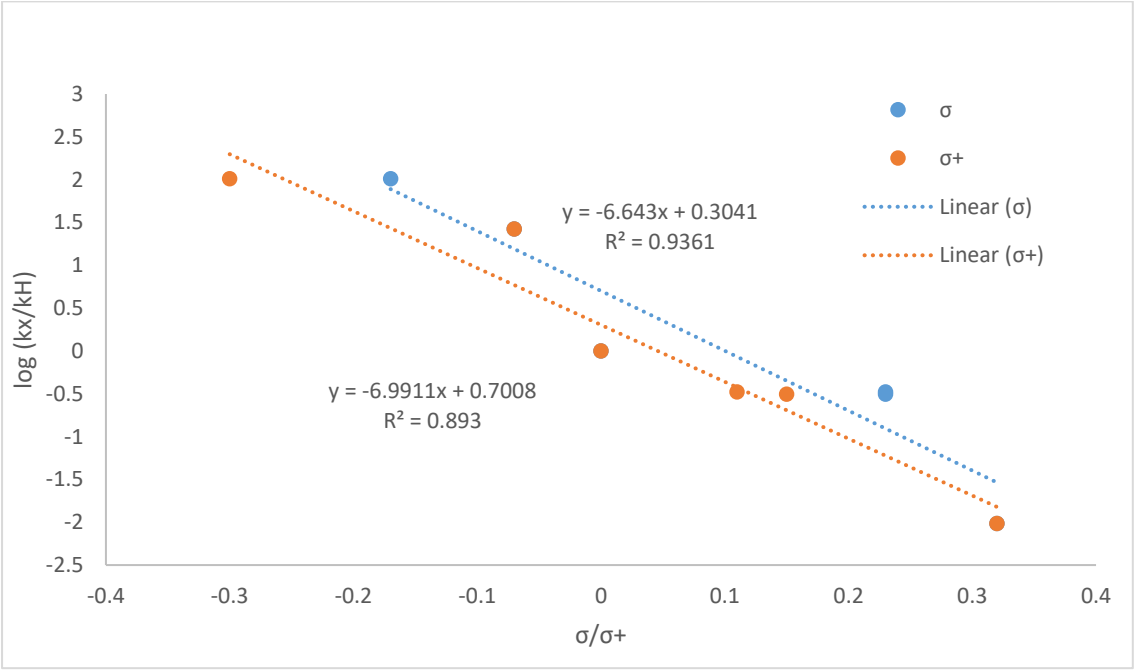

Figure S15. Hammett plot for benzodifluorides (**2**) with **FLP-II.** ρ = 6.99±1.21; ρ$^+$ = 6.64±0.87

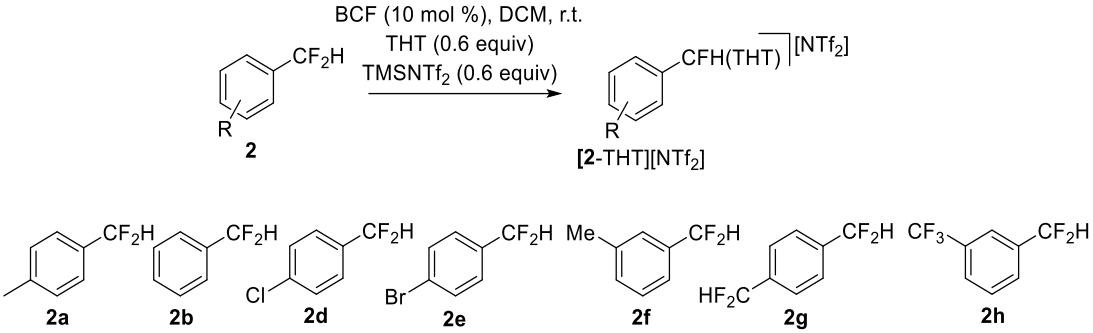

BCF (0.1 equiv) and THT (0.6 equiv) were dissolved in DCM (0.25 mL). The solution was added to a J. Young's NMR tube containing a combinations of compounds **2a**, **2b**, **2d**, **2e**, **2f**, **2g** and **2h** such that the combined concentration of compounds **2** was equal to 1.0 equiv. Then $TMSNTf_2$ (0.6 equiv) was added. The reaction was monitored at 298 K by ^{19}F NMR spectroscopy to determine the ratio of the products [**2**-THT][NTf_2] and the remaining starting materials (**2**).

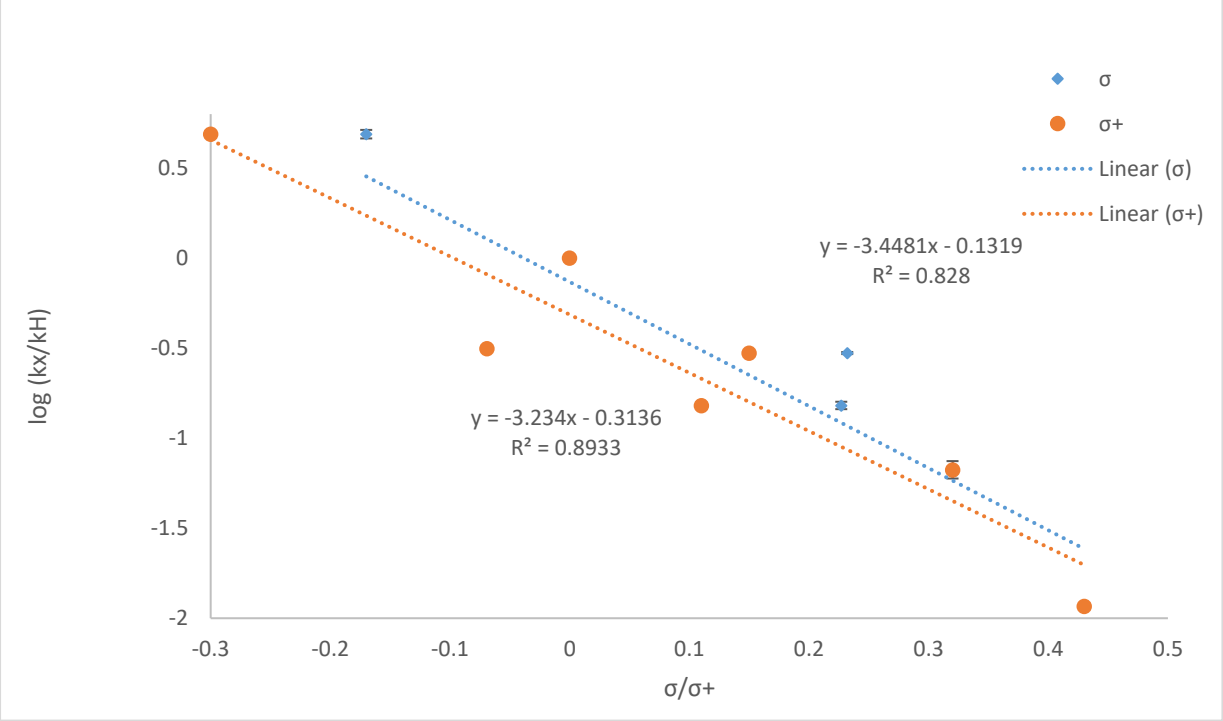

Figure S16. Hammett plot for benzodifluorides (**2**) with **FLP-III.** ρ = 3.45±0.70; ρ^+ = 3.23±0.50

Activation barriers for FLP-1 with 1a and 2c

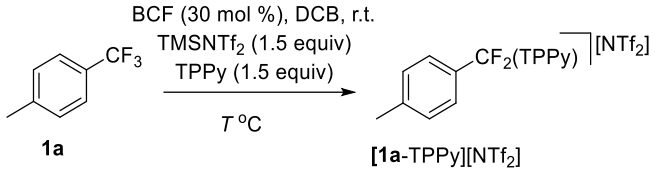

BCF (0.3 equiv) and TPPy (1.5 equiv) were dissolved in DCB (0.35 mL). The solution was added to a J. Young's NMR tube containing **1a** (24.0 mg, 0.15 mmol) and $TMSNTf_2$ (1.5 equiv) was added. The reaction was monitored at 298 K, 318 K or 338 K by ^{19}F NMR spectroscopy to determine the concentration of the product [**1a**-TPPy][NTf_2] and the remaining starting material (**1a**).

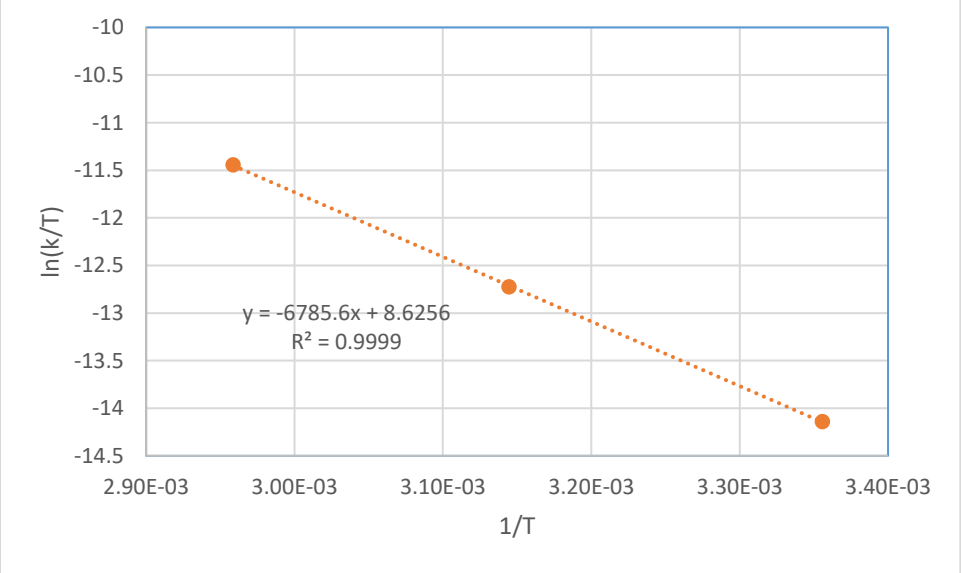

Figure S17. Eyring plot for activation parameters of **1a** with **FLP-I.** $\Delta H^{\ddagger}$ = 13.48 kcal mol^{-1}, $\Delta S^{\ddagger}$ = -0.030 kcal mol^{-1} K^{-1}, $\Delta G^{\ddagger}$ = 22.4±2.3 kcal mol^{-1}

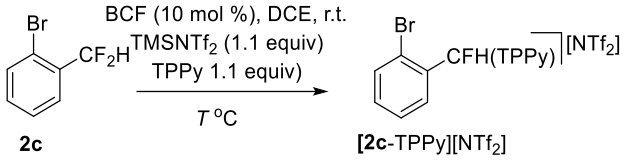

BCF (0.1 equiv) and TPPy (1.1 equiv) were dissolved in DCE (0.6 mL). The solution was added to a J. Young's NMR tube containing **2c** (12.4 mg, 0.06 mmol) and $TMSNTf_2$ (1.1 equiv) was added. The reaction was monitored at 298 K, 308 K or 318 K by ^{19}F NMR spectroscopy to determine the concentration of the product [**2c**-TPPy][NTf_2] and the remaining starting material (**2c**).

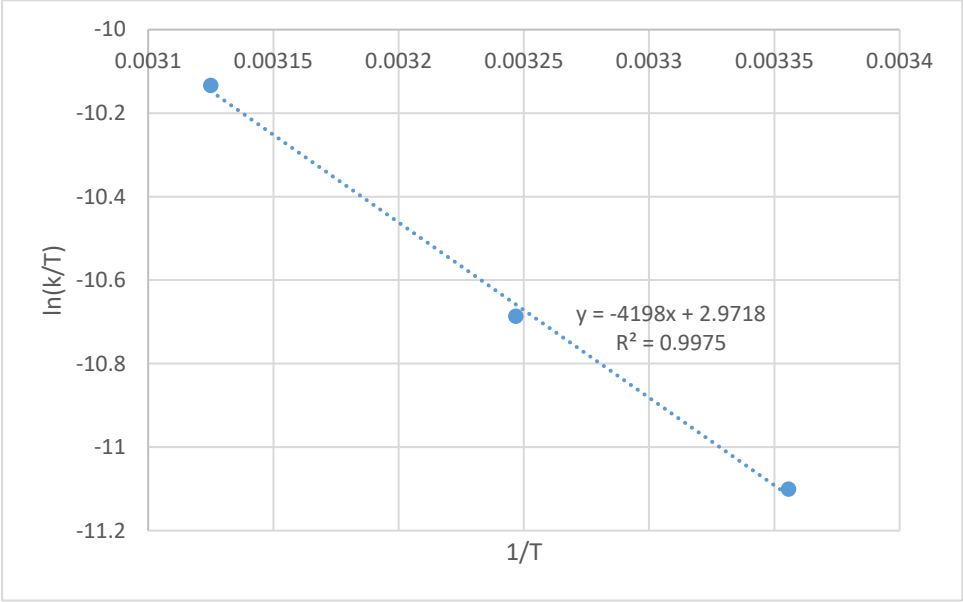

Figure S18. Eyring plot for activation parameters of **2c** with **FLP-I.** $\Delta H^{\ddagger}$ = 9.15 kcal mol^{-1}, $\Delta S^{\ddagger}$ = -0.039 kcal mol^{-1} K^{-1}, $\Delta G^{\ddagger}$ = 20.7±1.3 kcal mol^{-1}

Activation barriers for FLP-II with 1a and 2c

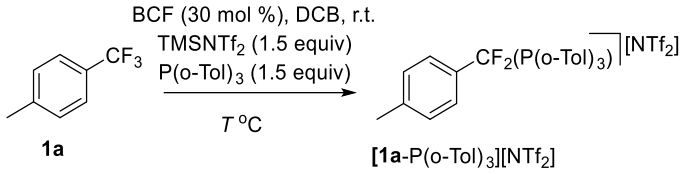

BCF (0.3 equiv) and P(*o*-Tol)$_3$ (1.5 equiv) were dissolved in DCB (0.35 mL). The solution was added to a J. Young's NMR tube containing **1a** (24.0 mg, 0.15 mmol) and $TMSNTf_2$ (1.5 equiv) was added. The reaction was monitored at 298 K, 318 K or 338 K by ^{19}F NMR spectroscopy to determine the concentration of the product [**1a**-P(*o*-Tol)$_3$][NTf_2] and the remaining starting material (**1a**).

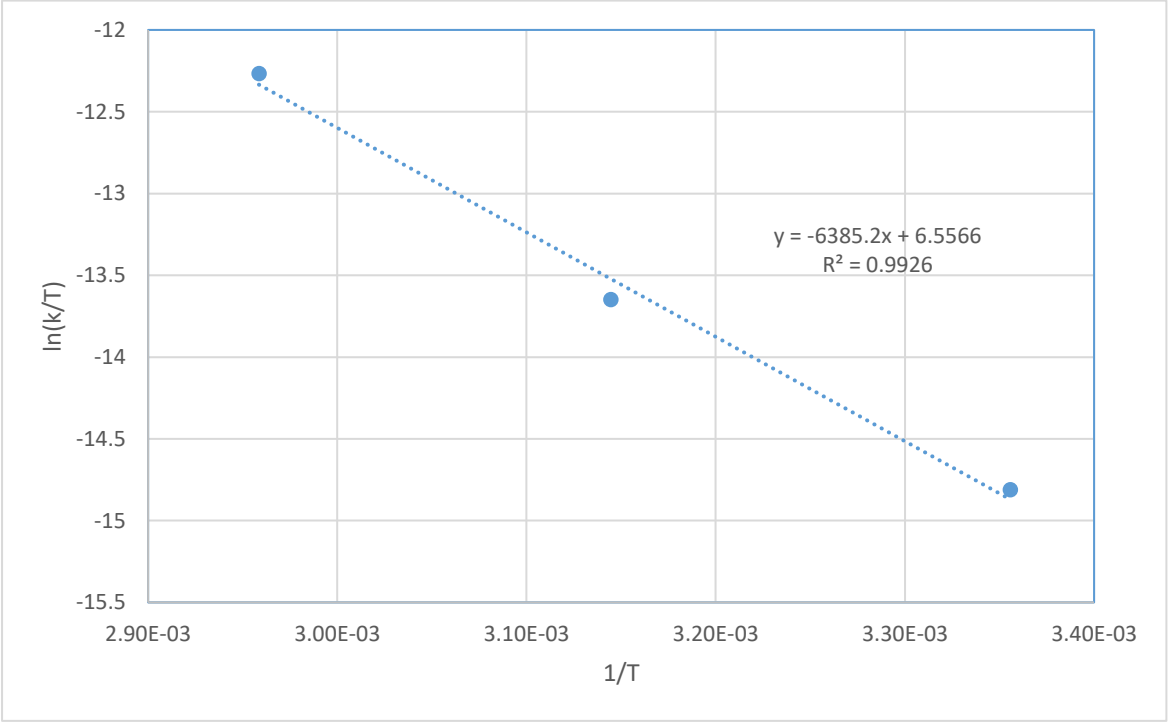

Figure S19. Eyring plot for activation parameters of **1a** with **FLP-II.** $\Delta H^{\ddagger}$ = 12.69 kcal mol^{-1}, $\Delta S^{\ddagger}$ = -0.034 kcal mol^{-1} K^{-1}, $\Delta G^{\ddagger}$ = 22.9±1.7 kcal mol^{-1}

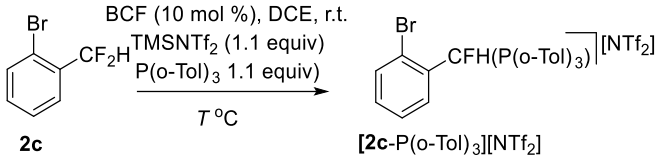

BCF (0.1 equiv) and P(*o*-Tol)$_3$ (1.1 equiv) were dissolved in DCE (0.6 mL). The solution was added to a J. Young's NMR tube containing **2c** (12.4 mg, 0.06 mmol) and $TMSNTf_2$ (1.1 equiv) was added. The reaction was monitored at 298 K, 308 K or 318 K by ^{19}F NMR spectroscopy to determine the concentration of the product [**2c**-P(*o*-Tol)$_3$][NTf_2] and the remaining starting material (**2c**).

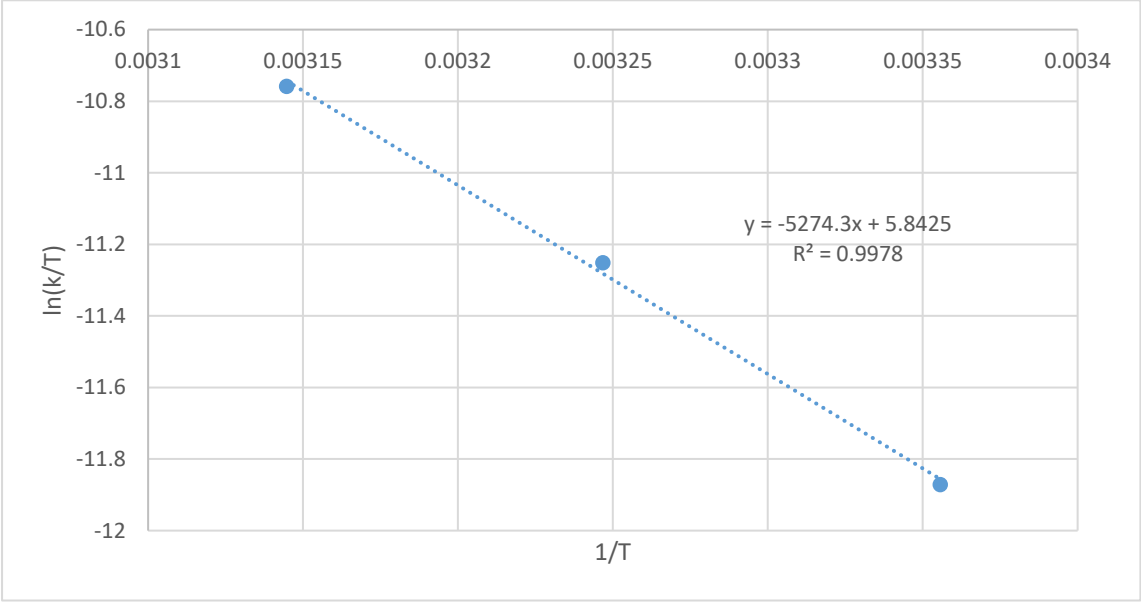

Figure S20. Eyring plot for activation parameters of **2c** with **FLP-II.** $\Delta H^{\ddagger}$ = 10.48 kcal mol^{-1}, $\Delta S^{\ddagger}$ = -0.036 kcal mol^{-1} K^{-1}, $\Delta G^{\ddagger}$ = 21.1±0.7 kcal mol^{-1}

Activation barrier for FLP-III with 2c

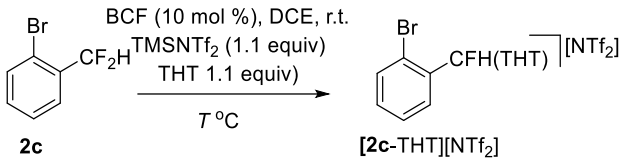

2c **[2c**-THT][NTf_2]

BCF (0.1 equiv) and THT (1.1 equiv) were dissolved in DCE (0.6 mL). The solution was added to a J. Young's NMR tube containing **2c** (12.4 mg, 0.06 mmol) and $TMSNTf_2$ (1.1 equiv) was added. The reaction was monitored at 298 K, 308 K or 318 K by ^{19}F NMR spectroscopy to determine the concentration of the product [**2c**-THT][NTf_2] and the remaining starting material (**2c**).

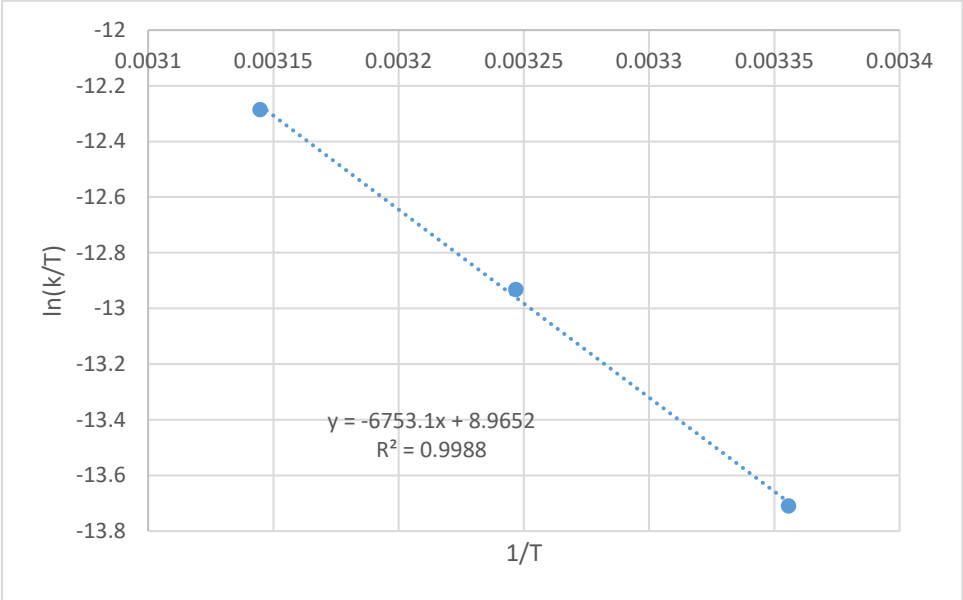

Figure S21. Eyring plot for activation parameters of **2c** with **FLP-III.** $\Delta H^{\ddagger}$ = 13.42 kcal mol^{-1}, $\Delta S^{\ddagger}$ = -0.029 kcal mol^{-1} K^{-1}, $\Delta G^{\ddagger}$ = 22.2±0.6 kcal mol^{-1}

Equilibrium of FLP-I with 1b

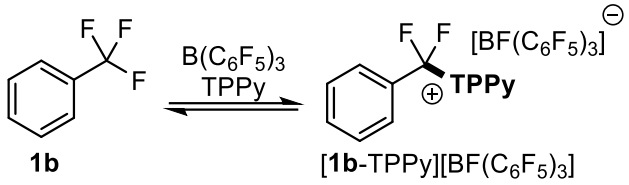

In a J-Young's NMR tube with BCF (1 equiv) and TPPy (1 equiv) in DCM (0.5 mL) was added $PhCF_3$ (**1b**) (11.0 mg). The solution was monitored over 48 hours at room temperature, after which the ratio of **1b** to [**1b**-TPPy][NTf_2] was determined to be 6.15:1 (K_{298} = 0.163, ΔG_0 = 1.1 kcal mol^{-1}).

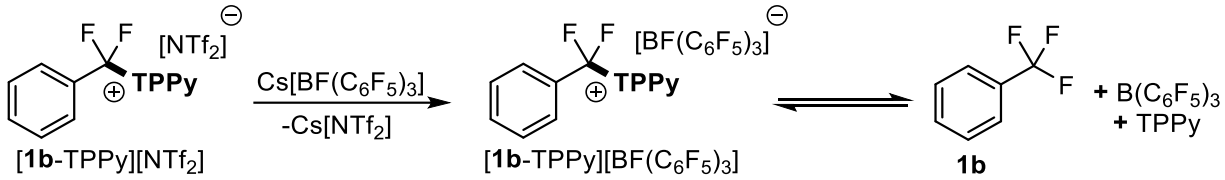

$Cs[BF(C_6F_5)_3]$ (50.0 mg, 0.075 mmol) and [**1b**-TPPy][NTf_2] (53.5 mg, 0.075 mmol) were added to a J-Young's NMR tube and dissolved in DCM (0.5 mL). After 72 hours the ratio of **1b** to [**1b**-TPPy][NTf_2] was determined to be 5.42:1 (K_{298} = 0.185, ΔG_0 = 1.0 kcal mol^{-1}).

Reaction of [2b-P(*o*-Tol)$_3$][BF(C$_6$F$_5$)$_3$] with Me$_3$SiNTf$_2$

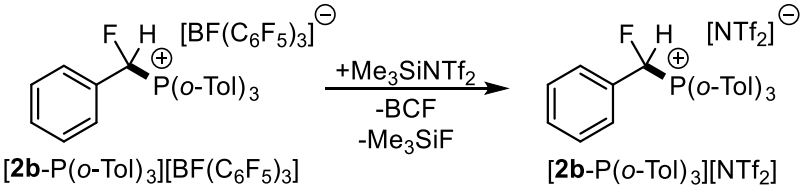

Me_3SiNTf_2 (26 mg, 0.075 mmol) was added to a solution of [**2b**-P(*o*-Tol)$_3$][$BF(C_6F_5)_3$] (50 mg, 0.05 mmol) dissolved in DCB (0.2 mL) in a J-Young's NMR tube. After 2 hours at room temperature, the reaction was monitored by ^{19}F NMR spectroscopy, after which time Me_3SiF, BCF and [**2b**-P(*o*-Tol)$_3$][NTf_2] had formed quantitatively and [**2b**-P(*o*-Tol)$_3$][$BF(C_6F_5)_3$] had been consumed.

Observation and synthesis of 2-Br-C_6H_4-CFH(NTf_2) (2c-NTf_2)

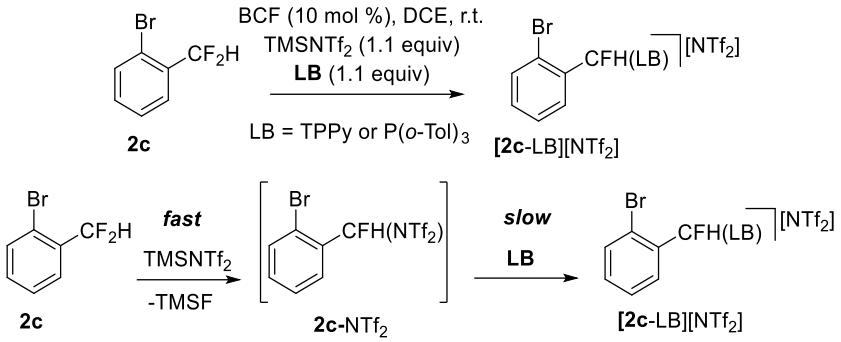

BCF (0.1 equiv) and Lewis base (LB = TPPy or P(*o*-Tol)$_3$) (1.1 equiv) were dissolved in DCE (0.6 mL). The solution was added to a J. Young's NMR tube containing **2c** (12.4 mg, 0.06 mmol) and $TMSNTf_2$ (1.1 equiv) was added. The reaction was monitored at 298 K by ^{19}F NMR spectroscopy to determine the concentration of the product [**2c**-P(*o*-Tol)$_3$][NTf_2], the intermediate **2c**-NTf_2 and the remaining starting material (**2c**).

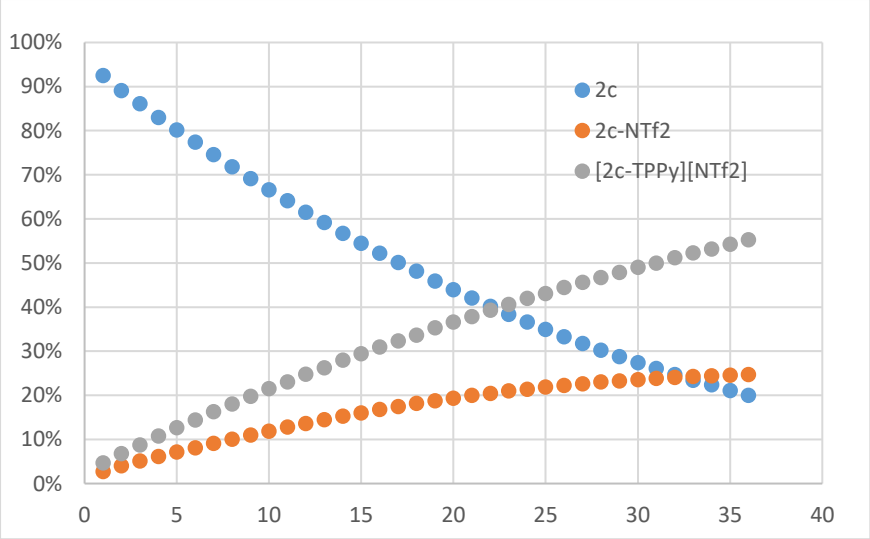

Figure 22. Relative concentrations of **2c**, **2c**-NTf_2 and [**2c**-TPPy][NTf_2] in the reaction of **FLP-I** with **2c** and $TMSNTf_2$.

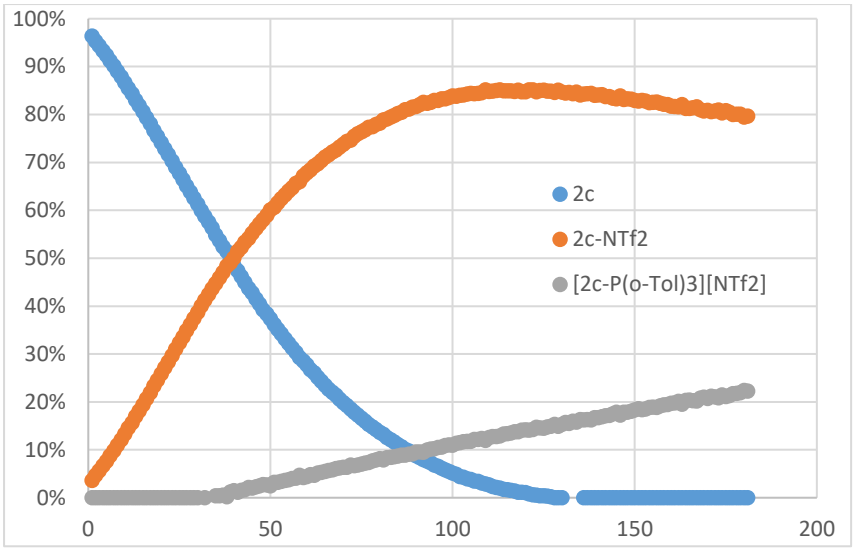

Figure 23. Relative concentrations of **2c**, **2c**-NTf_2 and [**2c**-P(*o*-Tol)$_3$][NTf_2] in the reaction of **FLP-II** with **2c** and Me_3SiNTf_2.

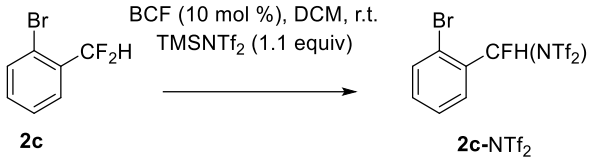

2c **2c**-NTf_2

Compound **2c**-NTf_2 was synthesised and characterised *in situ*. BCF (0.1 equiv) was dissolved in DCE (0.6 mL) and the solution added to a J. Young's NMR tube containing **2c** (12.4 mg, 0.06 mmol) before $TMSNTf_2$ (1.1 equiv) was added. The reaction was monitored at 298 K by ^{19}F NMR spectroscopy. After 24 hours **2c**-NTf_2 was determined to be formed in an NMR yield of 65% (against a $PhOCF_3$ internal standard).

^{19}F NMR (DCE, 298K, 471 MHz): δ_F = -71.5 (s (br), 6 F), -141.1 (s (br, 1 F); **HR-APCI-MS**: *m/z* 466.8742 Anal. Calcd. for $C_9H_5BrF_7NO_4S_2$: 466.8726 $[M]^+$.

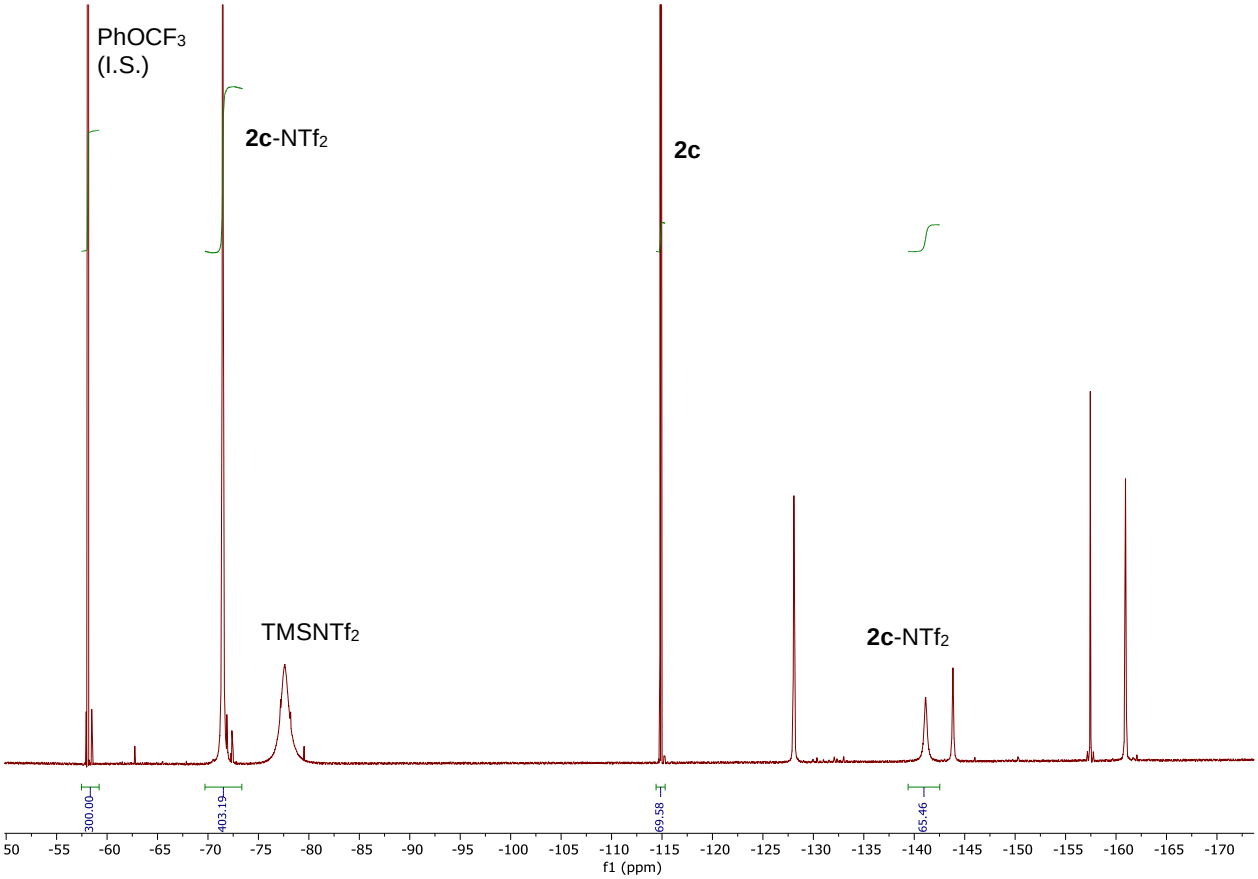

Figure 24. ^{19}F NMR spectrum of reaction BCF (10 mol %), **2c** and $TMSNTf_2$ (1.1 equiv) in DCM after 24 hours at r.t.

Double C-F activation of $PhCF_2H$ (2b)

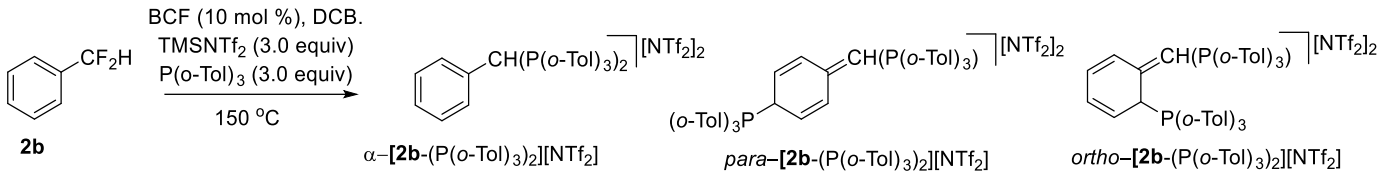

BCF (0.1 equiv) and P(*o*-Tol)$_3$ (3.0 equiv) were dissolved in DCB (0.4 mL). The solution was added to a J. Young's NMR tube containing **2b** (7.7 mg, 0.06 mmol) and $TMSNTf_2$ (3.0 equiv) was added. The reaction was heated at 423 K for 12 hours then analysed by ^{19}F NMR spectroscopy and ESI-MS. It was found that all of **2b** had been consumed, and that ESI-MS signals were observed for $[M]^{2+}$ and $[M\text{-}H]^+$ for the expected products [**2b**-(P(*o*-Tol)$_3$)$_2$][NTf_2]$_2$.

ESI-MS: *m/z* 978.1 Calcd. for $C_{51}H_{48}F_6NO_4P_2S_2$: 978.2 $[M+NTf_2]^+$, 697.1 Calcd. for $C_{49}H_{47}P_2$: 697.3 $[M\text{-}H]^+$, 349.4 Calcd. for $C_{49}H_{48}P_2$: 349.2 $[M]^{2+}$.

C-F activation of [PhCFH(P(*o*-Tol)$_3$)][NTf_2]

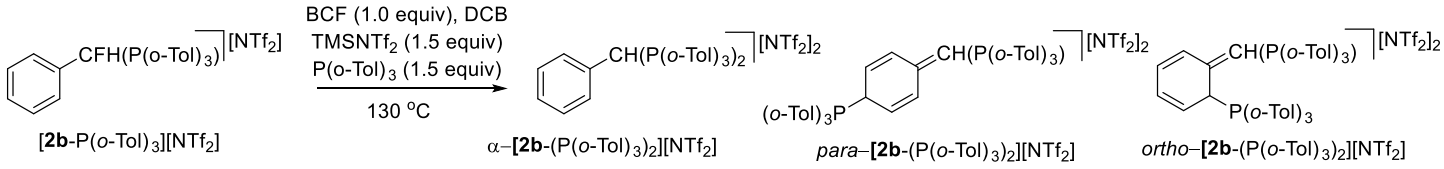

BCF (1.0 equiv) and P(*o*-Tol)$_3$ (1.5 equiv) were dissolved in DCB (0.2 mL). The solution was added to a J. Young's NMR tube containing [**2b**-P(*o*-Tol)$_3$][NTf_2] (7.0 mg, 0.01 mmol) and $TMSNTf_2$ (1.5 equiv) was added. The reaction was heated at 403 K for 12 hours then analysed by ^{19}F NMR spectroscopy and ESI-MS. It was found that all of **2b** had been consumed, and that ESI-MS signals were observed for $[M]^{2+}$ and $[M\text{-}H]^+$ for the expected products [**2b**-(P(*o*-Tol)$_3$)$_2$][NTf_2]$_2$.

ESI-MS: *m/z* 978.1 Calcd. for $C_{51}H_{48}F_6NO_4P_2S_2$: 978.2 $[M+NTf_2]^+$, 697.1 Calcd. for $C_{49}H_{47}P_2$: 697.3 $[M\text{-}H]^+$, 349.4 Calcd. for $C_{49}H_{48}P_2$: 349.2 $[M]^{2+}$.

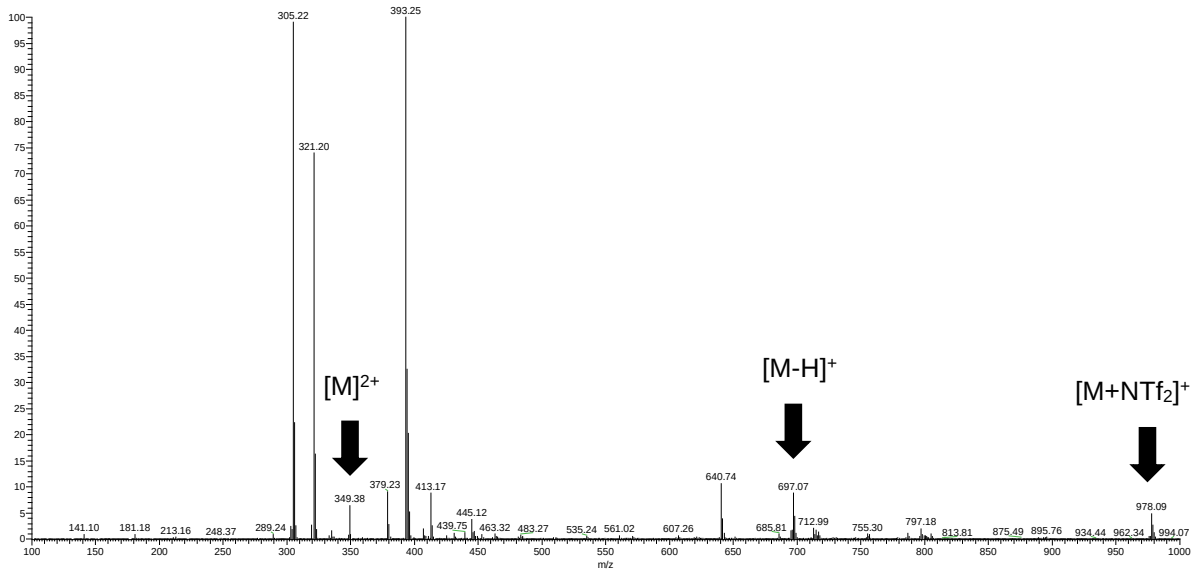

Figure 25. LR-ESI-MS of reaction mixture for double C-F activation of **1b** containing $[PhCH(P(o\text{-}Tol)_3)_2]^{2+}$ {$[M]^{2+}$}, $[PhC(P(o\text{-}Tol)_3)_2]^{+}$ {$[M\text{-}H]^{+}$} and $[PhCH(P(o\text{-}Tol)_3)_2(NTf_2)]^{+}$ {$[M+NTf_2]^{+}$}.

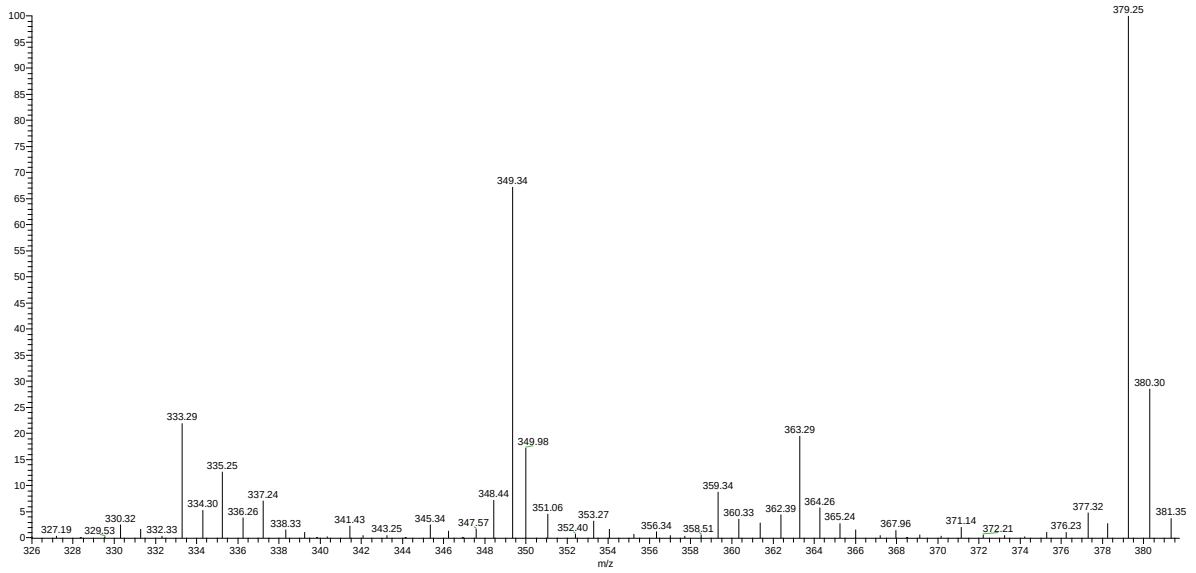

Figure 26. LR-ESI-MS of reaction mixture for double C-F activation of **1b** showing $[PhCH(P(o\text{-}Tol)_3)_2]^{2+}$ {$[M]^{2+}$}.

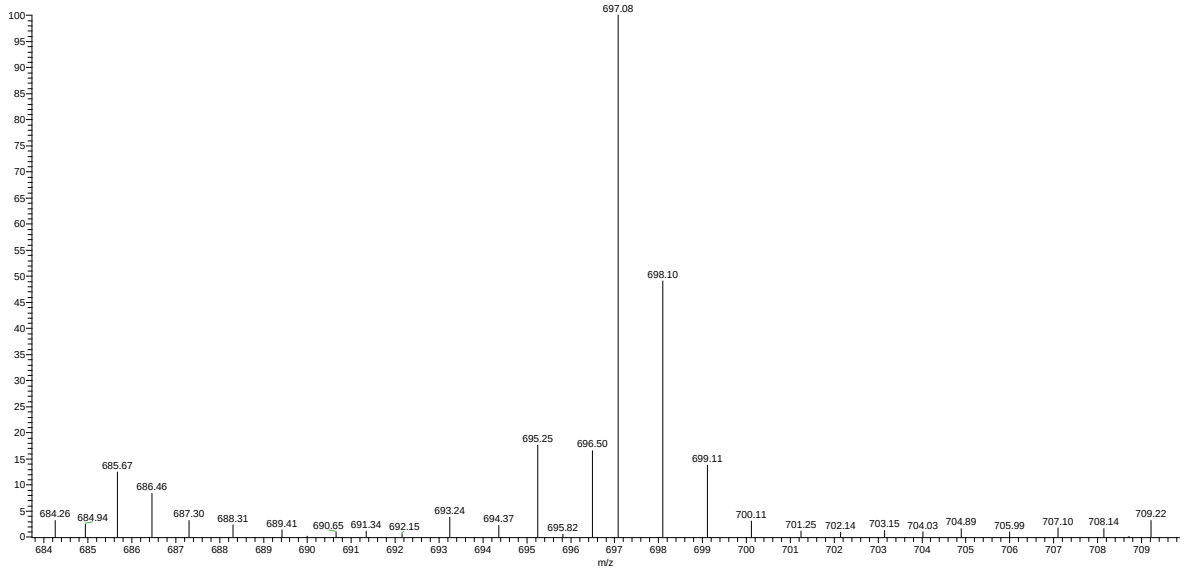

Figure 27. LR-ESI-MS of reaction mixture for double C-F activation of **1b** showing $[PhC(P(o\text{-}Tol)_3)_2]^+$ {$[M\text{-}H]^+$}.

Effect of added THT to FLP-I

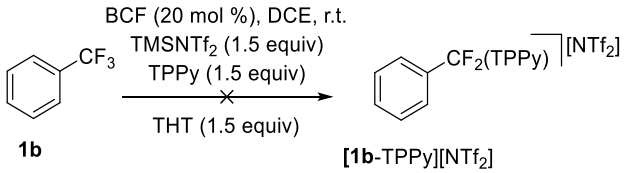

A solution of TPPy (1.5 equiv) and THT (1.5 equiv) in DCE (586 uL) was added to into a vial containing BCF (0.2 equiv). The solution was transferred into a Young's NMR tube containing $PhCF_3$ (8.7 mg, 0.06 mmol). $TMSNTf_2$ was added into the NMR tube and the reaction monitored at room temperature over 48 hours by ^{19}F NMR spectroscopy. After 48 hours, no product and no TMSF was observed.

Computational studies

General computational methodology

To gain insight into the mechanism of CF activation, we performed DFT calculations with the *Gaussian 16* suite of programs (Revision A.03).[4] The calculations were performed using B3LYP functional in combination with Grimme's D3-disperision correction (various DFT functionals were tested, see below for analysis).[5,6] The solvation effects were taken into account by computing the solvation free energies employing the Polarization Continuum Model (PCM) method (solvent: DCM).[7] Geometry optimisations and transition state locations were performed with PCM solvation method. All the converged geometries in solution phase were assessed by vibrational frequency calculations to identify the nature of the obtained structures. Due to several low-frequency vibrational modes, quasi-harmonic correction was applied to the vibrational entropies (frequency cut-off 100 cm^{-1}), following the scheme proposed by Grimme.[8] This was computed with the GoodVibes code.[9] Overall, the reported Gibbs free energies (see formula below) were obtained by combining B3LYP-D3/Def2TZVPP(PCM) electronic energies with the thermal and entropic contributions computed at the B3LYP-D3/Def2SVP(PCM) level (T = 298.15 K) followed by quasi-harmonic correction.[10] In this formula, the value of ΔG_{conc} (0.0030119 Hartree at 298.15 K ≈ 1.89 kcal/mol) corresponds to concentration correction to the Gibbs free energy when shifting from ideal gas standard state (p = 1 atm) to the standard concentration in solution phase (c = 1 mol/dm^3).

$$G = E_0'(\text{DCM}) + (G^q{}_0(\text{DCM}) - E_0(\text{DCM})) + \Delta G_{conc}$$

Transition state location

We applied two strategies to locate transition states. First, we attempted to find a structure that is close to a genuine TS by performing energy scans where constrained geometry optimizations were carried out starting from the reactant state (1b + Lewis base + BCF) and gradually reducing the distances between the corresponding atoms (*e.g.* N/P/S-C or F-B). This strategy was only successful in S_N1 process. The structures corresponding to

the energy maxima on the potential energy curves as initial geometries were utilized in transition state location procedures without any constraint. Herein, it is important to note that S_N1 transition state could be located only if the solvation model (be it PCM or SMD) was used, otherwise the TS location process failed to converge in gas-phase. For the S_N2 TS, this strategy appeared to be ineffective as we could not obtain any suitable initial structure for the purpose of transition state location.

We set out to locate a transition state corresponding to the CF bond activation involving the pyridine as a Lewis base. The calculated activation free energy represented by the **TS$^{CF3/py}$** is 45.7 kcal/mol with respect to **1b** + BCF-py reactant state (Figure S28). Due to the lack of steric barriers, the formation of BCF-py complex is rather favourable, the stability of which was computed to be -13.1 kcal/mol relative to the separate state (BCF + py). In the transition state **TS$^{CF3/py}$**, the lone pair of the pyridine seems to interact with the reactive carbon atom, or at least, the lone pair of the pyridine is well orientated for an S_N2 process. Indeed, IRC calculations showed the direct formation of the [py-**1b**]$^{+\cdots}$[BCFF]$^-$ ion pair, with no transient carbocation intermediate on the reaction pathway.

To locate the S_N2 transition state involving TPPy, we used the structure of **TS$^{CF3/py}$** in which pyridine was changed to TPPy by placing phenyl groups on the pyridine ring. Prior to the TS location, constrained geometry optimization was performed while retaining the atomic distances around the reactive centre. The obtained transition state can be seen in Figure S29. The structural features of such a transition state (**TS$^{GD3/PCM}$-1**) is quite different to that of **TS$^{CF3/py}$**. The N-C distance is longer than that in **TS$^{CF3/py}$**, and more importantly, the orientation of the lone pair is not ideal for a nucleophilic substitution. In the course of the optimisation, the py ring of the TPPy became tilted in such a way that its aromatic rings are accommodated to interact with the substrate via π-π stacking. Furthermore, IRC calculations revealed a high-lying TPPy$^{\cdots}$[**1b**]$^{+\cdots}$[BCFF]$^-$ intermediate along this reaction path, which suggests a two-step process with the Lewis base. Based on the obtained free energy data, the S_N2 energy barrier amounts to 30.2 kcal/mol, the corresponding barrier for S_N1 is only 26.2 kcal/mol. This free energy differences show a preference for the reaction to proceed via S_N1.

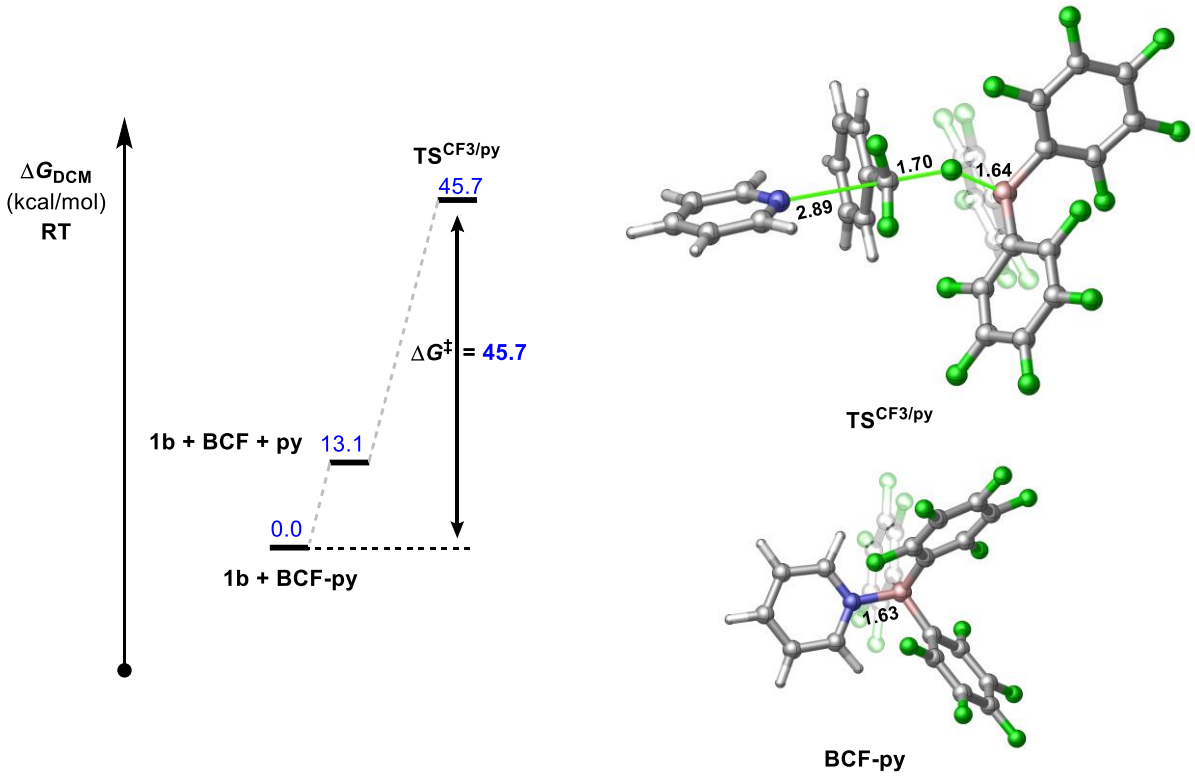

Figure S28. Relative Gibbs free energy profile for C-F activation by pyridine. Computationally identified transition state and **BCF-py** complex are shown along with selected bond distances given in Å.

Testing DFT methods

To assess the solvation effects on reaction mechanism, we located the S_N1 and S_N2 transition states varying the solvation models (SMD *vs* PCM). Further to this, we tested two versions of an empirical dispersion correction, namely D3 version of Grimme's dispersion with the original D3 damping function and with Becke-Johnson damping. Next, we carried out some test calculations to assess the functional-dependence of the mechanism (see Figure S29). The single-point energies were calculated using the M06-2X[11] and ωB97X-D[12] functionals on the respective located transition states, and the thermal and entropic contributions were taken into account at the level of theory used to locate the transition state (these barriers are shown in square brackets in Figure S29).

Based on the calculated barrier heights, the S_N1 pathway was calculated to be favoured as compared to the S_N2 pathway, irrespective of the computational method applied. The free energy gap between the two pathways ranges between 4.0 and 6.6 kcal/mol in favour of S_N1. The transition states related to S_N2 were found to lie *ca*. 2 kcal/mol higher in energy when SMD solvation model was used than the analogous TSs obtained with PCM model. The obtained free energy difference when comparing the two dispersion corrections is negligible (~0.5 kcal/mol). Generally, M06-2X and ωB97X-D functionals predicted higher activation energies in comparison with B3LYP-D3. The trends in the relative barrier heights obtained with the two functionals are the same, implying that the mechanistic conclusions are likely to remain invariant in terms of DFT functionals. However, it should be noted that a thorough conformational analysis was also required. The transition states depicted in Figure S29 were obtained starting the TS location from the pyridine model system, and thus, the optimisation may have not resulted in the most stable conformer of the transition state. The conformational analysis was performed in the next step using the structures of S_N1 and S_N2 transition states obtained at the level of PCM(DCM)-B3LYP-D3/def2TZVPP//PCM(DCM)-B3LYP-D3/def2SVP theory (for the sake of comparison with Fernández's structures). The described strategy was used for reactions with P(*o*-Tol)$_3$ (**PTol**) and **THT**. Ultimately, we propose this computational methodology as a reasonable starting point for our investigations on the reaction mechanism of the FLP-mediated CF-activation.

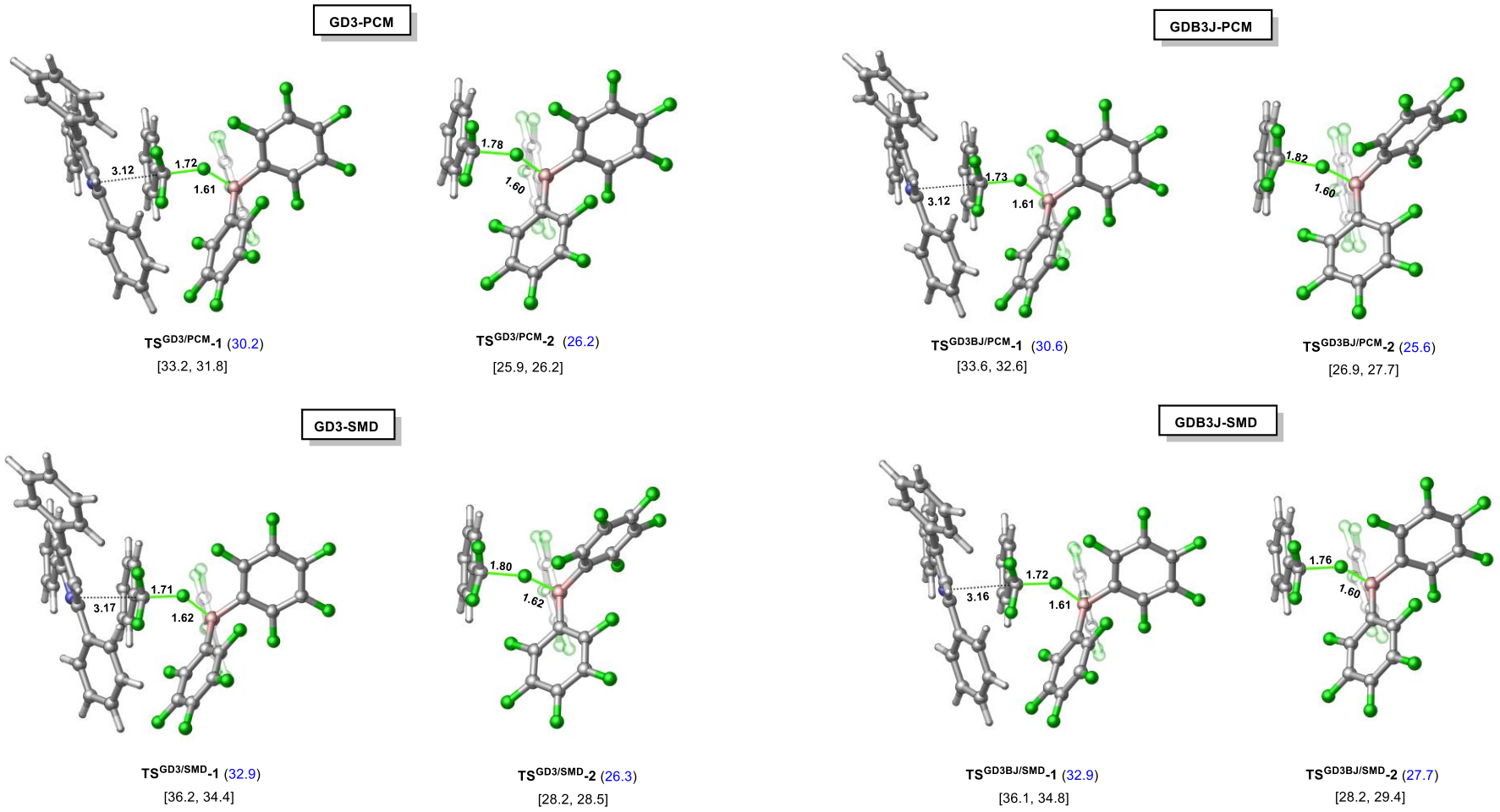

Figure S29**.** Transition states corresponding to S_N2 and S_N1 mechanisms obtained with B3LYP functionals. The applied dispersion correction and solvation model are indicated in the boxes. Relative stabilities (in kcal/mol) are shown in parentheses with respect to **1b** + BCF + TPPy. The barrier heights derived from single point calculations with M06-2X and ωB97X-D functionals are shown in square brackets, respectively.

Conformational analysis

In our study, an extensive conformational search was carried out for the the S_N2 and S_N1 transition states, and the most stable conformers were used to construct the relative free energy profiles.

We employed Monte Carlo sampling using the OPLS_2005 force field integrated in the *MacroModel* software.[13] The N/P/S···C···F···B (in S_N2 TS) and C···F···B (in S_N1 TS) atoms were frozen in the course of the conformational search to retain the bond lengths found in the transition state obtained at the level of PCM(DCM)-B3LYP-D3/def2SVP theory. For consistency, the same parameters were used in the conformational analysis of each investigated transition states. The important parameters are the followings: Solvent: none, Optimization method: PRCG, Maximum iteration of optimization: 15 000, Convergence threshold of optimization: 0.05 Maximum number of steps: 10 000 (300 steps per rotatable bond), CSearch method: Mixed torsional/Low-mode sampling, Energy window: 42 kJ/mol (= 10 kcal/mol). The generated transition state structures were subjected to optimization at the level of PCM(DCM)-B3LYP-D3/def2SVP theory. Upon DFT optimization, we obtained several conformers, and some representative examples are shown in Figures S36, S38, S40 and S42 for **1b**, as well as S44, S46, S49, and S51 for **2b**.

FLP and LP with BCF and TPPy, PTol, or THT

BCF-TPPy adducts (LP-I)

DFT calculations were performed to estimate the relative stability of possible adducts that can form upon reacting **BCF** with **TPPy** in solution phase. The classical B-N adduct, **BCF-TPPy**, was predicted to be well above the separate state (**BCF** + **TPPy**), namely at 10.2 kcal/mol (Figure S30). The presence of this adduct is highly unlikely in the solution phase.

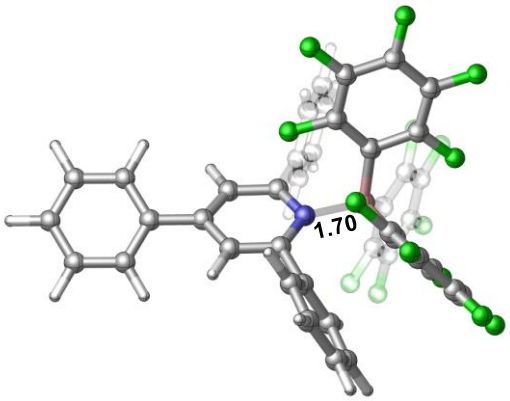

BCF-TPPy (10.2)

Figure S30**.** DFT-optimized **BCF-TPPy** complex featuring B-N dative bond. The relative stability (in blue) is given in kcal/mol with respect to **BCF** + **TPPy** state.

Generally, the π-π adducts are predicted to have higher stabilities (Figure S31), they are about 3 kcal/mol above the separate state (**BCF** + **TPPy**). It is plausible that a rapid equilibrium exists in the solution.

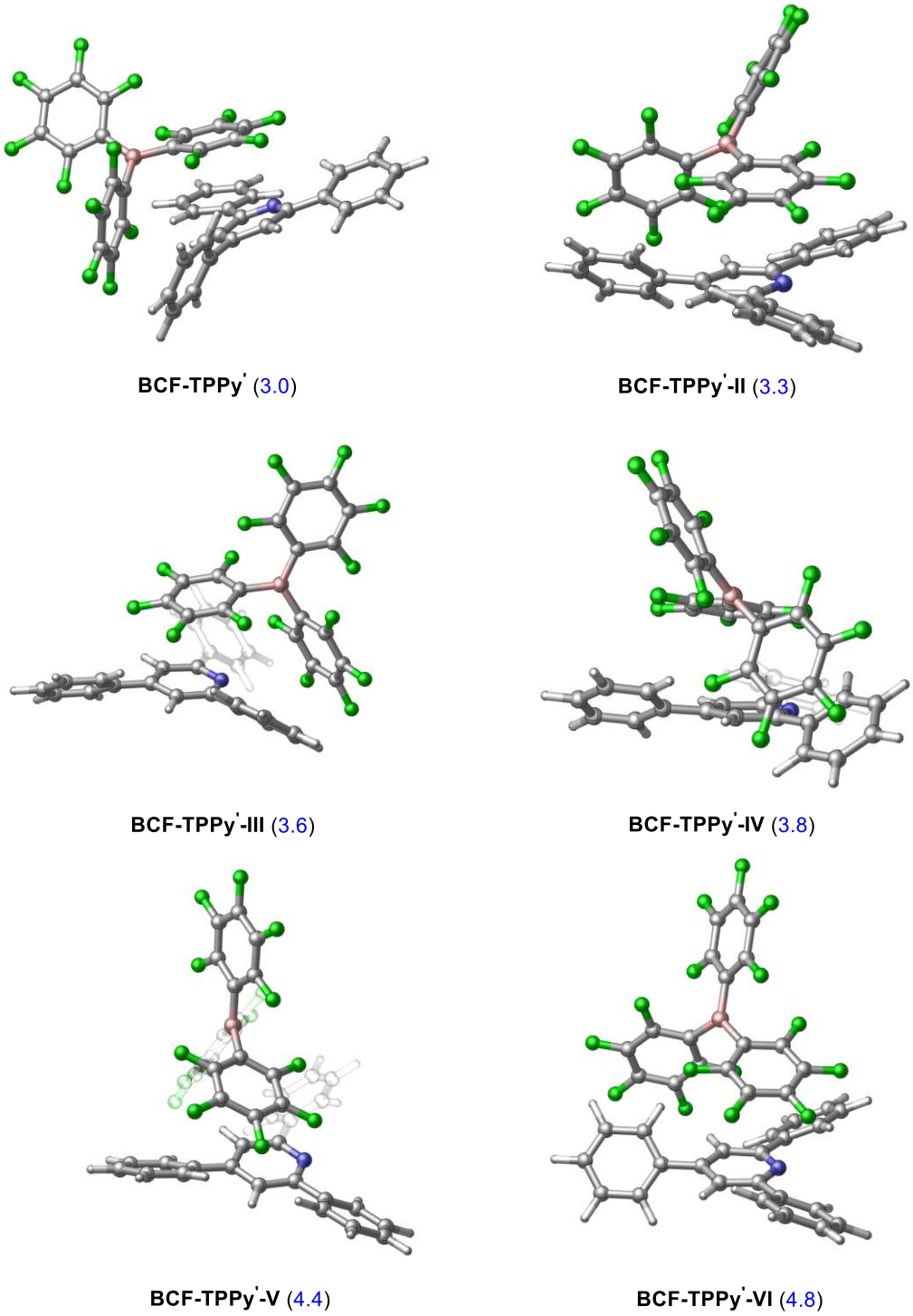

Figure S31. Computationally identified π-π adduct between **BCF** and **TPPy**. The relative stability (in blue) is given in kcal/mol with respect to **BCF** + **TPPy** state.

BCF-PTol adducts (LP-II)

Several possible adducts with **BCF** and **PTol** were investigated as well (Figure S32). In **BCF-PTol**, the P atom resides relatively close to the boron centre of BCF and it is conceivable that stabilizing π-π stacking interactions between arenes on the PTol and BCF are present. Yet, the formation of the adduct **BCF-PTol** is slightly endergonic (3.2 kcal/mol). Despite the apparent interaction between P and B atoms (pyramidal B atom and short P-B distance), the formation of **BCF-PTol-I** is even less favourable (8.1 kcal/mol). The decreased stability is likely to be attributed to a steric clash between the Me groups at the back of the **PTol**.

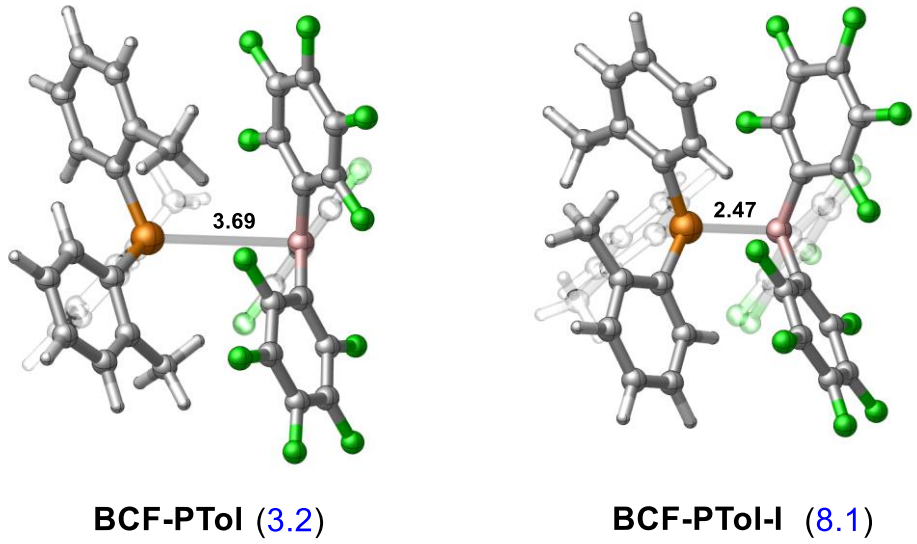

Figure S32. DFT-optimized **BCF-PTol** complexes. The relative stability (in blue) is given in kcal/mol with respect to **BCF** + **PTol** state.

Based on the computed free energies, the adduct involving **PTol** and **BCF** (an arene π-π stacking adduct) is assumed to be present in solution (Figure S33). The most stable adduct is **BCF-PTol'** which is only 1.5 kcal/mol above the **BCF** + **PTol** state.

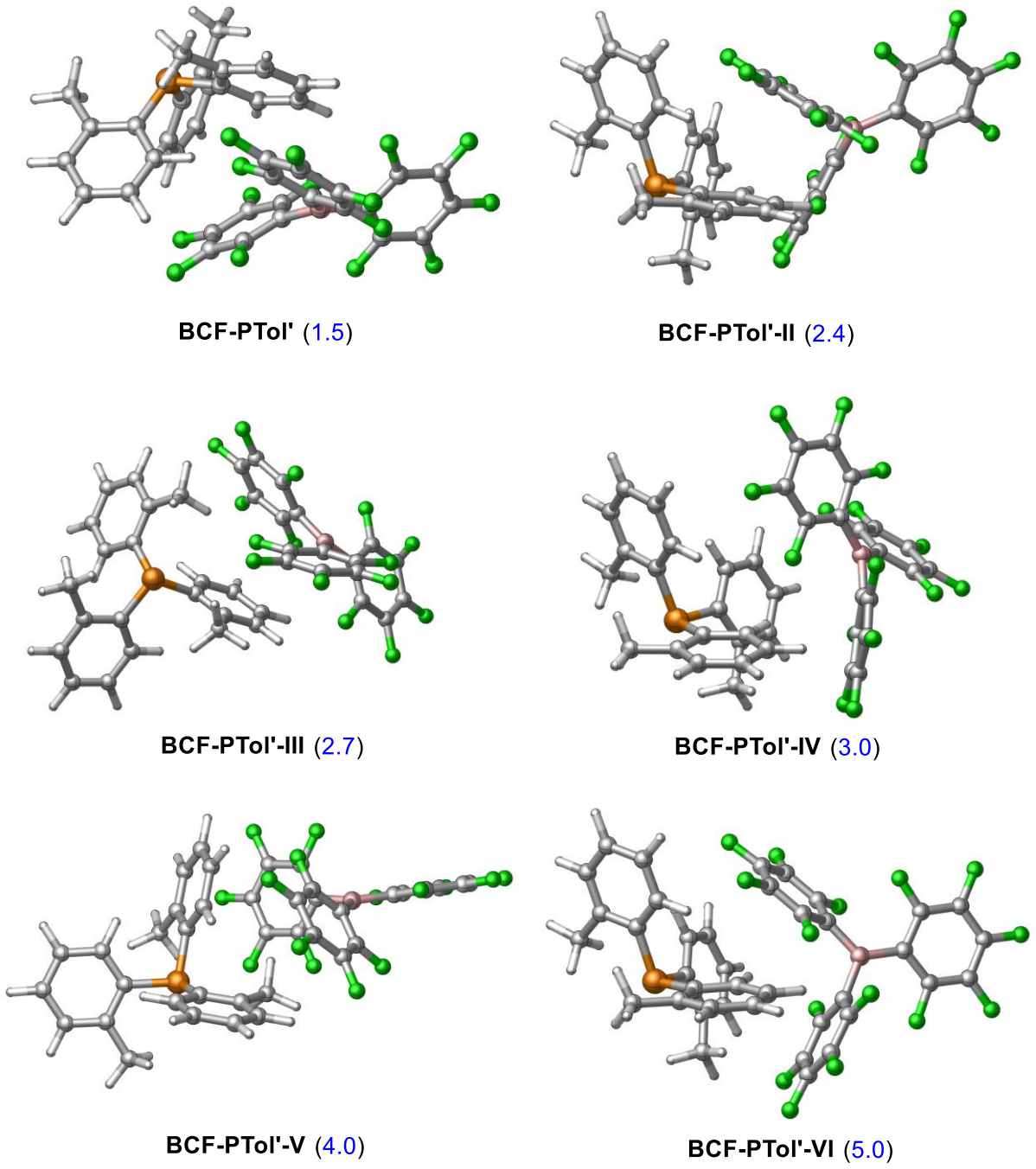

Figure S33. Computationally identified π-π adduct between **BCF** and **PTol**. The relative stability (in blue) is given in kcal/mol with respect to **BCF** + **PTol** state.

BCF-THT adducts (LP-III)

The formation of **BCF-THT** is thermodynamically feasible (Figure S34). The free energy changes associated with the adduct formation is -0.9 kcal/mol, which is likely due to the sterically more accessible environment around the sulfur atom. In these **BCF-THT** adducts, the B centres are slightly pyramidal which is clearly the consequence of the coordinative interaction between the sulfur and the Lewis acidic boron centre.

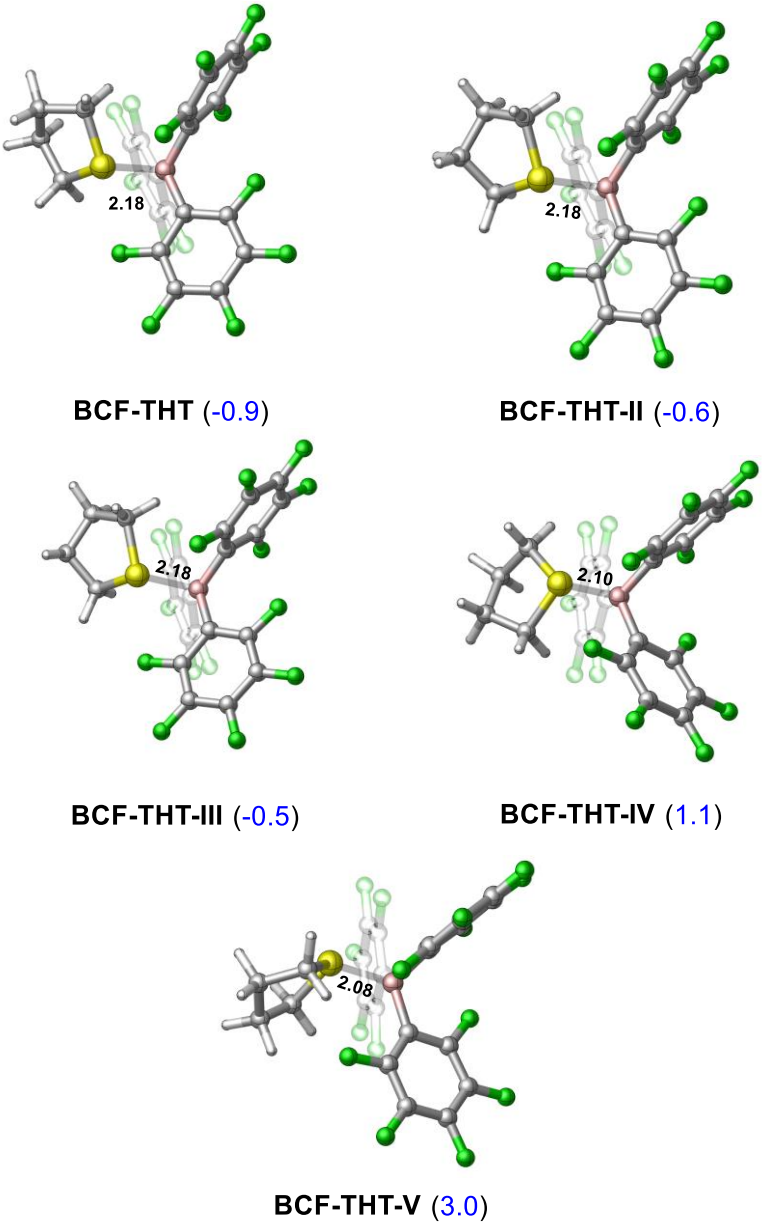

Figure S34. DFT-optimized **BCF-THT** complexes featuring B-S dative bond. The relative stability (in blue) is given in kcal/mol with respect to **BCF** + **THT** state.

Activation of $PhCF_3$ – S_N1 pathway

DFT calculations were performed to estimate the barrier height related to S_N1 mechanism. The computed relative free energy profile is shown in Figure S35. The C-F activation proceeds with the involvement of BCF, and we obtained a barrier of 25.2 kcal/mol for this process. The reactive adduct **1b**···**BCF** lies at 6.4 kcal/mol above the reactant state (**1b** + **BCF**), while the resultant ion pair **[1b]**$^+$···**[BCFF]**$^-$ is at 20.4 kcal/mol. The latter reactive species has an enhanced ability to react with suitable nucleophiles such as Lewis bases. The conformational space of the $\mathbf{TS^{CF3}}$ was explored, and the most stable transition state and some other selected structures are depicted in Figure S36. The transition state $\mathbf{TS^{CF3}}$**-IV**, corresponding to the previously reported transition state, lies 1 kcal/mol higher in free energy than the $\mathbf{TS^{CF3}}$ resulting from conformational analysis.

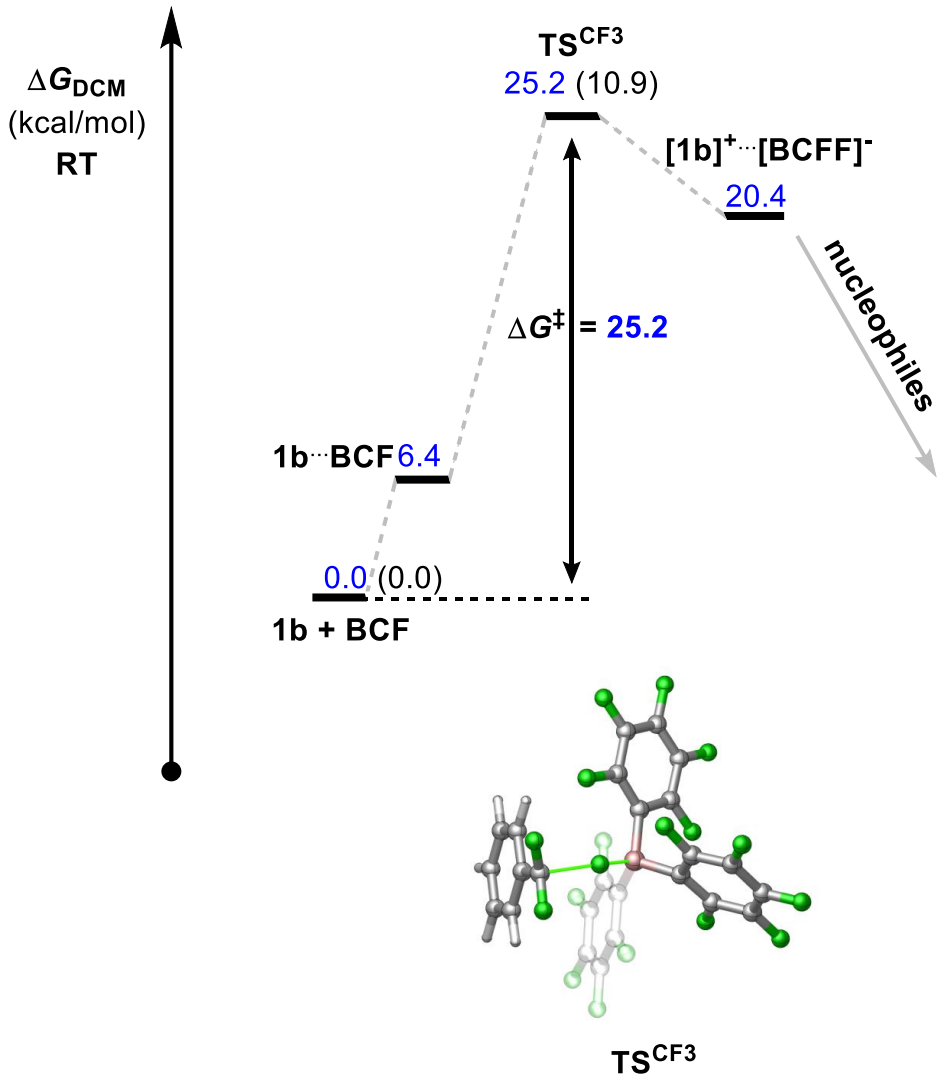

Figure S35. Computed Gibbs free energy profile (Δ*G* in kcal/mol) for the CF_3 group (substrate **1b**) activation via S_N1 mechanism. The relative stability (in blue) is given with respect to **1b** + **BCF** reference state. Relative electronic energies are given within parentheses (computed at the PCM(DCM)-B3LYP-D3/def2TZVPP level).

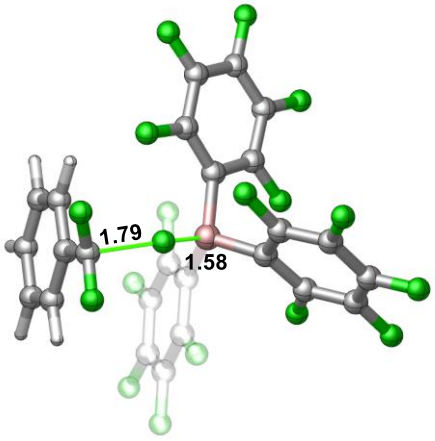

TS^{CF3} (25.2)

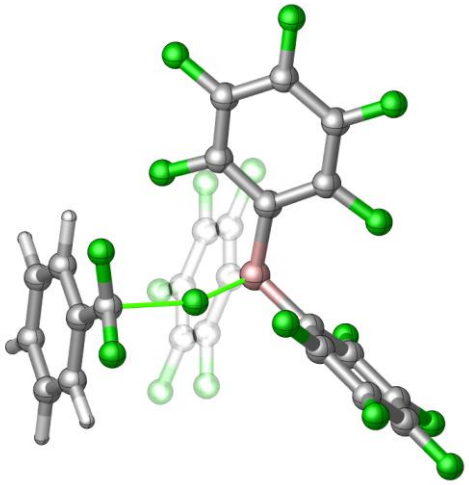

TS^{CF3}-II (25.3)

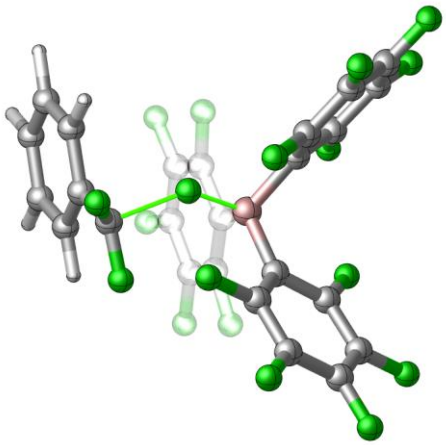

TS^{CF3}-III (25.7)

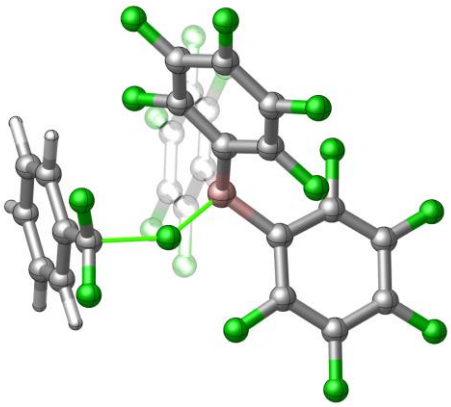

TS^{CF3}-IV (26.2)
(corresponds to Fernandez's TS)

Figure S36. Computationally identified transition states for C-F activation via S_N1 mechanism. The relative stability (in blue) is given with respect to **1b** + **BCF** reference state.

Activation of $PhCF_3$ – FLP-I pathway (using TPPy)

The barrier of C-F bond cleavage with the assistance of **TPPy** was estimated by calculating the free energy distance between the respective transition state and the most stable reactant state (Figure S37). The reactant state was the separate state, that is, **TPPy** + **1b** + **BCF**. Again, the reactive complex of **TPPy**···**1b**···**BCF** was found to be well above the reactant state. Herein, the C-F activation step requires a higher barrier than that on the S_N1 reaction pathway. The free energy gap between the two pathways is 3.4 kcal/mol. The C-F bond cleavage leads to **TPPy**···**[1b]$^+$**···**[BCFF]$^-$** intermediate at 22.9 kcal/mol. In the subsequent step, the **[1b]$^+$** migrates to the **TPPy** (for more details see 'Second step - addition of carbocation onto base' below). The calculations predict that separation of **[1b-TPPy]$^+$**···**[BCFF]$^-$** is thermodynamically disfavoured. It is of note that in the most stable conformer of **[1b-TPPy]$^+$**···**[BCFF]$^-$** ion pair the **[BCFF]$^-$** anion resides close to the positively charged nitrogen atom while the ion pair conformer that is originated directly from the transition state (**[1b-TPPy]$^+$**···**[BCFF]$^-$-II**) is less stable by 12 kcal/mol. Given that several orientations of the **TPPy** are feasible, the conformational space was also explored. Representative transition states from the conformational analysis are indicated in Figure S38.

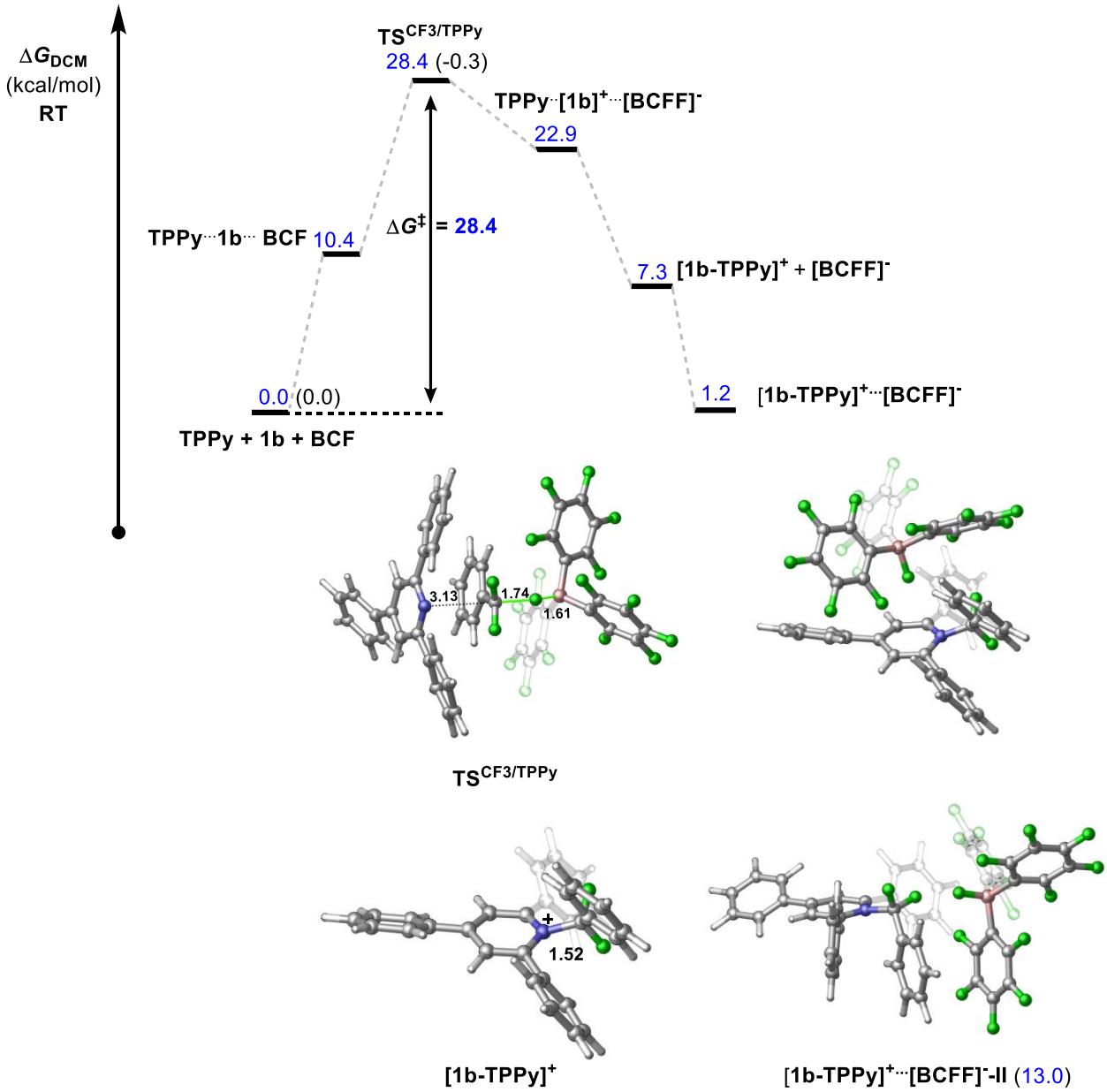

Figure S37. Computed Gibbs free energy profile (Δ*G* in kcal/mol) for the CF_3 group (substrate **1b**) activation with **TPPy** via S_N2 mechanism. The relative stability (in blue) is given with respect to **TPPy** + **1b** + **BCF** reference state. Relative electronic energies are given within parentheses (computed at the PCM(DCM)-B3LYP-D3/def2TZVPP level). Key structures involved in the mechanism are shown with selected bond distances given in Å.

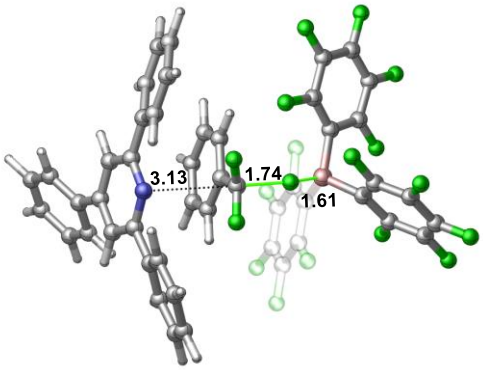

TS$^{CF3/TPPy}$ (28.4)

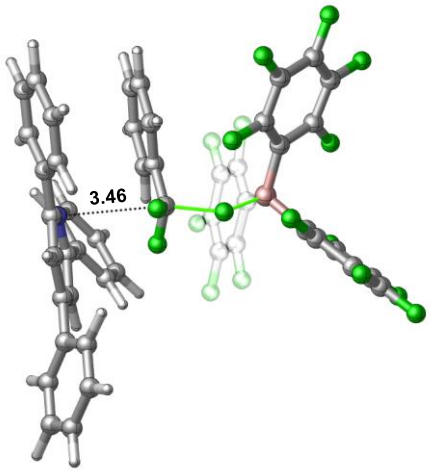

TS$^{CF3/TPPy}$-II (28.6)

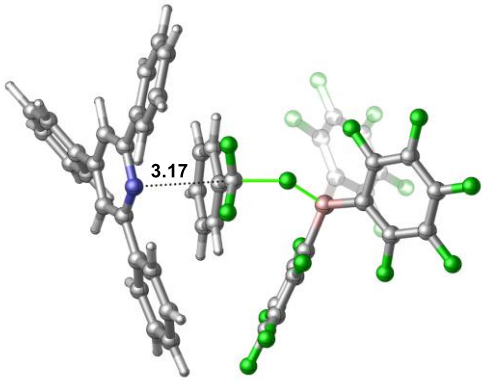

TS$^{CF3/TPPy}$-III (28.8)

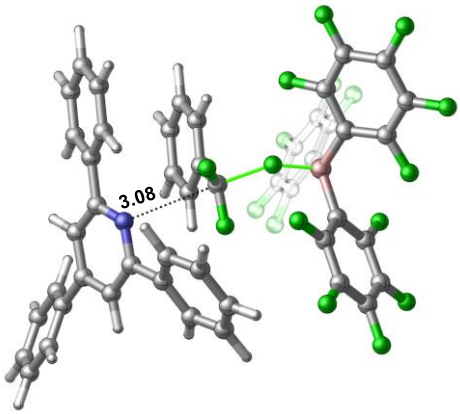

TS$^{CF3/TPPy}$-IV (29.1)
(corresponds to Fernandez's TS)

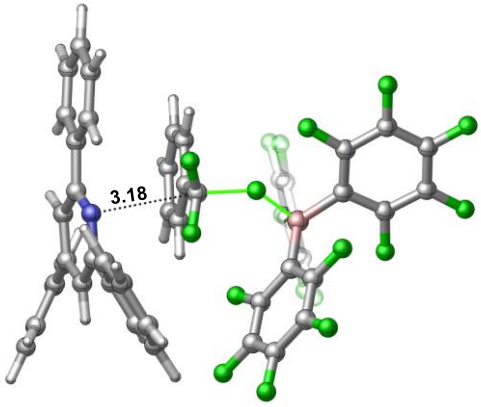

TS$^{CF3/TPPy}$-V (29.3)

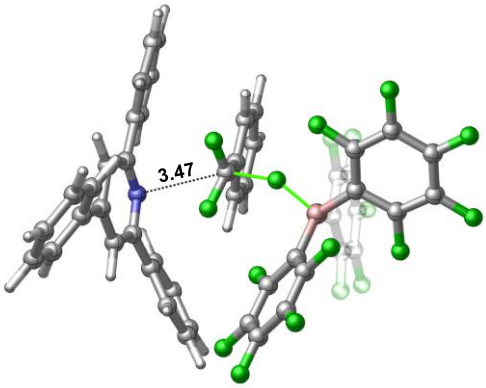

TS$^{CF3/TPPy}$-VI (29.9)

Figure S38. Computationally identified transition states for C-F activation via S_N2 mechanism involving **TPPy**. The relative stability (in blue) is given with respect to **TPPy** + **1b** + **BCF** reference state.

Activation of $PhCF_3$ – FLP-II pathway (using $P(o\text{-}Tol)_3$)

The calculated free energy profile of C-F activation in the presence of **PTol** shows similar features to that with **TPPy** (Figure S39). The overall activation barrier of the C-F bond cleavage is 29.3 kcal/mol, which suggests that the S_N1 process is still preferred. Conformational analysis was carried out as well (Figure S40). In these transition states, the distance between P atom and reactive centre is long (4.21 Å), which indicates that the lone pair of **PTol** does not play a role in the bond cleavage. However, there may be some stabilizing CH/π interaction might be present in the transition state as C-H bond of methyl group in **PTol** points towards the benzene ring of the substrate. Similarly to **TPPy**, a high-lying **PTol**···**[1b]**$^+$···**[BCFF]**$^-$ intermediate was identified along the reaction path. In this intermediate, the **[1b]**$^+$ is expected to be transferred to **PTol** via a small barrier (for details see Section 'Second step - addition of carbocation onto base'). The C-F cleavage leading to **[1b-PTol]**$^+$···**[BCFF]**$^-$ is computed to be an exergonic process. The ion pair in which the **[BCFF]**$^-$ is at the opposite side of CF_2 unit was computed to be slightly more favored (by 1.8 kcal/mol) over the conformer that is directly available from the transition state (**[1b-PTol]**$^+$···**[BCFF]**$^-$**-II**).

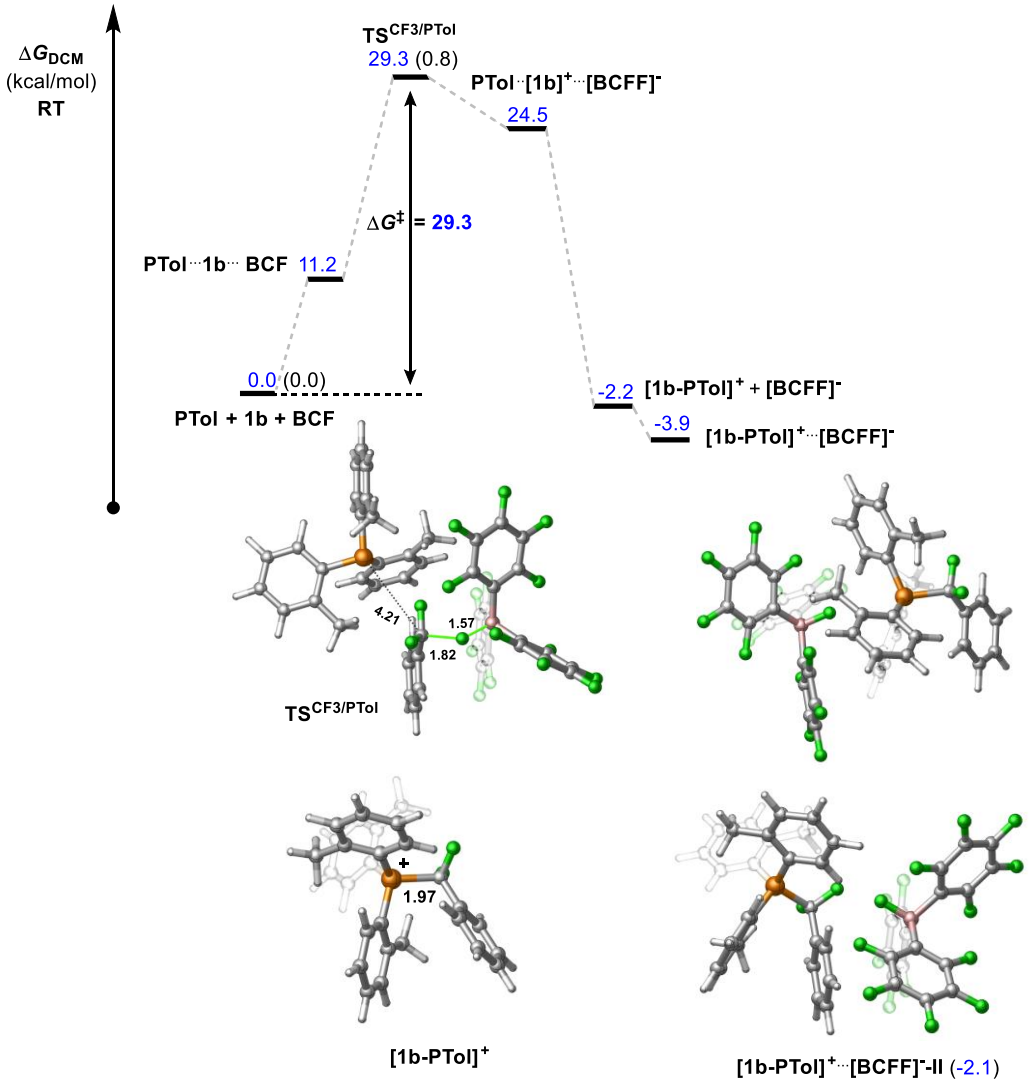

Figure S39. Computed Gibbs free energy profile (Δ*G* in kcal/mol) for the CF_3 group (substrate **1b**) activation with **PTol** via S_N2 mechanism. The relative stability (in blue) is given with respect to **PTol** + **1b** + **BCF** reference state. Key structures involved in the mechanism are shown with selected bond distances given in Å. Relative electronic energies are given within parentheses (computed at the PCM(DCM)-B3LYP-D3/def2TZVPP level).

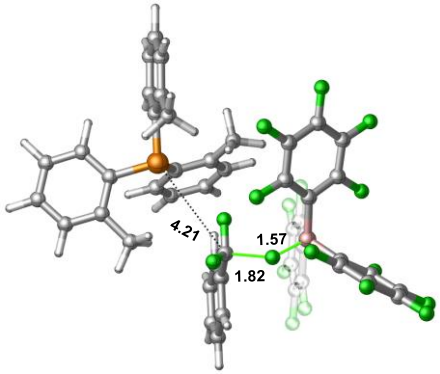

TS$^{CF3/PTol}$ (29.3)

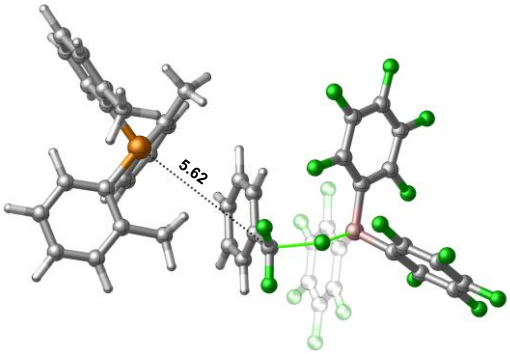

TS$^{CF3/PTol}$**-II** (29.7)

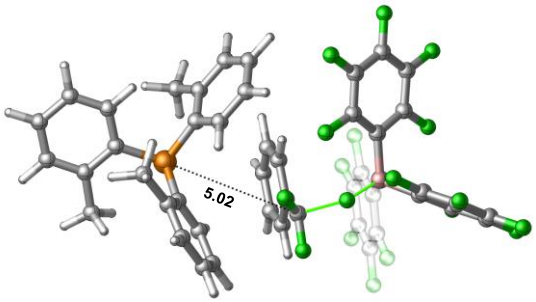

TS$^{CF3/PTol}$**-III** (29.8)

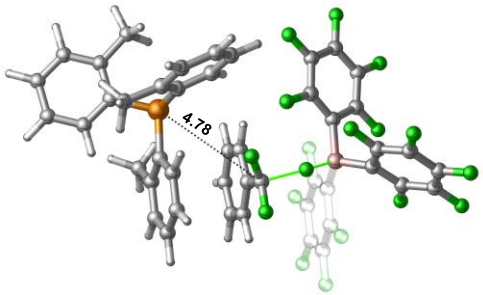

TS$^{CF3/PTol}$**-IV** (30.0)

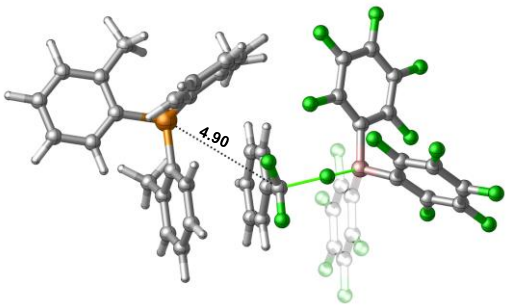

TS$^{CF3/PTol}$**-V** (30.2)

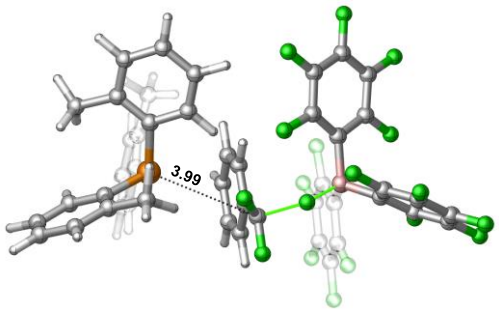

TS$^{CF3/PTol}$**-VI** (36.3)

Figure S40. Computationally identified transition states for C-F activation via S_N2 mechanism involving **PTol**. The relative stability (in blue) is given with respect to **PTol** + **1b** + **BCF** reference state.

Activation of $PhCF_3$ – FLP-III pathway (using THT)

The transition state **TS**$^{CF3/THT}$ associated with the THT-assisted C-F bond cleavage is predicted to have a 31.4 kcal/mol energy barrier relative to **THT** + **1b** + **BCF** state (Figure S41). When considering that THT forms a stable complex with BCF, the overall barrier is 32.3 kcal/mol, hence this barrier related to S_N2 process is insurmountable at ambient temperature. Interestingly, a high-lying carbocation intermediate could not be found, that is, the **[1b]**$^+$ species directly reacted with **THT** along the reaction pathway. The formation of the **[1b-THT]**$^+$···**[BCFF]**$^-$ is notably endergonic. In the most stable form of the **[1b-PTol]**$^+$···**[BCFF]**$^-$ ion pair, the **[BCFF]**$^-$ anion is in close proximity to the sulfonium cation.

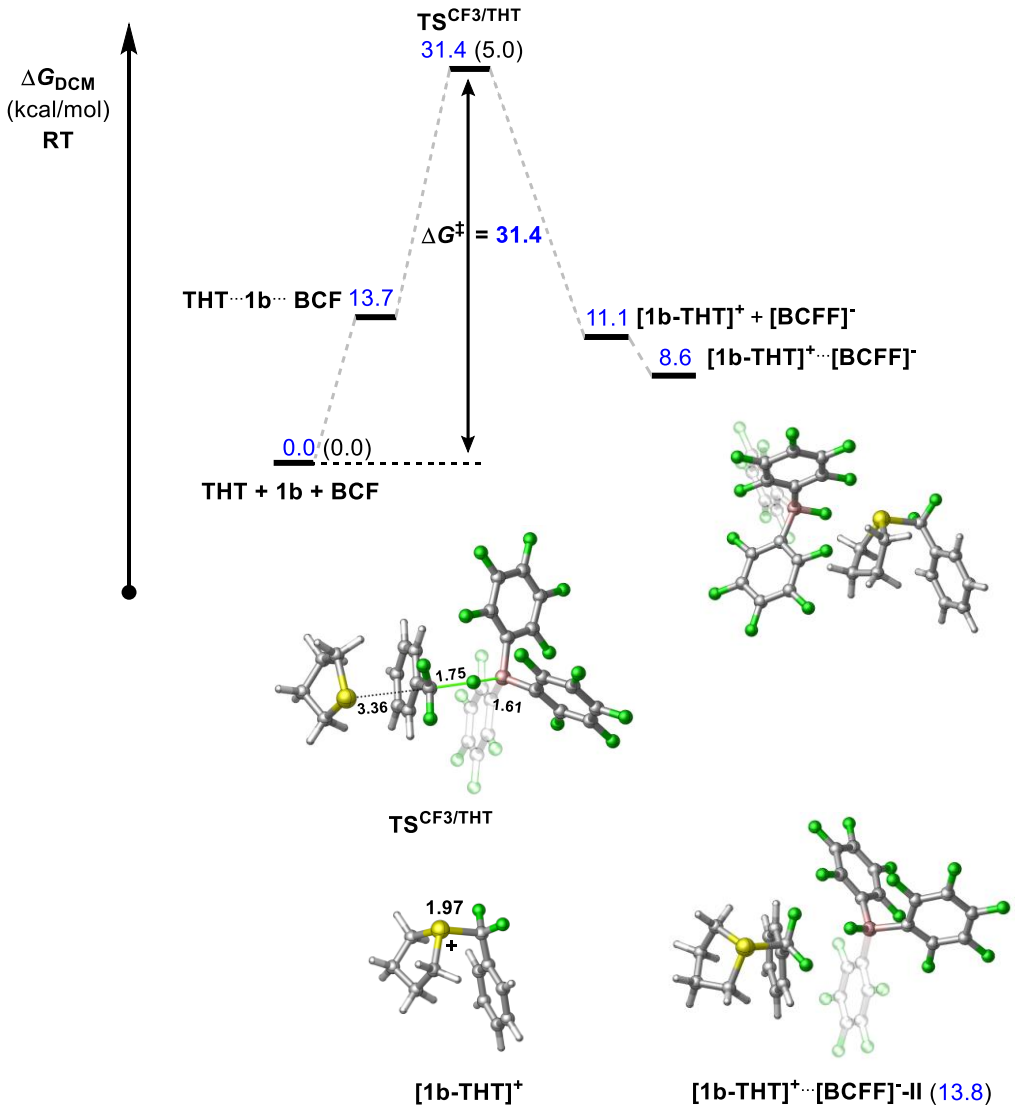

Figure S41. Computed Gibbs free energy profile (Δ*G* in kcal/mol) for the CF_3 group (substrate **1b**) activation with **THT** via S_N2 mechanism. The relative stability (in blue) is given with respect to **THT** + **1b** + **BCF** reference state. Relative electronic energies are given within parentheses (computed at the PCM(DCM)-B3LYP-D3/def2TZVPP level). Key structures involved in the mechanism are shown with selected bond distances given in Å.

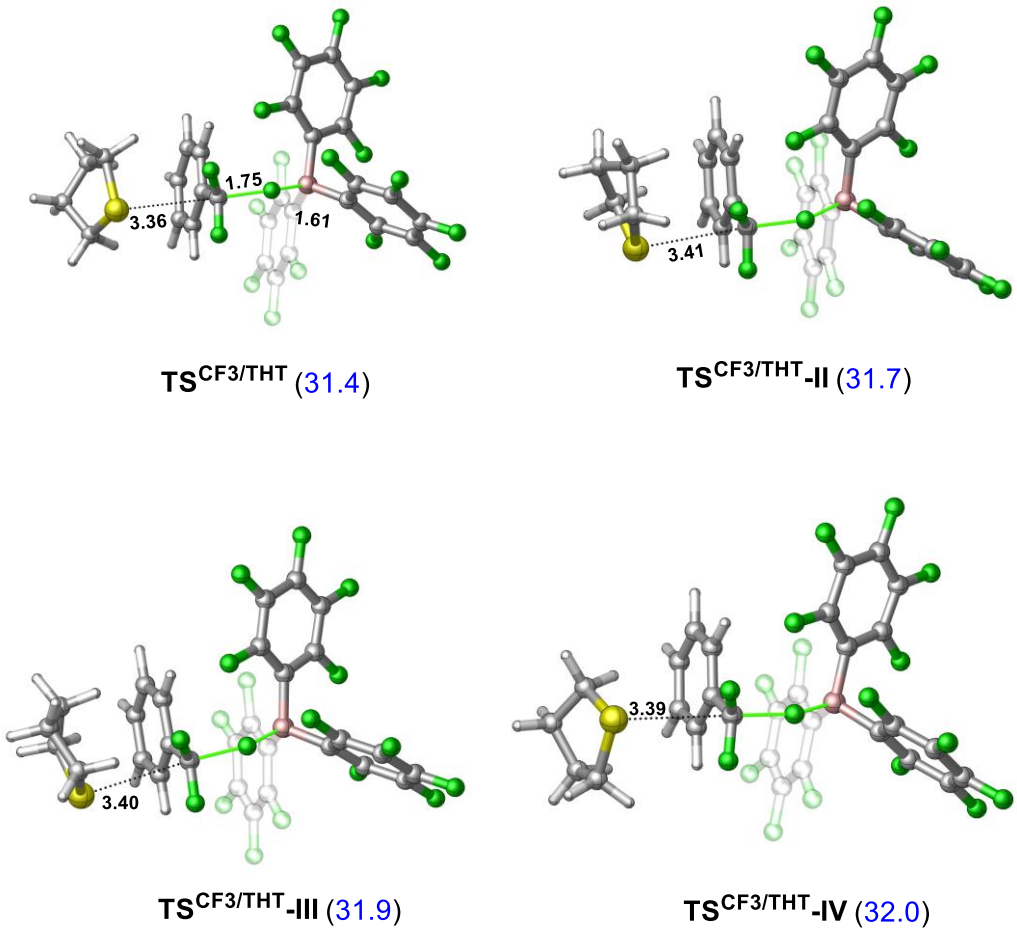

TS$^{CF3/THT}$ (31.4)

TS$^{CF3/THT}$-II (31.7)

TS$^{CF3/THT}$-III (31.9)

TS$^{CF3/THT}$-IV (32.0)

Figure S42. Computationally identified transition states for C-F activation via S_N2 mechanism involving **THT**. The relative stability (in blue) is given with respect to **THT** + **1b** + **BCF** reference state.

Activation of $PhCF_2H$ – S_N1 pathway

The activation of the CHF_2 group was found to be more facile based on the computed barrier heights. On the S_N1 pathway, the C-F bond cleavage is accessible through an activation barrier of only 18.9 kcal/mol. The resultant **[2b]$^+$···[BCFF]$^-$** can react with the Lewis bases to form the product. We found that there is a favourable H-bonding interaction between the substrate C(F)-H and the F atom in the aromatic ring of the **BCF**.

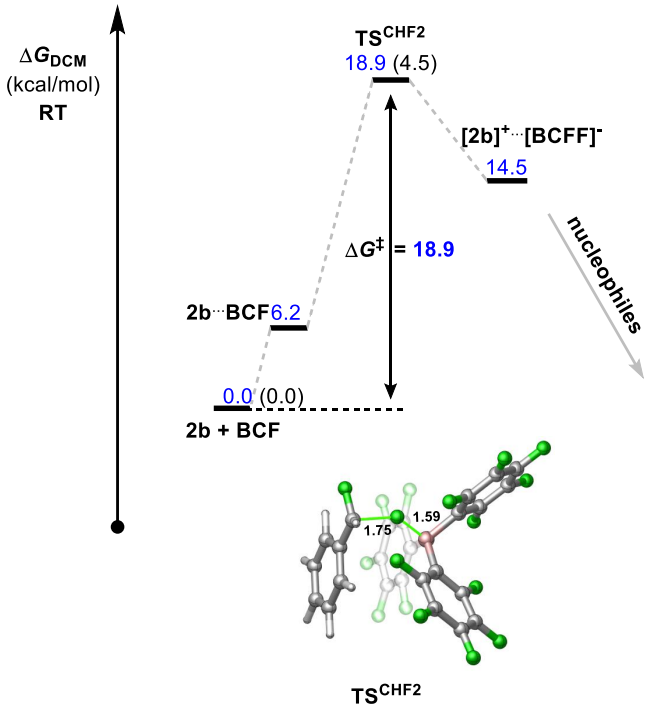

Figure S43. Computed Gibbs free energy profile (Δ*G* in kcal/mol) for the CF_3 group (substrate **1b**) activation via S_N1 mechanism. The relative stability (in blue) is given with respect to **2b** + **BCF** reference state. Relative electronic energies are given within parentheses (computed at the PCM(DCM)-B3LYP-D3/def2TZVPP level).

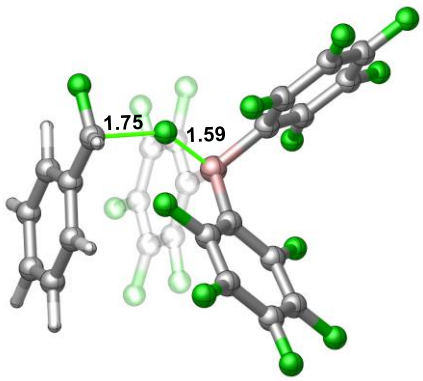

TS^{CHF2} (18.9)

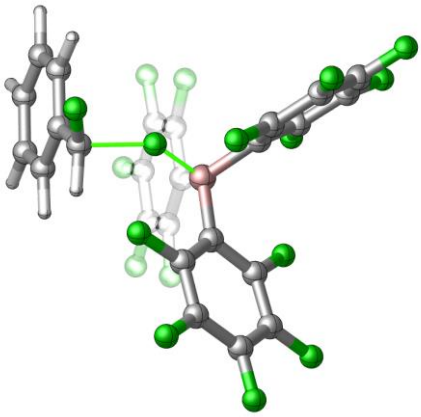

TS^{CHF2}-II (19.2)

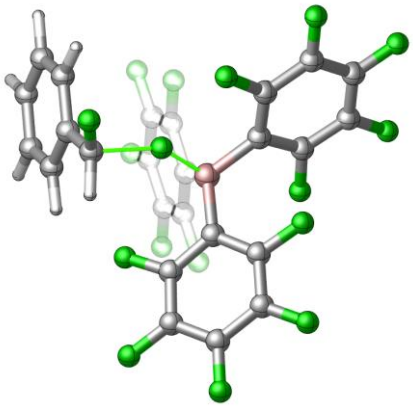

TS^{CHF2}-III (20.1)

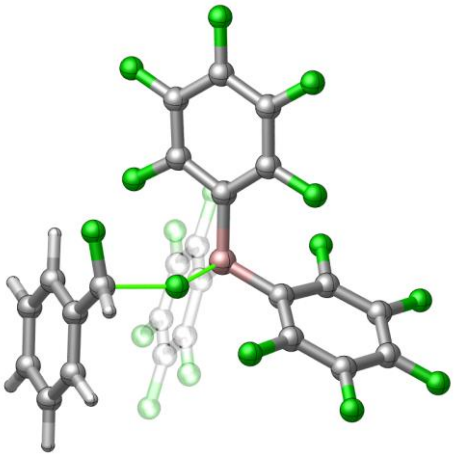

TS^{CHF2}-IV (21.2)

Figure S44. Computationally identified transition states for C-F activation via S_N1 mechanism. The relative stability (in blue) is given with respect to **2b** + **BCF** reference state.

Activation of $PhCF_2H$ – FLP-I pathway (using TPPy)

The energy barrier associated with the most favored transition state leading to the high-lying intermediate is 20.2 kcal/mol (see Figure S45). The conformational analysis provided several transition states which are shown in Figure S46. In the case of substrate **2b**, the computed free energy difference between the S_N1 and S_N2 pathway is smaller, it is only 1.3 kcal/mol, which may be attributed to an enhanced π-π interaction in the S_N2 transition state. In the following step, the carbocation **[2b]$^+$** reacts with the **TPPy** in an exergonic fashion.

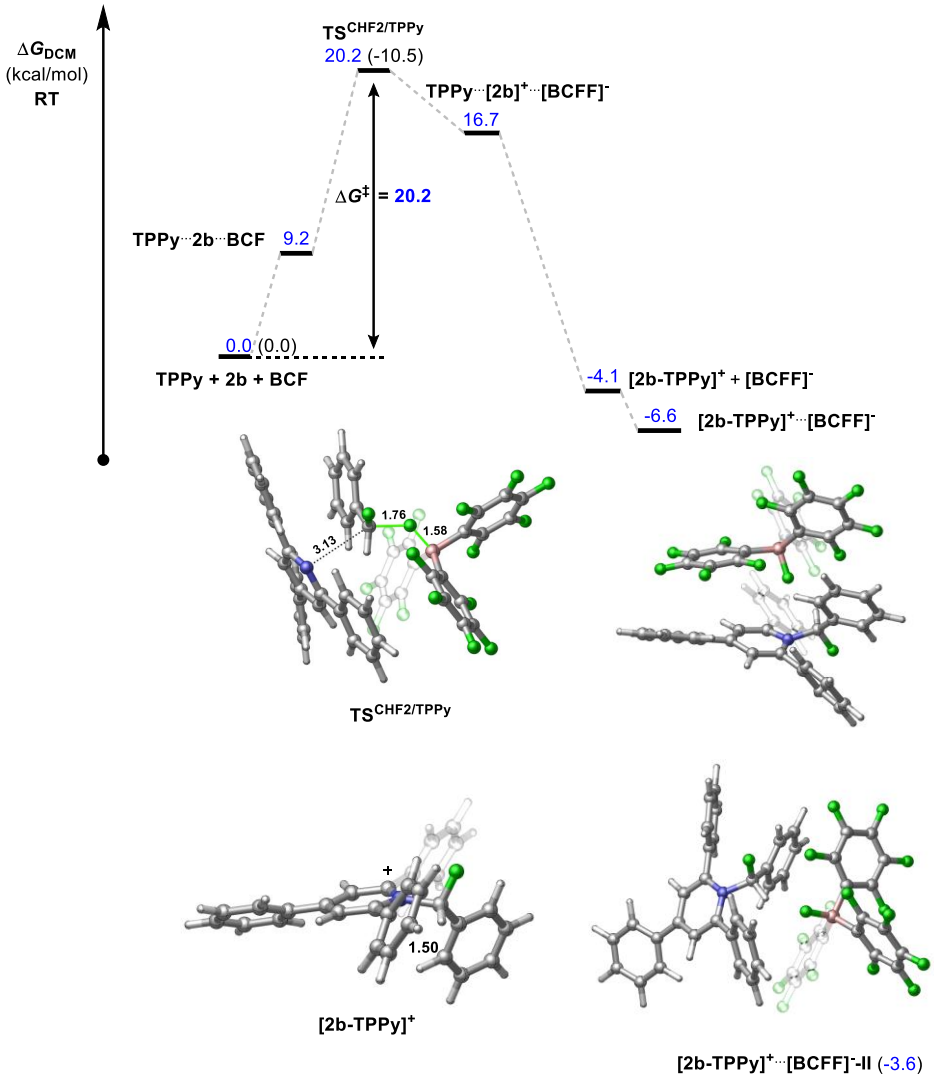

Figure S45. Computed Gibbs free energy profile (Δ*G* in kcal/mol) for the CHF_2 group (substrate **2b**) activation with **TPPy** via S_N2 mechanism. The relative stability (in blue) is given with respect to **TPPy** + **2b** + **BCF** reference state. Relative electronic energies are given within parentheses (computed at the PCM(DCM)-B3LYP-D3/def2TZVPP level). Key structures involved in the mechanism are shown with selected bond distances given in Å.

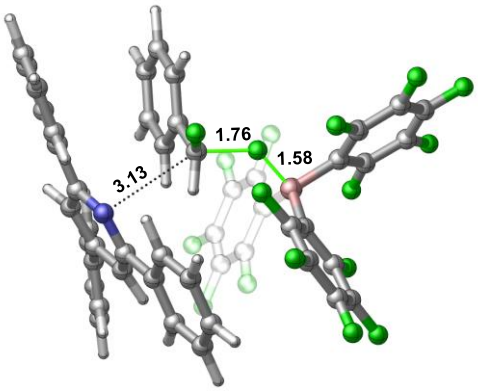

TS$^{CHF2/TPPy}$ (20.2)

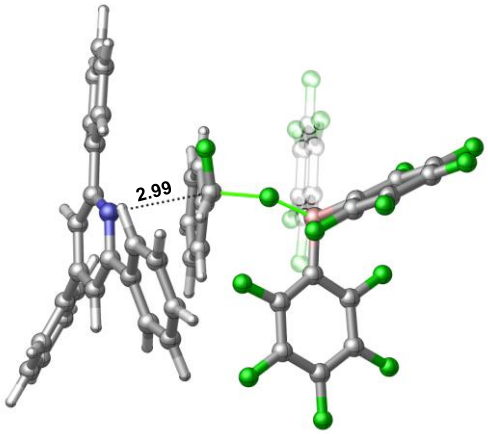

TS$^{CHF2/TPPy}$-II (21.1)

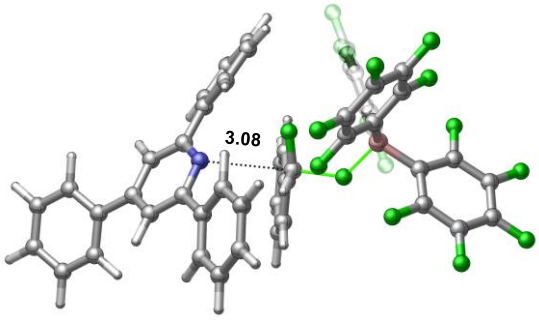

TS$^{CHF2/TPPy}$-III (21.8)

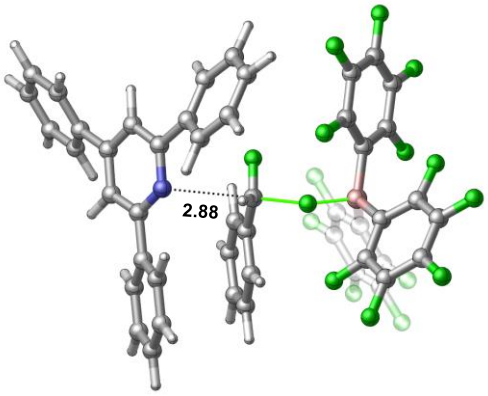

TS$^{CHF2/TPPy}$-IV (23.3)

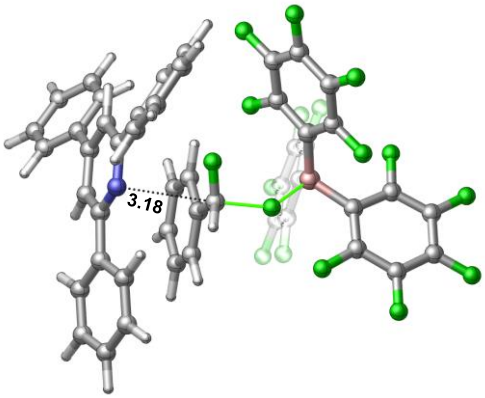

TS$^{CHF2/TPPy}$-V (24.2)

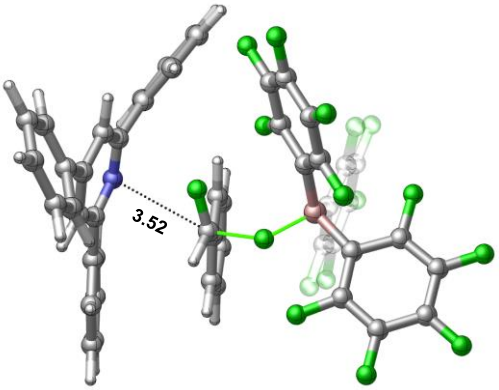

TS$^{CHF2/TPPy}$-VI (25.3)

Figure S46. Computationally identified transition states for C-F activation via S_N2 mechanism involving **TPPy**. The relative stability (in blue) is given with respect to **TPPy** + **2b** + **BCF** reference state.

H-Bonding assisted S_N1 activation of 2b

A reaction pathway involving hydrogen bonding between a CF_2H H-bond donor and a TPPy H-bond acceptor was explored (S47). The pathway is closely related to an S_N1 pathway (see Figure S43), with the main difference being that TPPy is involved in the transition state through a H-bonding interaction with the CF_2H hydrogen. It was calculated that such an interaction reduced the barrier for C-F activation by up to 0.5 kcal mol^{-1}. However, no direct rate dependence was found for TPPy concentration, implying that this interaction may not be active for all substrates and the calculated stabilization of the transition state is within the accepted error for our DFT methods.

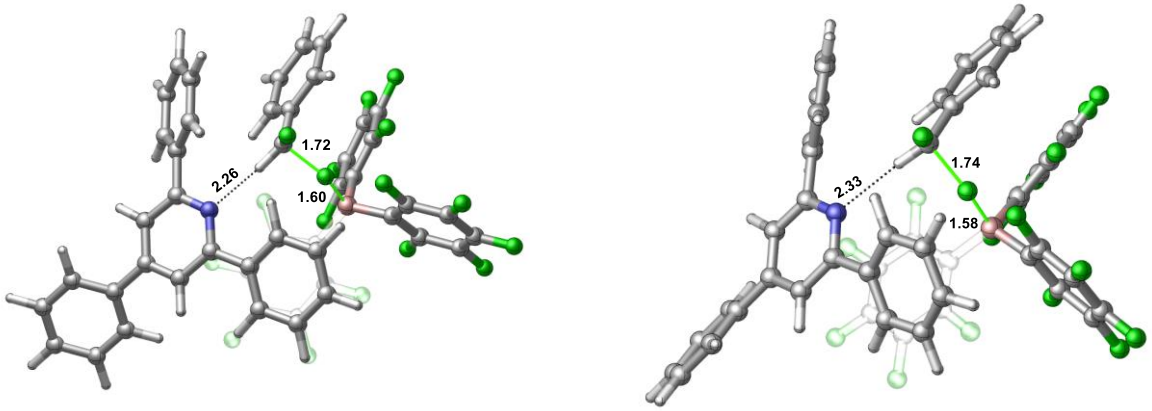

$TS^{CHF2/TPPy/H}$-I (18.4) **$TS^{CHF2/TPPy/H}$-II** (18.6)

Figure S47. Computationally identified transition states for C-F activation via S_N2 mechanism when TPPy features a H-bond with CHF_2 moiety. The relative stability (in blue) is given with respect to **TPPy** + **2b** + **BCF** reference state.

Activation of $PhCF_2H$ – FLP-II pathway (using $P(o\text{-}Tol)_3$)

In the S_N2 reaction with **PTol**, the transition state $\mathbf{TS^{CHF2/PTol}}$ was estimated to lie at 21.1 kcal/mol. The structure of $\mathbf{TS^{CHF2/PTol}}$ is analogous to that of $\mathbf{TS^{CF3/PTol}}$ (for further transition states see Figure S48). The overall reaction was calculated to be highly exergonic (-15.3 kcal/mol).

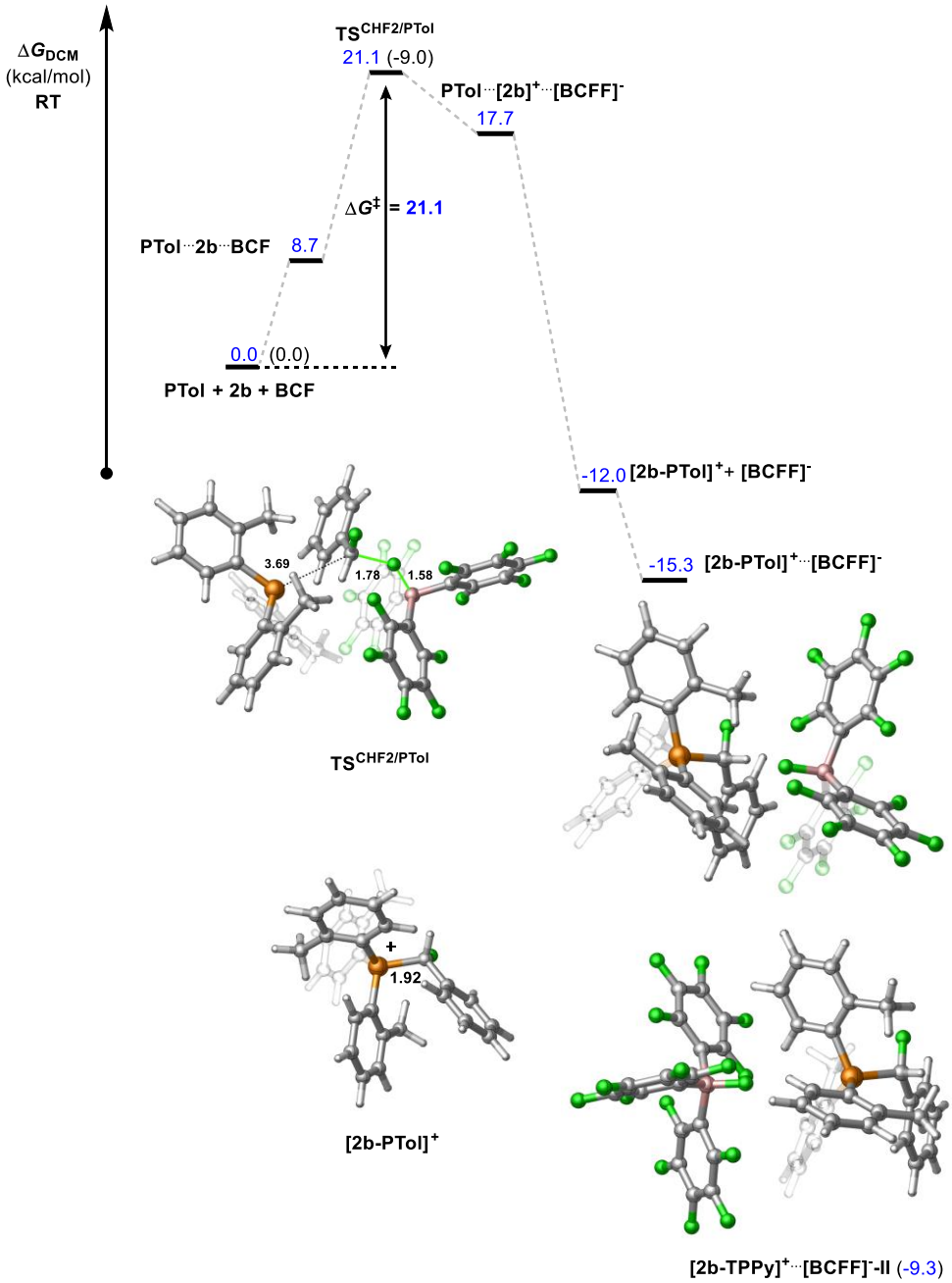

Figure S48. Computed Gibbs free energy profile (Δ*G* in kcal/mol) for the CHF_2 group (substrate **2b**) activation with **PTol** via S_N2 mechanism. The relative stability (in blue) is given with respect to **PTol** + **2b** + **BCF** reference state.

Relative electronic energies are given within parentheses (computed at the PCM(DCM)-B3LYP-D3/def2TZVPP level). Key structures involved in the mechanism are shown with selected bond distances given in Å.

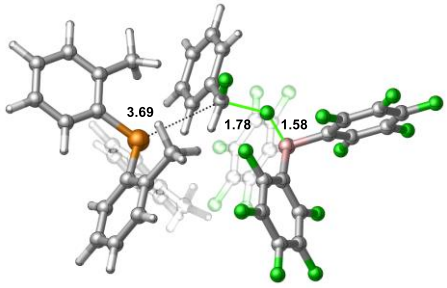

TS$^{CHF2/PTol}$ (21.1)

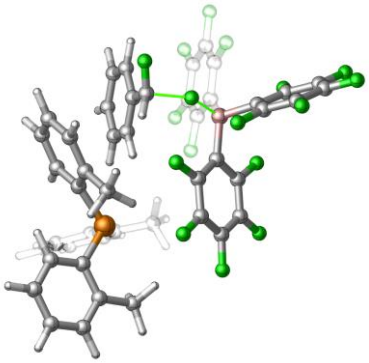

TS$^{CHF2/PTol}$-II (22.3)

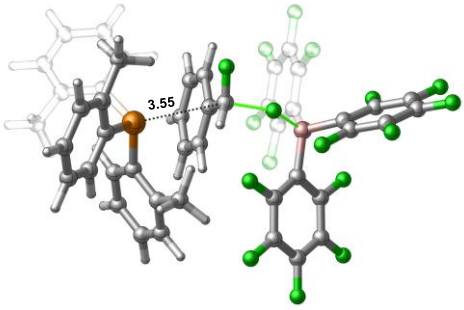

TS$^{CHF2/PTol}$-III (23.3)

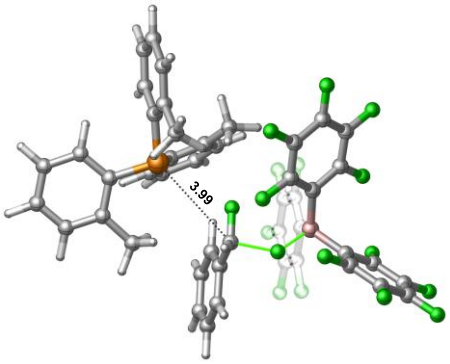

TS$^{CHF2/PTol}$-IV (23.6)

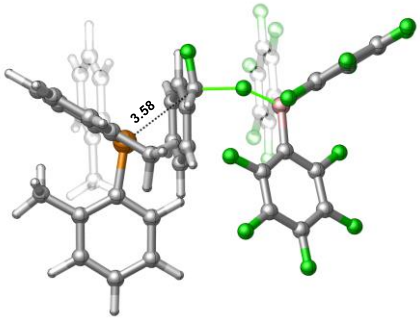

TS$^{CHF2/PTol}$-V (27.5)

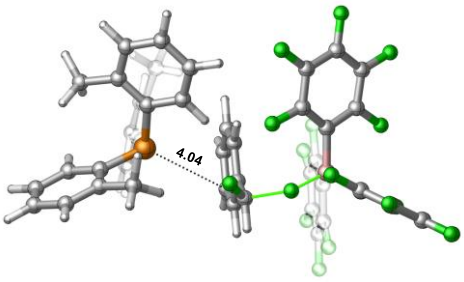

TS$^{CHF2/PTol}$-VI (31.7)

Figure S49. Computationally identified transition states for C-F activation via S_N2 mechanism involving **PTol**. The relative stability (in blue) is given with respect to **PTol** + **2b** + **BCF** reference state.

Activation of $PhCF_2H$ – FLP-III pathway (using THT)

The calculated activation free energy represented by the **TS$^{CHF2/THT}$** is 24.2 kcal/mol with respect to **THT** +**2b** + **BCF** state (Figure S50), which is 5.3 kcal/mol higher as compared to the S_N1 transition state. Again, the overall barrier is even higher when taking into the favourable **THT-BCF** formation. Other representative transition states emerged from the conformational analysis are shown in Figure S51.

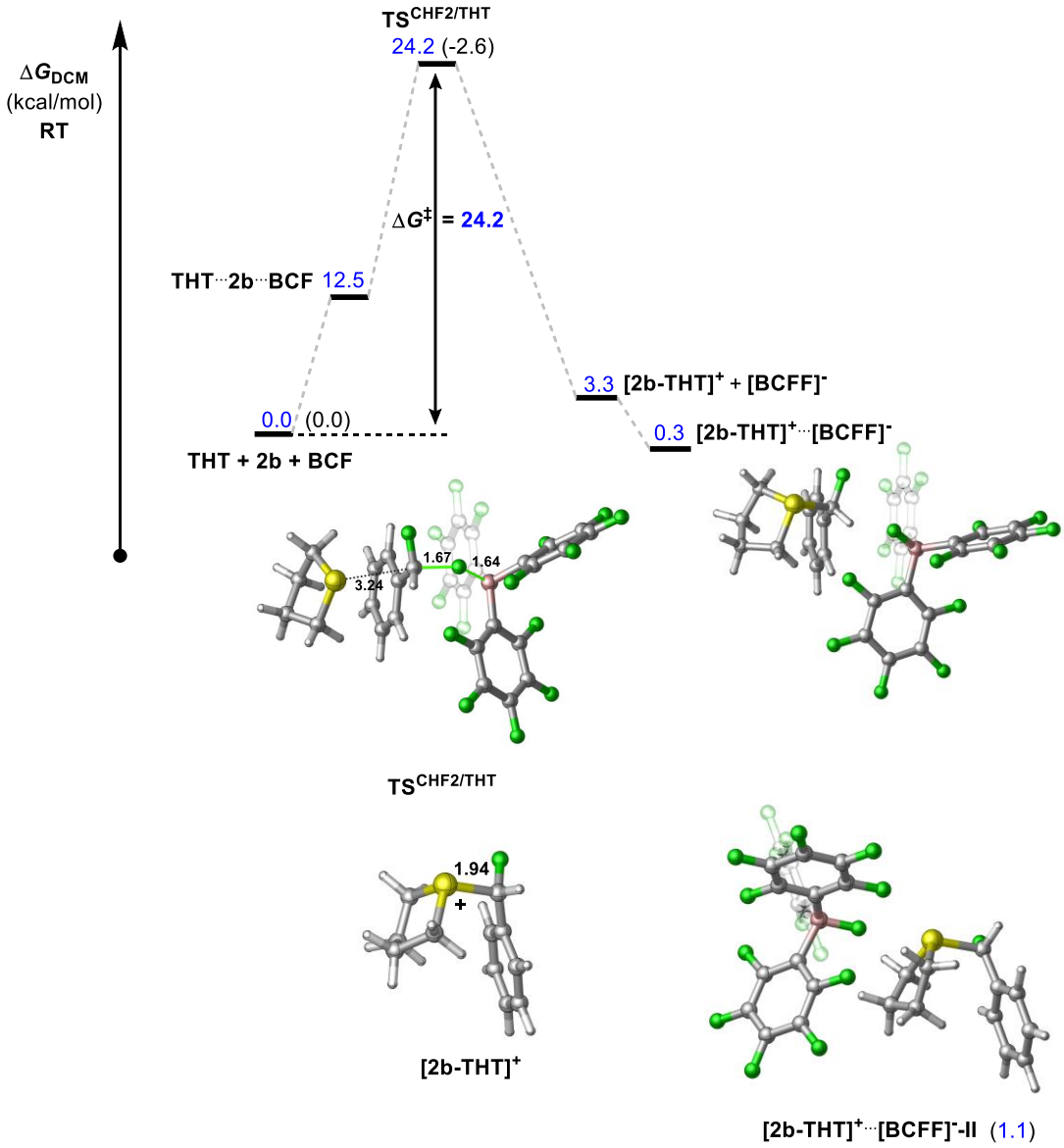

Figure S50. Computed Gibbs free energy profile (Δ*G* in kcal/mol) for the CHF_2 group (substrate **2b**) activation with **THT** via S_N2 mechanism. The relative stability (in blue) is given with respect to **THT** + **2b** + **BCF** reference state. Relative electronic energies are given within parentheses (computed at the PCM(DCM)-B3LYP-D3/def2TZVPP level). Key structures involved in the mechanism are shown with selected bond distances given in Å.

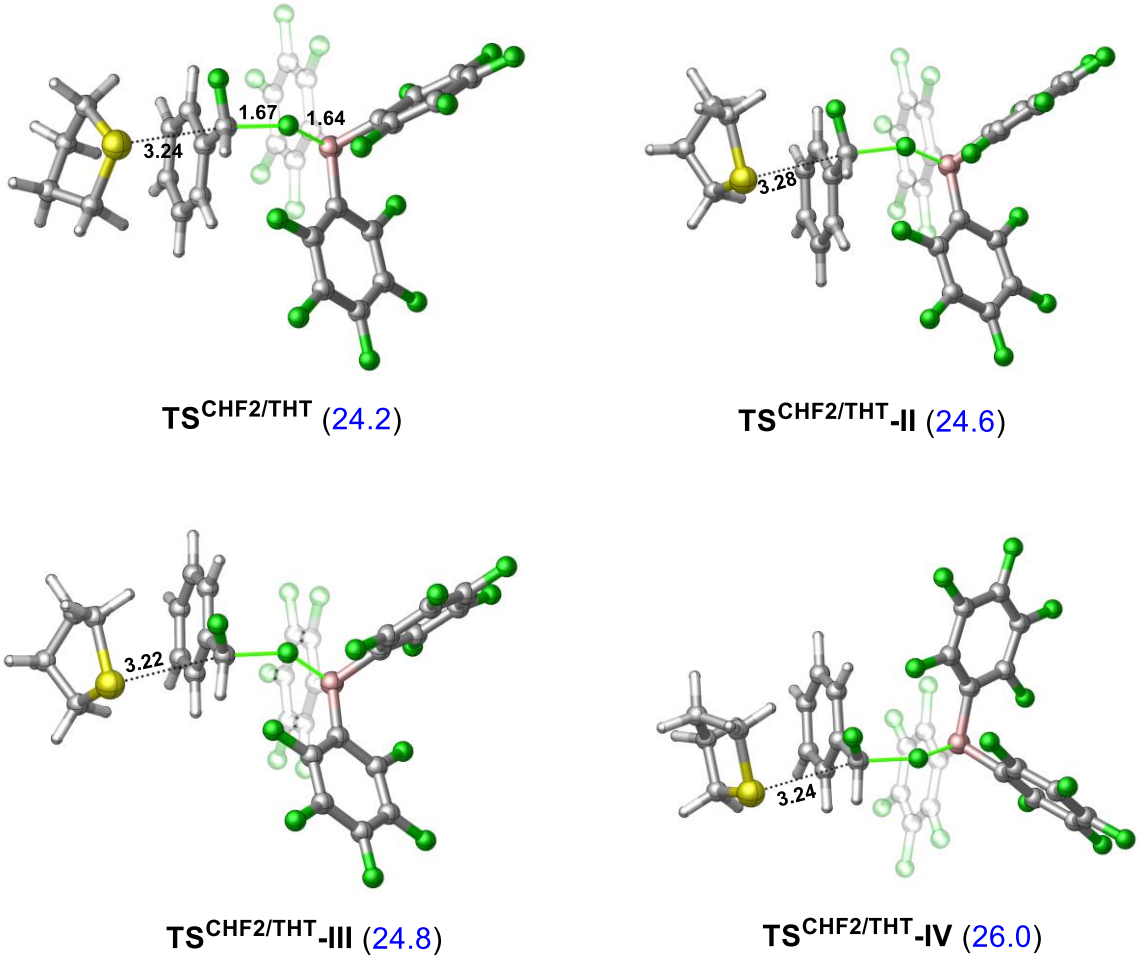

TS$^{CHF2/THT}$ (24.2)

TS$^{CHF2/THT}$-II (24.6)

TS$^{CHF2/THT}$-III (24.8)

TS$^{CHF2/THT}$-IV (26.0)

Figure S51. Computationally identified transition states for C-F activation via S_N2 mechanism involving **THT**. The relative stability (in blue) is given with respect to **THT** + **2b** + **BCF** reference state.

TMSF formation from $TMSNTf_2$ and $[BF(C_6F_5)_3]^-$

The most stable isomer is **$TMSNTf_2$** which is predicted to be *ca*. 2 kcal/mol more favoured over the other investigated isomers (Figure S52). In the most stable isomer, NTf_2 anion coordinates to the TMS unit through the O atom, and the neighbouring O atom is also in a close proximity to the silicon centre. In isomer **$TMSNTf_2$-II**, which 2.1 kcal/mol less stable, the latter O atom is pointing away from the Si atom. The N-bound isomer **$TMSNTf_2$-III** was found to be 2.2 kcal/mol above the most stable isomer.

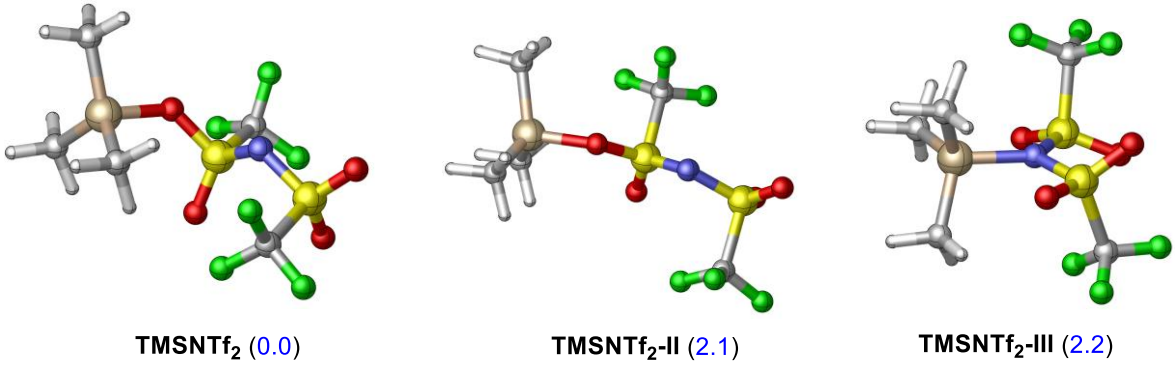

Figure S52. DFT-optimized structures of **$TMSNTf_2$**. The relative stability (in blue) is given in kcal/mol

The TMSF from the reaction between **$[BCFF]^-$** and **$TMSNTf_2$** drives the reaction to the product side, as its formation is thermodynamically highly favourable (-14.2 kcal/mol). The transition state corresponds to abstraction of the F- anion from the **$[BCFF]^-$** by **$TMSNTf_2$** could not been identified, but we could obtain a pentacoordinate intermediate **$[BCF\text{-}F\text{-}TMSNTf2]^-$** as an energy minimum (Figure S53). This intermediate lies above the dissociated state by 7.4 kcal/mol. Given that many attempts to locate the transition state leading to TMF was unsuccessful, we hypothesize that the transition state in question is close to the free energy of **$[BCF\text{-}F\text{-}TMSNTf2]^-$** intermediate. This notion was corroborated by performing constraint geometry optimisation which showed that the barrier should be about 2 kcal/mol from the intermediate state.

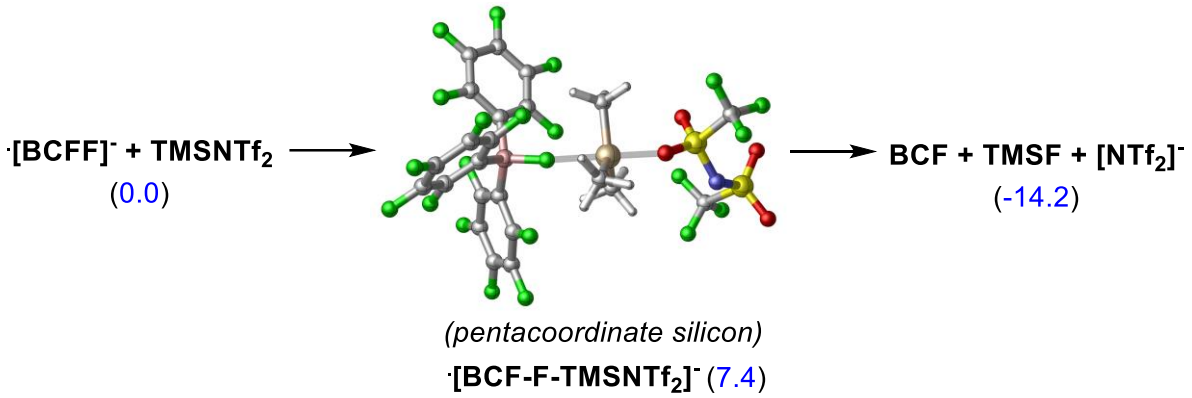

Figure S53. The process of **BCF** regeneration with **$TMSNTf_2$.** The relative stability (in blue) is given in kcal/mol with respect to **$[BCFF]^-$** + **$TMSNTf_2$**.

Activation pathways for 4-Me-$C_6H_4(CF_3)$ (1a)

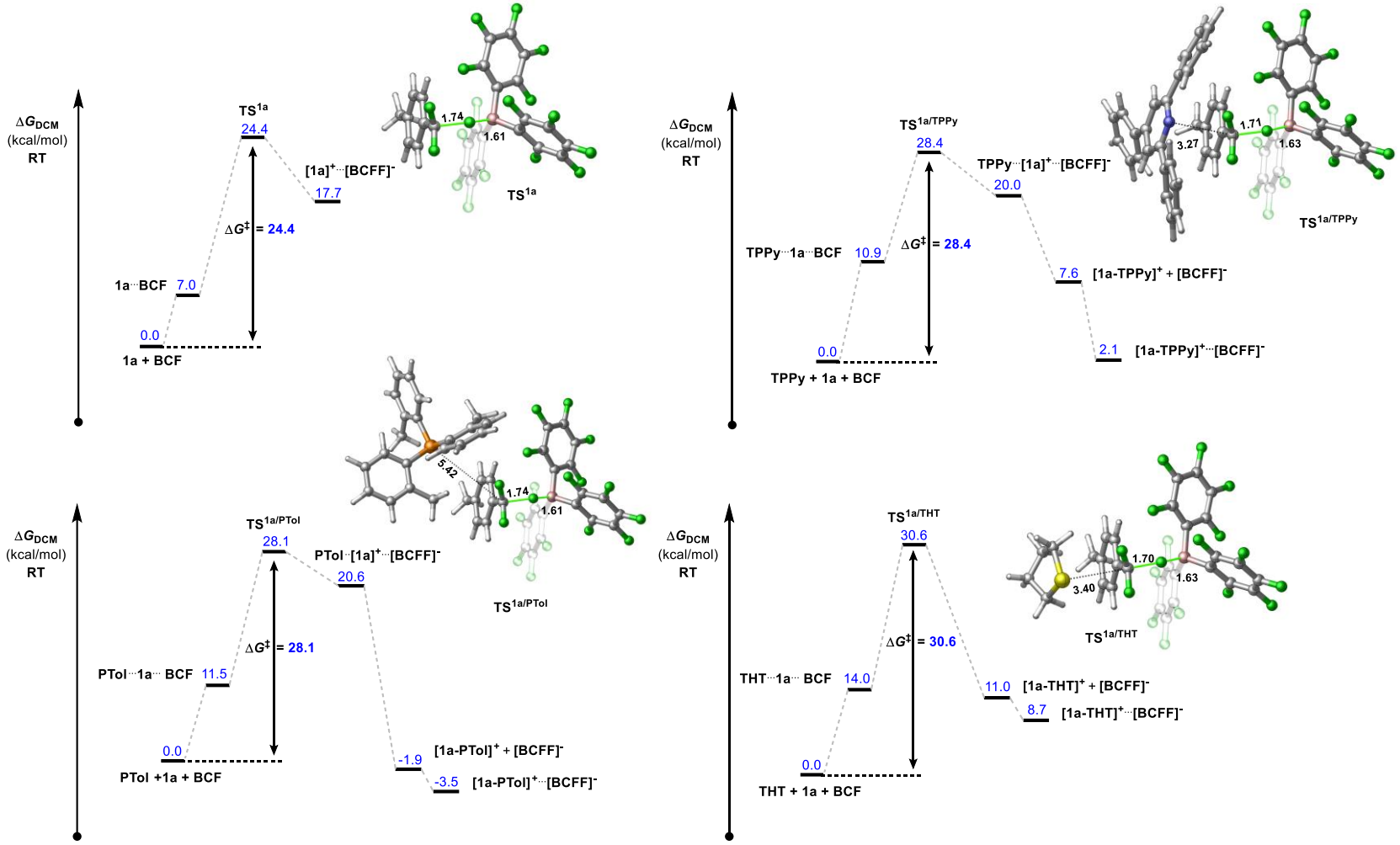

Figure S54. Computationally identified transition states for C-F bond activation in the case of substrate **1a**. Computed barriers are given in kcal/mol (in blue) with respect to the corresponding reactant states indicated at the start of the mechanism. Selected bond distances of TSs are given in Å.

CF-bond activation with $TMSNTf_2$

We also considered the mechanistic scenario in which the **$TMSNTf_2$** acts as a Lewis acid in the process of C-F activation (Figure S55). The corresponding transition states were identified for substrates **1b** and **2b**. In both cases, the reaction barriers associated with the mechanism involving **$TMSNTf_2$** are predicted to be disfavored by 5 kcal/mol in comparison with reaction pathway with **BCF**.

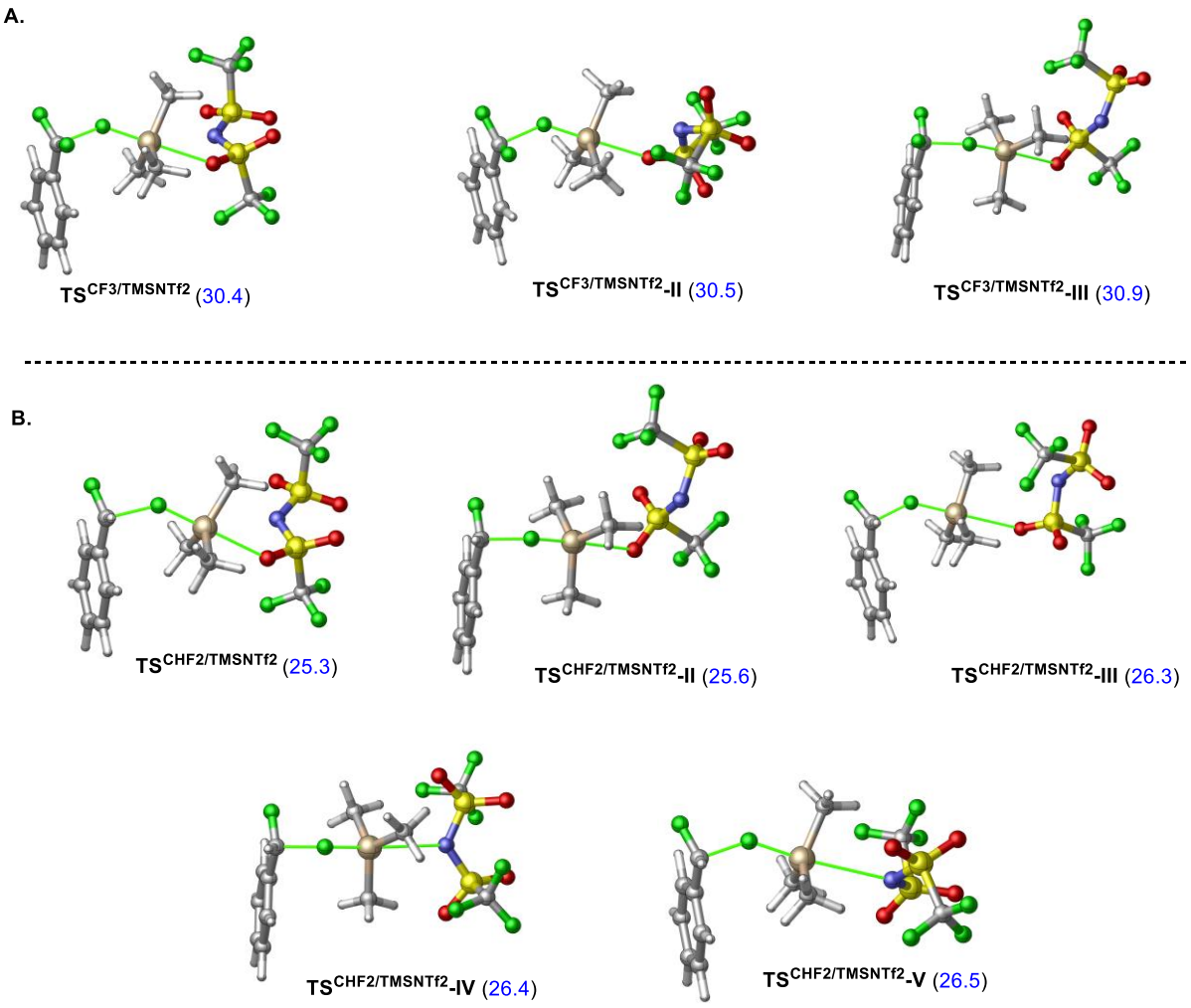

Figure S55. Computationally identified transition states for C-F bond activation with **$TMSNTf_2$.** The relative stability (in blue) is given in kcal/mol with respect to **1b/2b** + **$TMSNTf_2$**.

Activation of BnF via a S_N1 pathway

The C-F becomes more accessible in the case of benzyl fluoride, as shown by the decreased barrier (Figure S56). The computed barrier was rather low as **TS^{CH2F}** was found to be 13.5 kcal/mol above the reactant state.

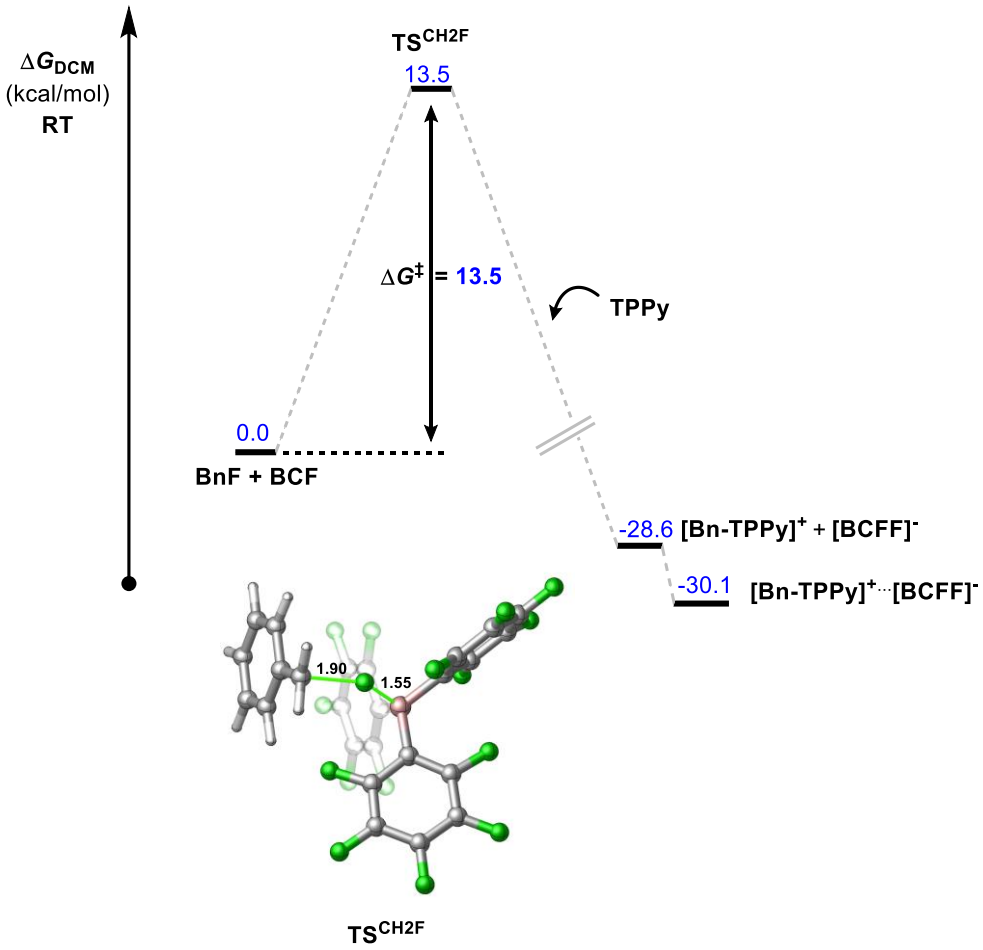

Figure S56. Computed Gibbs free energy profile (Δ*G* in kcal/mol) for the CH_2F group (substrate **BnF**) activation via S_N1 mechanism. The relative stability (in blue) is given with respect to **BnF** + **BCF** reference state.

Second step – addition of carbocation onto base (TPPy, PTol, THT)

To investigate the steps after C-F bond cleavage, we next turned our attention toward the addition of carbocation to the Lewis base which results in the **[1b-LB]$^+$···[BCFF]$^-$** ion pair.

First, we attempted to identify the transition states in the case of **TPPy** + **1b** that describes such a mechanistic process. The resultant carbocation in complex **TPPy**···**[1b]$^+$**···**[BCFF]$^-$** moves to **TPPy** via transition state of **TS$^{[1b]+/TPPy}$** with a barrier of 25.0 kcal/mol (Figure S57). This barrier height is slightly below the barrier needed for C-F activation. We attempted to locate a transition state which corresponds to the addition of carbocation **[1b]$^+$** to the **TTPy** in the absence of **[BCFF]$^-$** anion. Such a transition state could not be identified as the optimisation failed to converge. However, this barrier was estimated by the free energy required to form the separate **[1b]$^+$** cation. The separate state **[1b]$^+$** + **[BCFF]$^-$** lies above the reactant state by 24.5 kcal/mol. This intermediate state is 0.7 kcal/mol lower than that of the C-F bond activation, and only 0.5 kcal/mol more stable compared to the **TS$^{[1b]+/TPPy}$**.

Mindful of the accuracy of DFT, it is difficult to decipher which mechanism is prevailing regarding the formation of **TPPy**···**[1b]$^+$**.

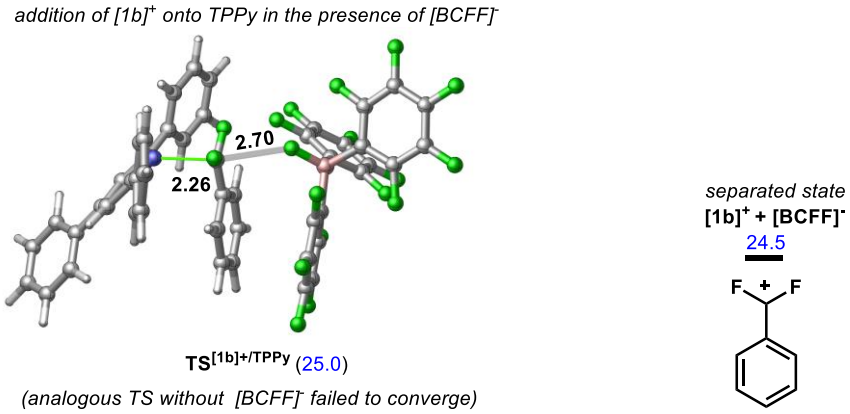

Figure S57. Transition state related to the addition of carbocation and the separate state. The relative stability (in blue) is given with respect to **TPPy** + **1b** + **BCF** reference state.

Analogous transition state with PTol was also attempted to identify. In this case, the reactive centre of the carbocation **[1b]$^+$** is not directly orientated towards the P atom, and the atomic distance between C and P atom is rather long. As a result, we could not locate a transition state analogous to **TS$^{[1b]+/TPPy}$**. The constraint geometry optimisations revealed that a small conformational change in complex **PTol**···**[1b]$^+$**···**[BCFF]$^-$** can lead to the facile formation of **[1b-PTol]$^+$**.

The resulting intermediate encompassing PTol after C-F activation lies at 24.5 kcal/mol (Figure S58). The intermediate **PTol**···**[1b]**$^{+}$···**[BCFF]**$^{-}$ originates from the most stable transition state **TS**$^{PTol/CF3}$ lying at 29.3 kcal/mol (see Figure S39). The stability of this intermediate is close to the barrier required for C-F activation via S_N1 mechanism and the separate state **[1b]**$^{+}$ + **[BCFF]**$^{-}$. We started the constraint geometry optimisations from **PTol**···**[1b]**$^{+}$···**[BCFF]**$^{-}$ gradually decreasing the P-C distance. The obtained potential energy curve is shown in Figure S58. This computational experiment suggests an ~1.5 kcal/mol barrier need to initiate the P-C bond formation.

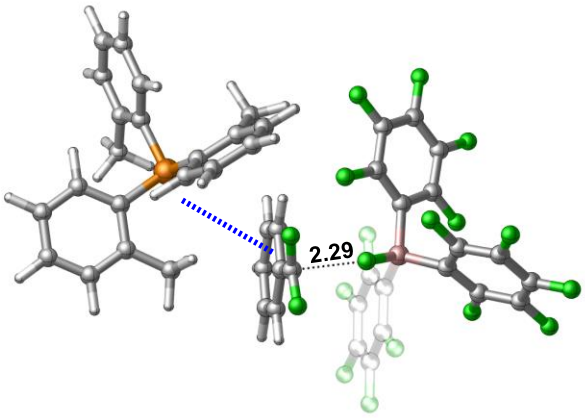

PTol···**[1b]**$^{+}$···**[BCFF]**$^{-}$ (24.5)

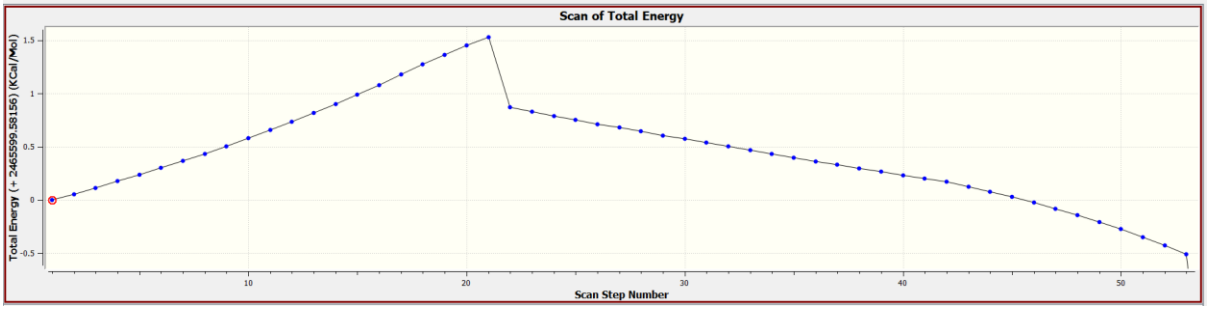

Figure S58. Potential energy curve derived for intermediate **PTol**···**[1b]**$^{+}$···**[BCFF]**$^{-}$ via energy scan calculation between the reactive carbon and P atom.

In parallel with computation with **1b**, we performed a series of transition locations with substrate **2b** as well. Although the transition state corresponding to the most stable conformation was not identified, we found a transition state that relates to the carbocation addition in high-lying intermediate (see Figure S59). This step proceeds via **TS**$^{[2b]+/PTol}$ and we obtained a barrier of 0.9 kcal/mol with respect to the intermediate state. This **PTol**···**[1b]**$^{+}$···**[BCFF]**$^{-}$**-II** intermediate arises form **TS**$^{CHF2/PTol}$**-VI** which was obtained form the conformational analysis. Taken together, these calculations implies that the barrier of the carbocation migration should be within 1.5 kcal/mol.

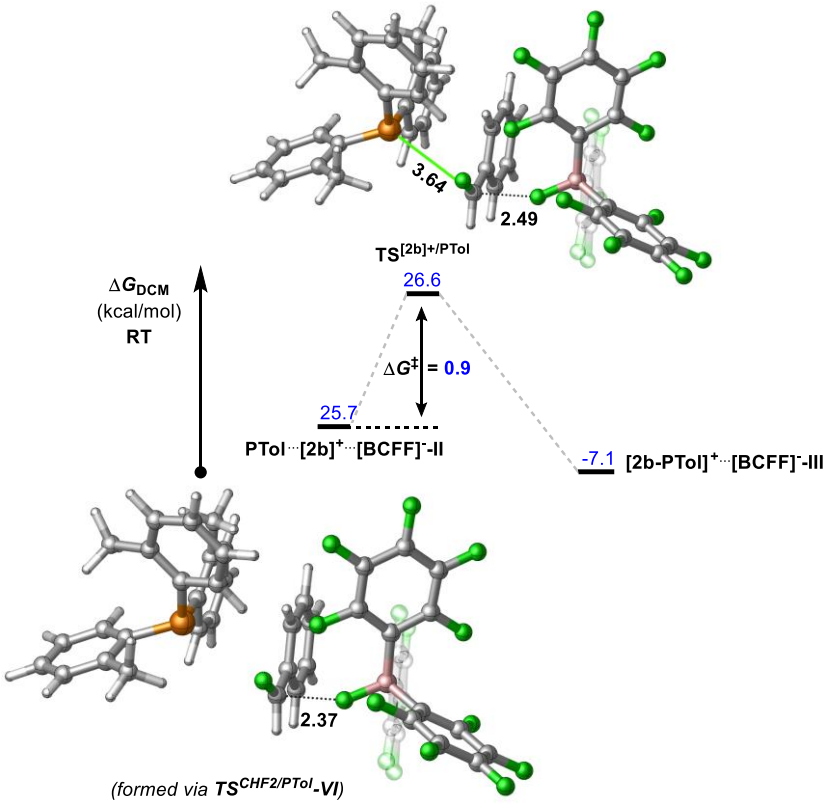

Figure S59. Identified transition state for the addition of carbocation to **PTol**. The relative stability (in blue) is given with respect to **PTol** + **2b** + **BCF** reference state.

As previously mentioned, analogous intermediate in which the sulphur atom points to the reactive carbon centre (originating from transition state of S_N2 process) could not be identified. To give an estimate for such an intermediate, we first calculated the stability of an intermediate where the THT is suited away from the reactive centre. This **THT**···**[1b]**$^+$···**[BCFF]**$^-$intermediate was computed to be 26.2 kcal/mol with respect to the reactant state. Moreover, we also computed the relative free energy of a structure adopted from the IRC calculations to provide an estimate for the energy requirement involved in the formation of **[1b-THT]**$^+$. In this structure, the CF_2H unit is almost planar, similarly to the geometry of the **[1b]**$^+$ in complex the **TPPy**···**[1b]**$^+$···**[BCFF]**$^-$ and **PTol**···**[1b]**$^+$···**[BCFF]**$^-$. Note that this structure is not an energy minimum, but it may approximate free energy needed for these components to assemble. This **THT**···**[1b]**$^+$···**[BCFF]**$^-$**-II** imaginary intermediate is estimated to lie at 25.6 kcal/mol. Overall, the computed barrier heights suggest that the process of the migration of **[1b]**$^+$ to the Lewis base is close to the C-F activation event in free energy.

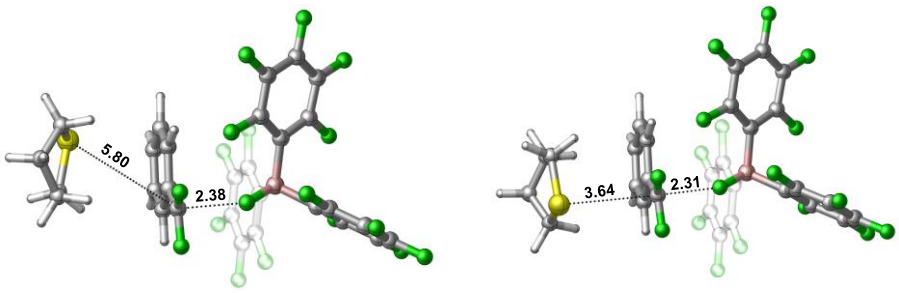

THT···**[1b]$^+$**···**[BCFF]$^-$** (26.2)

THT···**[1b]$^+$**···**[BCFF]$^-$-II** (25.6)
(frozen S-C-F distances)

Figure S60. DFT-optimized structures of possible intermediates after C-F activation. The relative stability (in blue) is given with respect to **THT** + **1b** + **BCF** reference state.

Formation of intermediate 2c-NTf_2

We identified the C-F activation transition state with *o*-Br-substrate **2c** to compare the computed barrier with the experimentally-derived value. The reaction was overly fast with substrate **2b**, as a result, the necessary kinetic measurement could not be executed on that timescale.

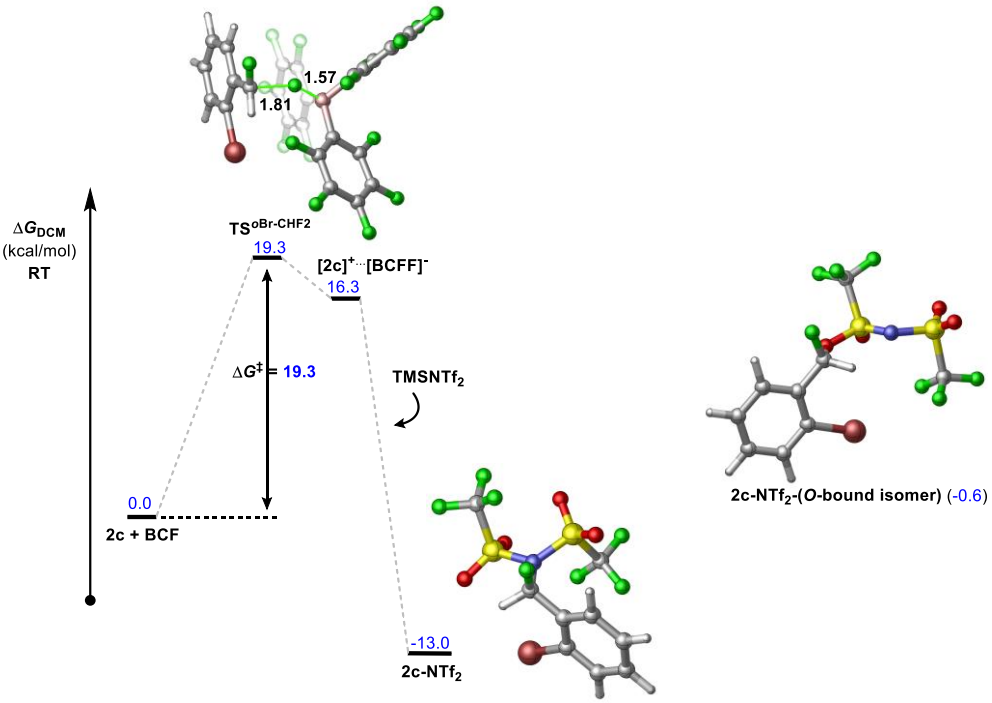

Figure S61. Computed Gibbs free energy profile (Δ*G* in kcal/mol) for substrate **2c** activation via S_N1 mechanism. The relative stability (in blue) is given with respect to **2c** + **BCF + TMSNTf$_2$** reference state.

The second step in the reaction to form [**2c**-LB][NTf_2] (LB = TPPy, PTol, THT) is substitution of NTf_2^- in **2c**-NTf_2 with LB. An S_N1 TS for this reaction was identified at 20.1 kcal mol^{-1} relative to **2c**-NTf_2. However, S_N2 pathways were shown to be much lower in energy (Figure S62), with barriers of 13.7 kcal mol^{-1}, 18.9 kcal mol^{-1} and 15.0 kcal mol^{-1} for S_N2 pathways involving TPPy, PTol and THT respectively.

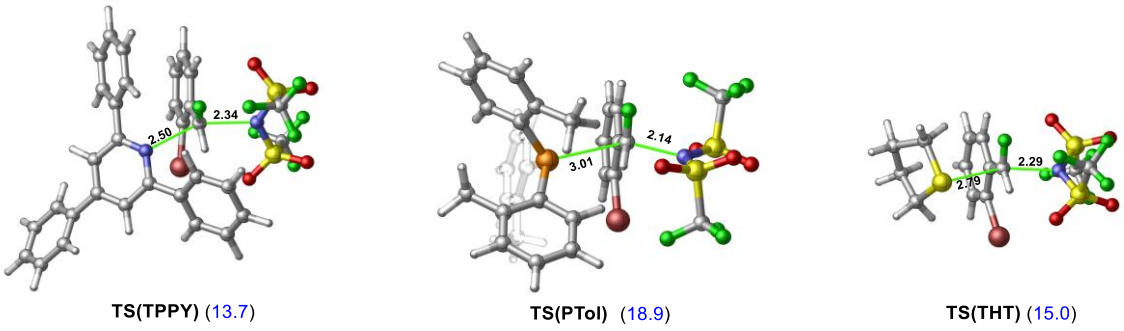

Figure S62. Identified transition states for the substitution of **2c-NTf_2** with Lewis bases. The relative stability (in blue) is given with respect to the reactant state prior to C-F activation.

Activation of 1,4-C_6H_4-$(CF_2H)_2$ (3b) with FLP-I

We also investigated the process of C-F activation in substrate **3b** where the two CHF_2 groups can be activated. The computed energy profile for the double activation with **TPPy** is shown in Figure S63. The reaction starts with the activation of the first CHF_2 group, which proceeds via **TS^{3b}** with a free energy barrier of 19.3 kcal/mol, furnishing the **$[3b]^+\cdots[BCFF]^-$** intermediate (Figure S63). In the next step, the Lewis base enters the reaction mechanism. Once the **$[3b\text{-}TPPy]^+$** is formed, the **$TMSNTf_2$** reacts with **$[BCFF]^-$** anion to regenerate the **BCF**, while forming intermediate **$[3b\text{-}TPPy]^+\cdots[NTf2]^-$**. After the first C-F activation, the resultant intermediate is -21.9 kcal/mol below the reactant state (**3b** + **BCF** + 2 **TPPy +** 2 **$TMSNTf_2$**). We examined several possible orientations of the **$[NTf2]^-$** anion in the **$[3b\text{-}TPPy]^+\cdots[NTf2]^-$** intermediate (Figure S64). The most stable arrangement corresponds to the previously reported crystal structure of **$[1b\text{-}TPPy]^+\cdots[NTf2]^-$**.[14] The subsequent transition state (*i.e.* second C-F activation) was located by using the most stable form of **$[3b\text{-}TPPy]^+\cdots[NTf2]^-$** intermediate. The second C-F activation also appears feasible based on the calculated barrier. The activation barrier represented by **TS^{3b}(TPPy)** is 20.3 kcal/mol, which is similar to the estimated barrier for the first C-F activation (19.3 kcal/mol). Subsequently, the intermediate **$[BCFF]^-\cdots[3b\text{-}TPPy]^{2+}\cdots[NTf2]^-$** reacts with another **TPPy** followed by the **BCF** regeneration with the help of **$TMSNTf_2$**. The overall reaction is highly exergonic (-37.3 kcal/mol).

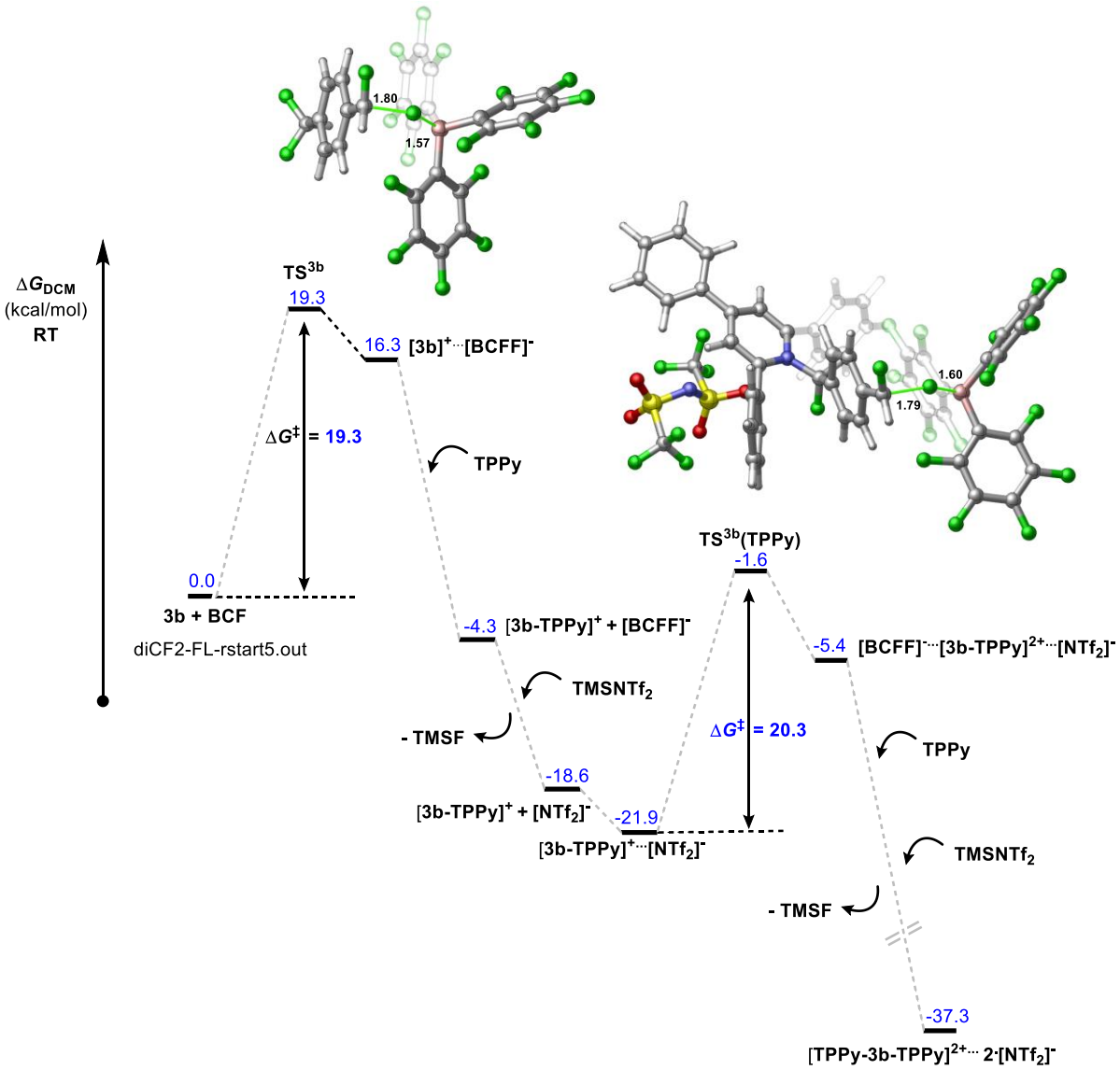

Figure S63. Calculated energy profile for the 1st and 2nd C–F activation of substrate **3b**. The relative stability (in blue) is given with respect to **3b** + **BCF** + 2 **TPPy** + 2 **TMSNTf$_2$**.

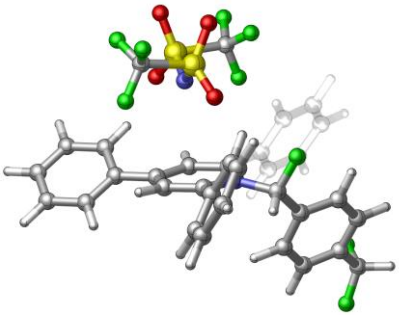

[3b-TPPy]$^{+}$···[NTf$_2$]$^{-}$ (0.0)
conformer corresponding to TS^{3b}(TPPy)

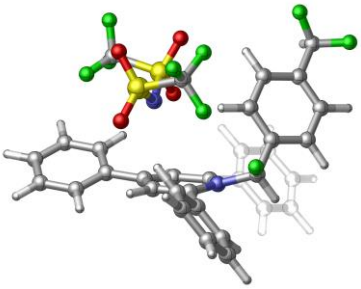

[3b-TPPy]$^{+}$···[NTf$_2$]$^{-}$-II (6.5)

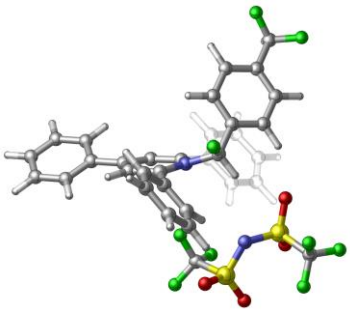

[3b-TPPy]$^{+}$···[NTf$_2$]$^{-}$-III (6.5)

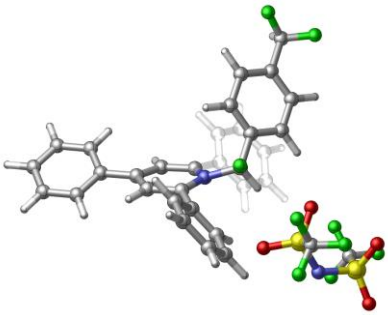

[3b-TPPy]$^{+}$···[NTf$_2$]$^{-}$-IV (8.5)

Figure S64. Various conformers of intermediate **[3b-TPPy]$^{+}$···[NTf2]$^{-}$**. The relative stability (in blue) is given in kcal/mol.

Activation of 1,4-C_6H_4-$(CF_2H)_2$ with FLP-III

Using **THT** as a base, the reaction begins with **TS^{3b}** with a free energy barrier of 19.3 kcal/mol, as is the case with **TPPy**, followed by addition of **$[3b]^+$** to the **THT** (Figure S65). The complex **$[3b\text{-}THT]^+\cdots[NTf2]^-$** wherein the nitrogen atom of $[NTf_2]^-$ binds to the cationic sulphur center is found to be more stable as compared to **$[3b\text{-}THT]^+\cdots[NTf2]^-$-IV** in which O atom coordinates to positive centre (Figure S66). The activation of second C-F bond is kinetically the less favored (**TS^{3b}(THT)** =.23.1 kcal/mol) as its barrier was estimated to be higher than the first C-F activation as well as the analogous **TS^{3b}(TPPy)**. Overall, the formation of the doubly activated product with **THT** is also highly favourable thermodynamically.

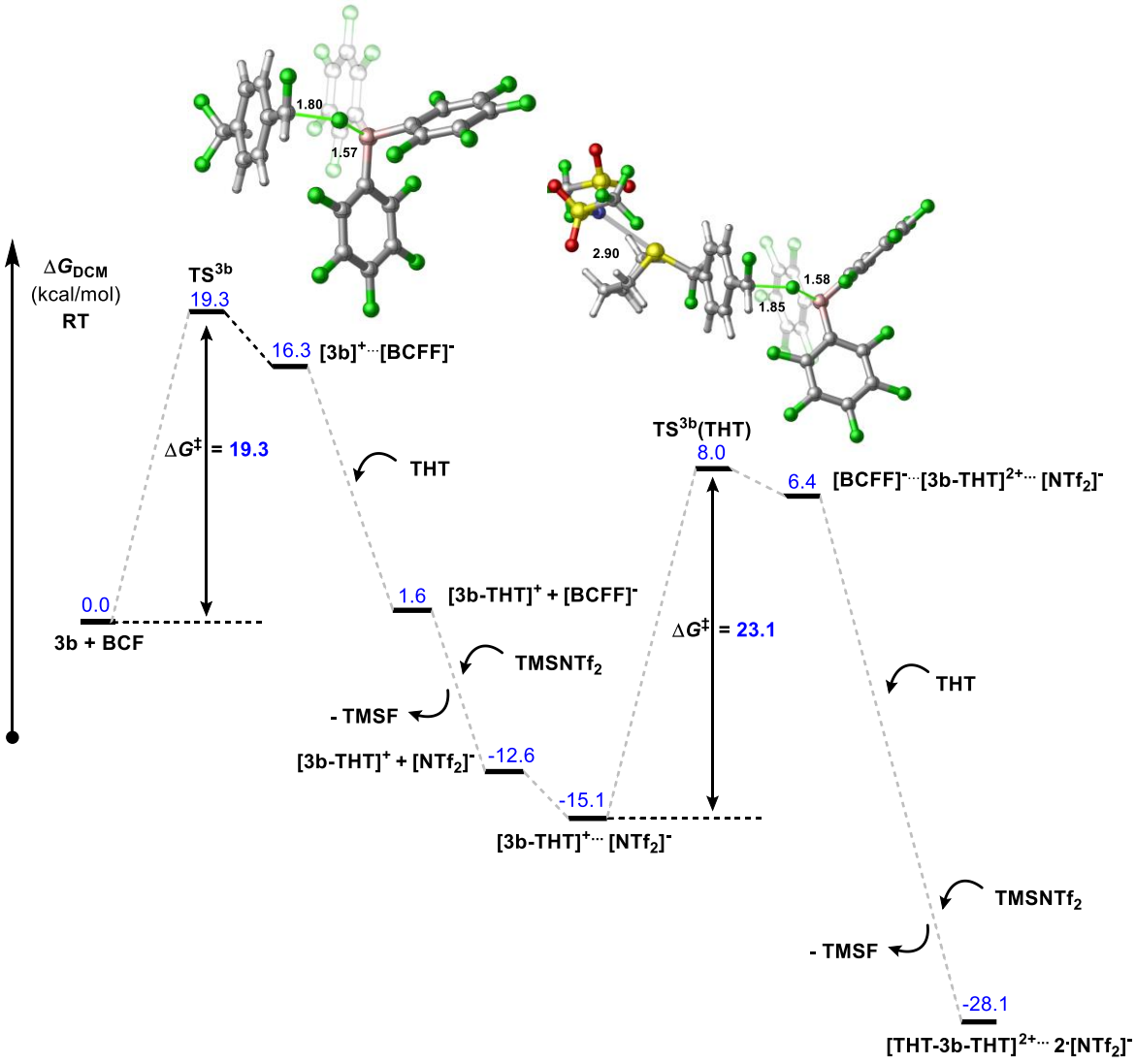

Figure S65. Calculated energy profile for the 1st and 2nd C–F activation of substrate **3b**. The relative stability (in blue) is given with respect to **3b** + **BCF** + 2 **THT** + 2 **$TMSNTf_2$**.

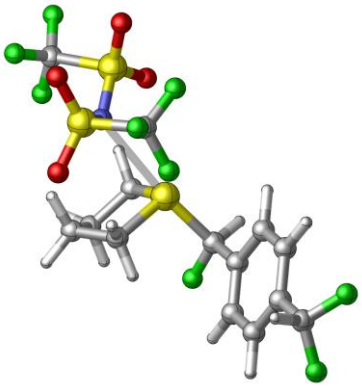

[3b-THT]$^{+}$··· [NTf$_2$]$^{-}$ (0.0)

conformer corresponding to TS^{3b}(THT)

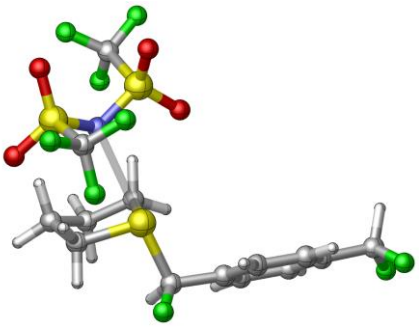

[3b-THT]$^{+}$··· [NTf$_2$]$^{-}$-II (0.6)

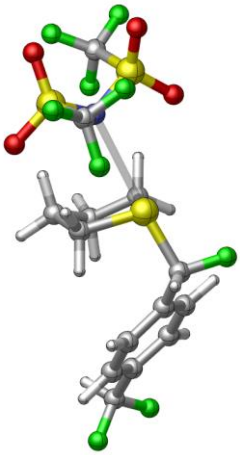

[3b-THT]$^{+}$··· [NTf$_2$]$^{-}$-III (1.7)

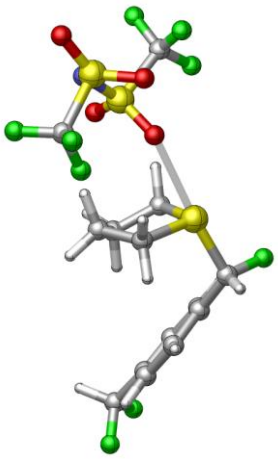

[3b-THT]$^{+}$··· [NTf$_2$]$^{-}$-IV (4.3)

Figure S66. Various conformers of intermediate **[3b-THT]$^{+}$···[NTf2]$^{-}$**. The relative stability (in blue) is given in kcal/mol.

Reactivity difference in double activation

We intend to obtain insights into the origin of the reactivity difference observed for **[3b-THT]**$^+$ and **[3b-TPPy]**$^+$. The free energy change associated with the equation of **[3b-LB]**$^+$ **+ BCF** → **[3b-LB]**$^+$ + **[BCFF]**$^-$ may serve as a measure for differing reactivities. In the case of **TPPy**, we truncated the **TPPy** by systematically removing Ph groups in order to assess the contribution of the arena rings to the stabilization of dications. The stabilization may be effected by either an extended conjugation of the positive charges (Figure S67) or a favorable π-π interaction between the arene ring of the substrate and the *ortho*-Ph of **TPPy** (Figure S68). We argue that these stabilizing effects are present in the transition state **TS^{3b}(TPPy)** leading to a kinetically more favourable C-F bond activation.

The free energy change for **[3b-THT]**$^+$ is 31.5 kcal/mol, which is close to that of **[3b-py]**$^+$. The incorporation of Ph group to *ortho* position appears beneficial to the removal of F anion (by 2.7 kcal/mol). This may be accounted for by a favorable π-π interaction between the arene rings. The computed 1.3 kcal/mol free energy difference between **[3b-*o*Ph-py]**$^+$ and **[3b-TPPy]**$^+$ indicates that possessing additional Ph groups at *para* and *ortho* positions gives rises to further stabilization which is likely to be a result of an extended conjugation of the positive charges.

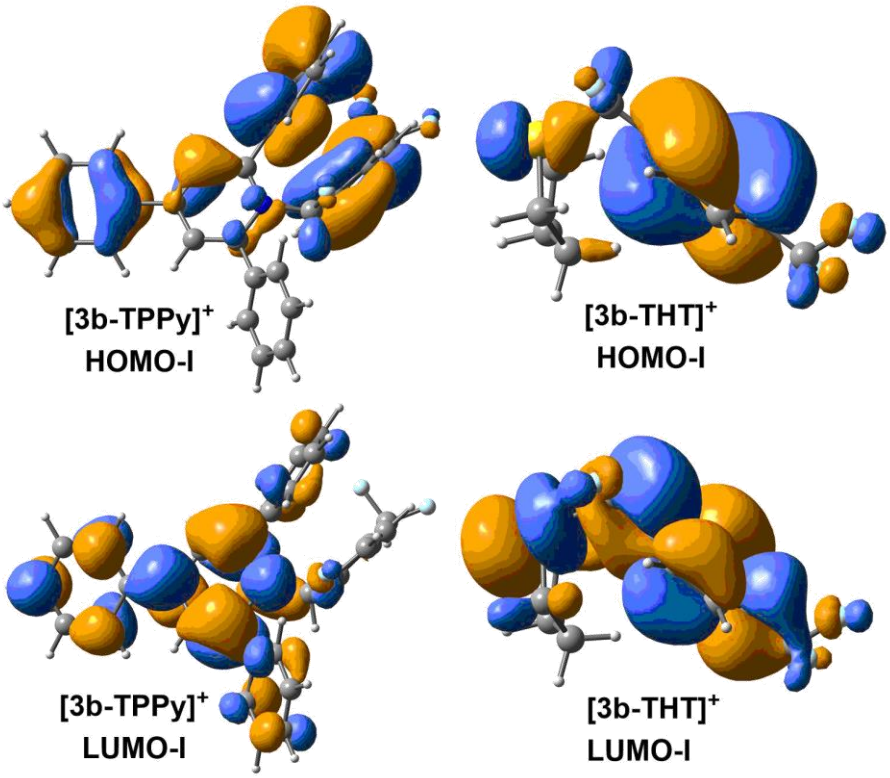

Figure S68. Calculated frontier orbitals for **[3b-TPPy]**$^+$ (left) and **[3b-THT]**$^+$ (right).

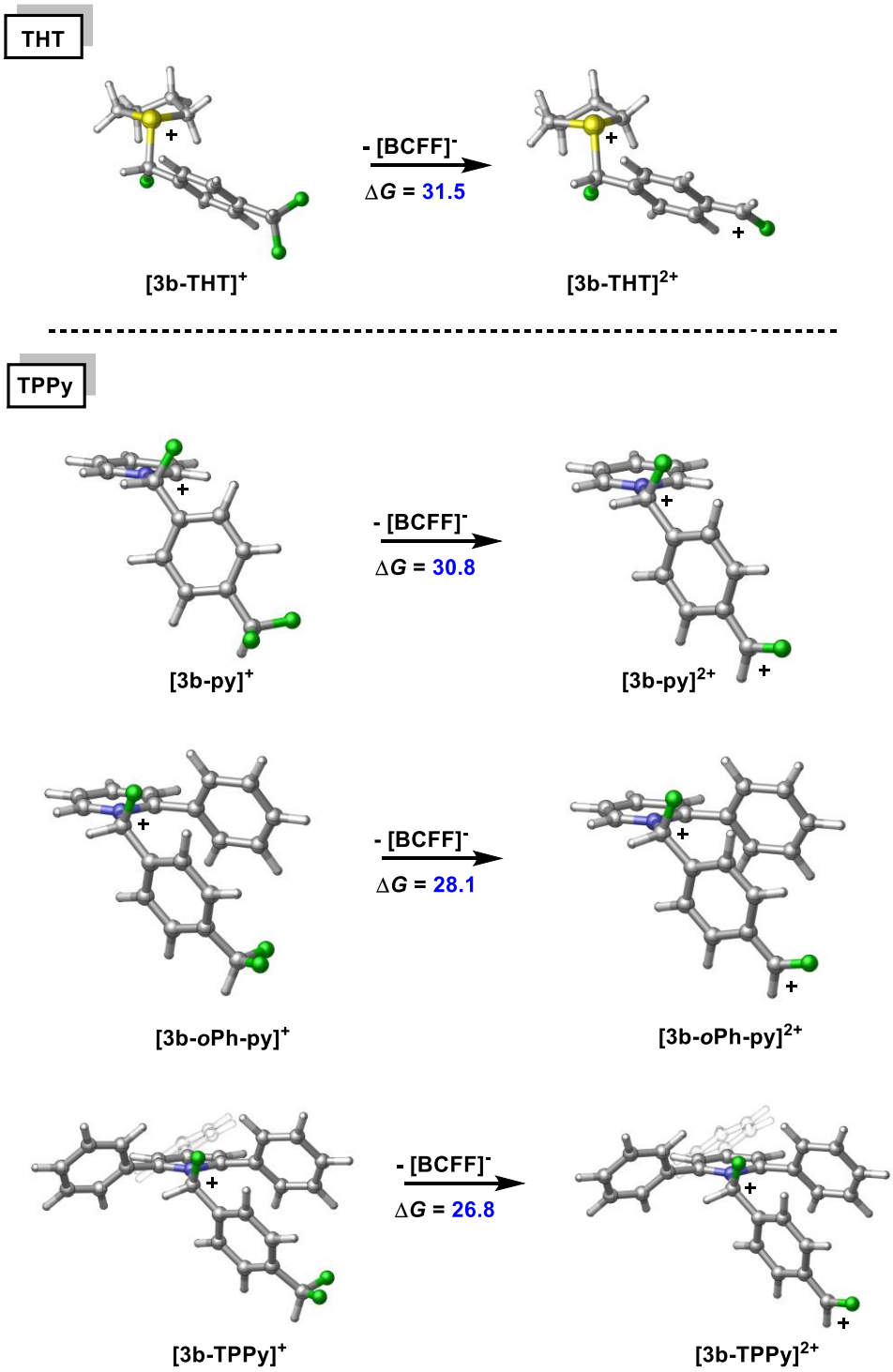

Figure S68. Model reactions for the activation of **[3b-THT]**$^{+}$ and **[3b-TPPy]**$^{+}$ (Δ*G* in kcal/mol).

Double activation of $PhCF_2H$ with FLP-II

Further DFT calculations were performed to elucidate the mechanism of the geminal activation of substrate **2b** (Figure S68). The reaction barrier associated with the geminal C-F bond activation in **[2b-PTol]$^+$** was estimated to be 27.1 kcal/mol, which is 8.2 kcal/mol higher than the barrier for monoactivation. Prior to the C-F bond cleavage, the dissociation of the **[BCFF]$^-$** is necessary to allow BCF to approach the C-F bond, which may otherwise be hindered by the **[BCFF]$^-$** anion. Thus, the presented barrier encompasses the free energy penalty related to dissociation, which is 3.3 kcal/mol (see Figure S48). The activation mechanism is characterized by a transition state **TS$^{CF2''}$** wherein **BCF** abstracts the F anion via S_N1 mechanism. The resultant intermediate **[2b-PTol]$^{2+}$···[BCFF]$^-$** lies at 18.6 kcal/mol above the reactant state (**[2b-PTol]$^+$···[BCFF]$^-$ + BCF**). However, the **[BCFF]$^-$** anion creates a steric hindrance for **PTol** to approach the cationic α-carbon atom in the intermediate **[2b-PTol]$^{2+}$**. Again, the **[BCFF]$^-$** anion is required to be removed to afford a free **[2b-PTol]$^{2+}$** species which is highly reactive due to its strong cationic nature. Hence, the overall barrier height is 29.1 kcal/mol. The elevated temperature may provide sufficient energy for the **[2b-PTol]$^+$···[BCFF]$^-$** to ascend the 29.1 kcal/mol barrier that would allow for the liberation of the **[2-PTol]$^+$**. This cationic intermediate is thus primed for the reaction with an additional **PTol**. Transition state describing the addition of **PTol** could not be identified. The reaction between **[2b-PTol]$^{2+}$** and **PTol** can lead to the formation of multiple products, as show in Figure S68. We observed three possible species, **α -[PTol-2b-PTol]$^{2+}$** wherein the α-carbon was attacked by incoming **PTol**, as well as, the products ***ortho*-[PTol-2b-PTol]$^{2+}$** and ***para*-[PTol-2b-PTol]$^{2+}$** in which the **PTol** reacted with the aryl ring at the ortho and para positions, respectively. Of these products, the ***para*-[PTol-2b-PTol]$^{2+}$** was found to be the most stable, presumably due to the smaller steric congestion, and also the two cationic P atoms are better separated from one another.

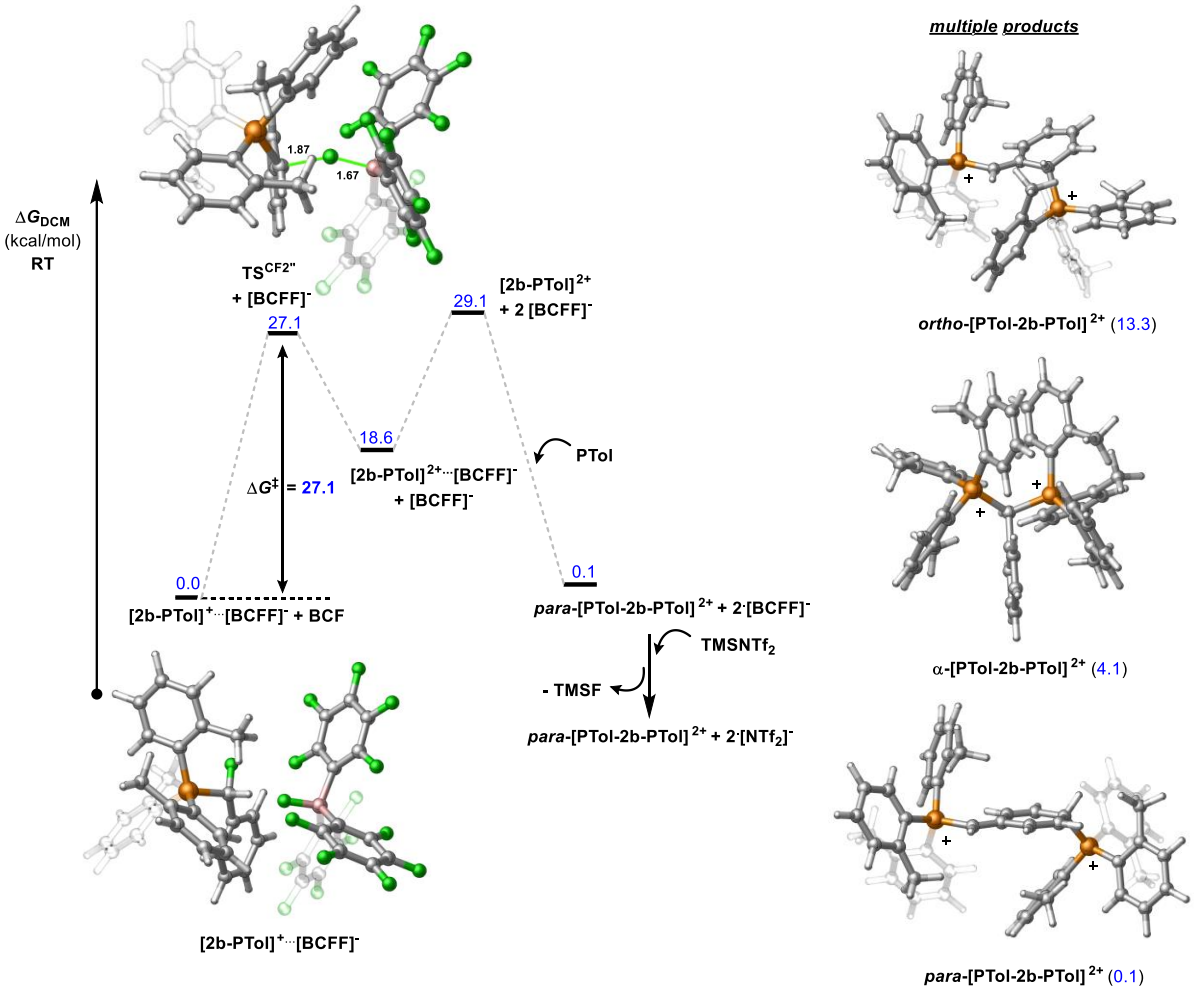

Figure S68. Calculated energy profile for the geminal activation of substrate **2b**. The relative stability (in blue) is given with respect to **[2b-PTol]**$^{+}$···**[BCFF]**$^{-}$ + **BCF**.

Computed energy components of the reported structures.

Table S1**.** Summary of energy data (given in Hartree) computed for optimized structures at the PCM(DCM)- B3LYP-D3/Def2SVP level of theory. Note that G was obtained based on the quasi-harmonic approximation and contains concentration correction. For the definition of various energy components, see Computational details section (above).

Structure	E_0'(DCM)	G^q_0(DCM)	E_0(DCM)	G(DCM)
BCF	-2209.2515	-2206.5544	-2206.6532	-2209.1497
py	-248.3892	-248.0523	-248.1136	-248.3249
BCF-py	-2457.6858	-2454.6352	-2454.8226	-2457.4954
$TS^{CF3/py}$	-3027.1745	-3023.3804	-3023.6589	-3026.8930
1b	-569.5457	-568.8128	-568.8852	-569.4703
TPPy	-941.8453	-940.5463	-940.8332	-941.5554
$TMSNTf_2$	-2237.1539	-2235.1591	-2235.2744	-2237.0355
$TMSNTf_2$-II	-2237.1517	-2235.1550	-2235.2716	-2237.0321
$TMSNTf_2$-III	-2237.1538	-2235.1648	-2235.2837	-2237.0319
TS^{CF3}	-2778.7798	-2775.3369	-2775.5337	-2778.5799
TS^{CF3}-II	-2778.7785	-2775.3362	-2775.5320	-2778.5797
TS^{CF3}-III	-2778.7788	-2775.3354	-2775.5322	-2778.5791
TS^{CF3}-IV	-2778.7777	-2775.3359	-2775.5323	-2778.5782
1b···BCF	-2778.8090	-2775.3648	-2775.5610	-2778.6098
$[1b]^+$···$[BCFF]^-$	-2778.7864	-2775.3413	-2775.5371	-2778.5876
$TS^{CF3/TPPY}$	-3720.6430	-3715.8812	-3716.3911	-3720.1301
$TS^{CF3/TPPY}$-II	-3720.6437	-3715.8838	-3716.3947	-3720.1298
$TS^{CF3/TPPY}$-III	-3720.6436	-3715.8833	-3716.3944	-3720.1295
$TS^{CF3/TPPY}$-IV	-3720.6408	-3715.8816	-3716.3904	-3720.1290
$TS^{CF3/TPPY}$-V	-3720.6428	-3715.8840	-3716.3952	-3720.1287
$TS^{CF3/TPPY}$-VI	-3720.6410	-3715.8823	-3716.3925	-3720.1278
TPPy···1b···BCF	-3720.6727	-3715.9142	-3716.4251	-3720.1588
TPPy···$[1b]^+$···$[BCFF]^-$	-3720.6520	-3715.8887	-3716.3987	-3720.1390
$[1b\text{-}TPPy]^+$	-1411.3055	-1409.3816	-1409.7676	-1410.9165
$[BCFF]^-$	-2309.3491	-2306.5244	-2306.6233	-2309.2472
$[1b\text{-}TPPy]^+$···$[BCFF]^-$	-3720.6902	-3715.9316	-3716.4454	-3720.1735
$[1b\text{-}TPPy]^+$···$[BCFF]^-$-II	-3720.6703	-3715.9074	-3716.4199	-3720.1548
PTol	-1154.6236	-1153.3141	-1153.6249	-1154.3098

$TS^{CF3/PTol}$	-3933.4195	-3928.6487	-3929.1820	-3932.8831
$TS^{CF3/PTol}$-II	-3933.4170	-3928.6438	-3929.1752	-3932.8826
$TS^{CF3/PTol}$-III	-3933.4197	-3928.6483	-3929.1826	-3932.8824
$TS^{CF3/PTol}$-IV	-3933.4192	-3928.6486	-3929.1828	-3932.8820
$TS^{CF3/PTol}$-V	-3933.4184	-3928.6487	-3929.1824	-3932.8818
$TS^{CF3/PTol}$-VI	-3933.4094	-3928.6374	-3929.1718	-3932.8720
PTol···1b···BCF	-3933.4483	-3928.6781	-3929.2114	-3932.9120
PTol···$[1b]^+$···$[BCFF]^-$	-3933.4266	-3928.6529	-3929.1857	-3932.8908
$[1b\text{-}PTol]^+$	-1624.0993	-1622.1595	-1622.5698	-1623.6860
$[1b\text{-}PTol]^+$···$[BCFF]^-$	-3933.4762	-3928.6979	-3929.2350	-3932.9361
$[1b\text{-}PTol]^+$···$[BCFF]^-$-II	-3933.4729	-3928.6965	-3929.2333	-3932.9331
THT	-555.5395	-555.1381	-555.2227	-555.4520
$TS^{CF3/THT}$	-3334.3288	-3330.4667	-3330.7706	-3334.0219
$TS^{CF3/THT}$-II	-3334.3284	-3330.4667	-3330.7704	-3334.0216
$TS^{CF3/THT}$-III	-3334.3281	-3330.4663	-3330.7703	-3334.0211
$TS^{CF3/THT}$-IV	-3334.3280	-3330.4654	-3330.7693	-3334.0210
THT···1b···BCF	-3334.3560	-3330.4926	-3330.7955	-3334.0501
$[1b\text{-}THT]^+$	-1024.9907	-1023.9575	-1024.1380	-1024.8071
$[1b\text{-}THT]^+$···$[BCFF]^-$	-3334.3670	-3330.4938	-3330.7996	-3334.0582
$[1b\text{-}THT]^+$···$[BCFF]^-$-II	-3334.3583	-3330.4854	-3330.7907	-3334.0500
2b	-470.2505	-469.6260	-469.7072	-470.1664
TS^{CHF2}	-2679.4949	-2676.1622	-2676.3681	-2679.2859
TS^{CHF2}-II	-2679.4939	-2676.1604	-2676.3658	-2679.2855
TS^{CHF2}-III	-2679.4923	-2676.1600	-2676.3653	-2679.2840
TS^{CHF2}-IV	-2679.4906	-2676.1588	-2676.3641	-2679.2822
2b···BCF	-2679.5147	-2676.1796	-2676.3852	-2679.3062
$[2b]^+$···$[BCFF]^-$	-2679.4994	-2676.1659	-2676.3693	-2679.2930
$TS^{CHF2/TPPy}$	-3621.3641	-3616.7150	-3617.2369	-3620.8392
$TS^{CHF2/TPPy}$-II	-3621.3607	-3616.7106	-3617.2304	-3620.8379
$TS^{CHF2/TPPy}$-III	-3621.3602	-3616.7112	-3617.2317	-3620.8367
$TS^{CHF2/TPPy}$-IV	-3621.3553	-3616.7056	-3617.2235	-3620.8344
$TS^{CHF2/TPPy}$-V	-3621.3557	-3616.7064	-3617.2263	-3620.8328
$TS^{CHF2/TPPy}$-VI	-3621.3531	-3616.7039	-3617.2228	-3620.8311
$TS^{CHF2/TPPy/H}$-I	-3621.3668	-3616.7215	-3617.2431	-3620.8422

$TS^{CHF2/TPPy/H}$-II	-3621.3668	-3616.7222	-3617.2441	-3620.8418
TPPy···2b···BCF	-3621.3801	-3616.7316	-3617.2519	-3620.8568
TPPy···$[2b]^+$···$[BCFF]^-$	-3621.3689	-3616.7208	-3617.2418	-3620.8449
$[2b\text{-}TPPy]^+$	-1312.0294	-1310.2142	-1310.6099	-1311.6307
$[2b\text{-}TPPy]^+$···$[BCFF]^-$	-3621.4110	-3616.7600	-3617.2859	-3620.8820
$[2b\text{-}TPPy]^+$···$[BCFF]^-$-II	-3621.4038	-3616.7509	-3617.2746	-3620.8772
$TS^{CHF2/PTol}$	-3834.1400	-3829.4807	-3830.0255	-3833.5922
$TS^{CHF2/PTol}$-II	-3834.1371	-3829.4795	-3830.0232	-3833.5904
$TS^{CHF2/PTol}$-III	-3834.1351	-3829.4742	-3830.0176	-3833.5888
$TS^{CHF2/PTol}$-IV	-3834.1356	-3829.4769	-3830.0214	-3833.5882
$TS^{CHF2/PTol}$-V	-3834.1281	-3829.4671	-3830.0102	-3833.5820
$TS^{CHF2/PTol}$-VI	-3834.1216	-3829.4592	-3830.0026	-3833.5753
PTol···2b···BCF	-3834.1579	-3829.4975	-3830.0403	-3833.6121
PTol···$[2b]^+$···$[BCFF]^-$	-3834.1421	-3829.4790	-3830.0203	-3833.5977
$[2b\text{-}PTol]^+$	-1524.8203	-1522.9901	-1523.4095	-1524.3978
$[2b\text{-}PTol]^+$···$[BCFF]^-$	-3834.2005	-3829.5327	-3830.0800	-3833.6502
$[2b\text{-}PTol]^+$···$[BCFF]^-$-II	-3834.1913	-3829.5230	-3830.0706	-3833.6407
$TS^{CHF2/THT}$	-3235.0457	-3231.2935	-3231.6068	-3234.7294
$TS^{CHF2/THT}$-II	-3235.0449	-3231.2933	-3231.6064	-3234.7288
$TS^{CHF2/THT}$-III	-3235.0447	-3231.2916	-3231.6048	-3234.7285
$TS^{CHF2/THT}$-IV	-3235.0430	-3231.2903	-3231.6036	-3234.7267
THT···2b···BCF	-3235.0641	-3231.3099	-3231.6228	-3234.7482
$[1b\text{-}THT]^+$	-925.7082	-924.7858	-924.9754	-925.5156
$[2b\text{-}THT]^+$···$[BCFF]^-$	-3235.0850	-3231.3245	-3231.6389	-3234.7675
$[2b\text{-}THT]^+$···$[BCFF]^-$-II	-3235.0836	-3231.3221	-3231.6364	-3234.7663
$[BCF\text{-}F\text{-}TMSNTf2]^-$	-4546.5161	-4541.6803	-4541.9224	-4546.2710
1a	-608.8814	-608.0812	-608.1775	-608.7822
1a···BCF	-2818.1459	-2814.6342	-2814.8562	-2817.9208
TS^{1a}	-2818.1184	-2814.6080	-2814.8305	-2817.8930
$[1a]^+$···$[BCFF]^-$	-2818.1287	-2814.6146	-2814.8366	-2817.9037
TPPy···1a···BCF	-3760.0105	-3755.1840	-3755.7216	-3759.4699
$TS^{1a/TPPy}$	-3759.9817	-3755.1533	-3755.6899	-3759.4420
TPPy···$[1a]^+$···$[BCFF]^-$	-3759.9946	-3755.1627	-3755.6989	-3759.4554
$[1a\text{-}TPPy]^+$	-1450.6419	-1448.6497	-1449.0606	-1450.2279

[1a-TPPy]$^{+}$···[BCFF]$^{-}$	-3760.0268	-3755.2000	-3755.7400	-3759.4838
PTol···1a···BCF	-3972.7855	-3967.9476	-3968.5067	-3972.2234
TS$^{1a/PTol}$	-3972.7587	-3967.9204	-3968.4792	-3972.1968
PTol···[1a]$^{+}$···[BCFF]$^{-}$	-3972.7701	-3967.9283	-3968.4865	-3972.2089
[1a-PTol]$^{+}$	-1663.4357	-1661.4276	-1661.8629	-1662.9974
[1a-PTol]$^{+}$···[BCFF]$^{-}$	-3972.8125	-3967.9657	-3968.5280	-3972.2472
THT···1a···BCF	-3373.6931	-3369.7621	-3370.0907	-3373.3615
TS$^{1a/THT}$	-3373.6674	-3369.7379	-3370.0672	-3373.3351
[1a-THT]$^{+}$	-1064.3275	-1063.2262	-1063.4316	-1064.1191
[1a-THT]$^{+}$···[BCFF]$^{-}$	-3373.7036	-3369.7623	-3370.0928	-3373.3700
BnF	-370.9582	-370.4474	-370.5370	-370.8656
TS^{CH2F}	-2580.2100	-2576.9881	-2577.2014	-2579.9937
[Bn-TPPy]$^{+}$	-1425.5541	-1423.8337	-1424.2614	-1425.1234
[Bn-TPPy]$^{+}$···[BCFF]$^{-}$	-3734.9326	-3730.3753	-3730.9319	-3734.3730
BCF-TPPy	-3151.1096	-3147.0984	-3147.5162	-3150.6889
BCF-TPPy'	-3151.1167	-3147.1090	-3147.5223	-3150.7003
BCF-TPPy'-II	-3151.1171	-3147.1088	-3147.5232	-3147.5232
BCF-TPPy'-III	-3151.1159	-3147.1084	-3147.5220	-3150.6993
BCF-TPPy'-IV	-3151.1158	-3147.1064	-3147.5202	-3150.6990
BCF-TPPy'-V	-3151.1153	-3147.1072	-3147.5214	-3150.6981
BCF-TPPy'-VI	-3151.1145	-3147.1054	-3147.5194	-3150.6975
BCF-PTol	-3363.8971	-3359.8727	-3360.3123	-3363.4544
BCF-PTol-II	-3363.8911	-3359.8669	-3360.3083	-3363.4467
BCF-PTol'	-3363.8968	-3359.8781	-3360.3147	-3363.4572
BCF-PTol'-II	-3363.8943	-3359.8777	-3360.3133	-3363.4557
BCF-PTol'-III	-3363.8945	-3359.8740	-3360.3101	-3363.4553
BCF-PTol'-IV	-3363.8940	-3359.8740	-3360.3102	-3363.4548
BCF-PTol'-V	-3363.8921	-3359.8743	-3360.3102	-3363.4532
BCF-PTol'-VI	-3363.8910	-3359.8733	-3360.3097	-3363.4516
BCF-THT	-2764.8160	-2761.7013	-2761.9112	-2764.6031
BCF-THT-II	-2764.8151	-2761.7001	-2761.9096	-2764.6026
BCF-THT-III	-2764.8151	-2761.7001	-2761.9096	-2764.6025
BCF-THT-IV	-2764.8099	-2761.6976	-2761.9046	-2764.5999
BCF-THT-V	-2764.8099	-2761.6946	-2761.9046	-2764.5969
TS$^{CF3/TMSNTf2}$	-2806.6723	-2803.9201	-2804.1320	-2806.4574

$TS^{CF3/TMSNTf2}$-II	-2806.6721	-2803.9199	-2804.1318	-2806.4572
$TS^{CF3/TMSNTf2}$-III	-2806.6713	-2803.9192	-2804.1309	-2806.4566
$TS^{CHF2/TMSNTf2}$	-2707.3852	-2704.7425	-2704.9632	-2707.1615
$TS^{CHF2/TMSNTf2}$-II	-2707.3847	-2704.7426	-2704.9633	-2707.1611
$TS^{CHF2/TMSNTf}$-III	-2707.3841	-2704.7411	-2704.9623	-2707.1600
$TS^{CHF2/TMSNTf2}$-IV	-2707.3842	-2704.7450	-2704.9664	-2707.1598
$TS^{CHF2/TMSNTf2}$-V	-2707.3842	-2704.7437	-2704.9653	-2707.1596
$TS^{[1b]+/TPPy}$	-3720.6498	-3715.8852	-3716.3964	-3720.1356
$[1b]^+$	-469.4079	-468.8006	-468.8718	-469.3337
PTol···$[2b]^+$···$[BCFF]^-$-II	-3834.1289	-3829.4656	-3830.0066	-3833.5850
$TS^{[2b]+/PTol}$	-3834.1292	-3829.4640	-3830.0066	-3833.5835
$[2b\text{-}PTol]^+$···$[BCFF]^-$-III	-3834.1878	-3829.5224	-3830.0699	-3833.6373
THT···$[1b]^+$···$[BCFF]^-$	-3334.3362	-3330.4704	-3330.7733	-3334.0303
THT···$[1b]^+$···$[BCFF]^-$-II	-3334.3367	-3330.4711	-3330.7737	-3334.0312
2c	-3043.8290	-3042.9065	-3042.9754	-3043.7571
TS^{SN1}	-5253.0721	-5249.4408	-5249.6339	-5252.8760
$[2c]^+$···$[BCFF]^-$	-5253.0761	-5249.4433	-5249.6355	-5252.8808
2c-NTf_2	-4771.6832	-4769.2279	-4769.3356	-4771.5726
2c-NTf_2-II	-4771.6609	-4769.2000	-4769.3050	-4771.5529
TS(TPPY)	-5713.5285	-5709.7413	-5710.1607	-5713.1062
TS(PTol)	-5926.2981	-5922.5018	-5922.9446	-5925.8523
TS(THT)	-5327.2162	-5324.3280	-5324.5406	-5327.0007
$[2c\text{-}TPPy]^+$	-3885.5999	-3883.4849	-3883.8687	-3885.2132
$[2c\text{-}PTol]^+$	-4098.3964	-4096.2668	-4096.6751	-4097.9851
$[2c\text{-}THT]^+$	-3499.2888	-3498.0703	-3498.2472	-3499.1088
3b	-708.1519	-707.2318	-707.3224	-708.0583
TS^{3b}	-2917.3962	-2913.7676	-2913.9835	-2917.1773
$[3b]^+$···$[BCFF]^-$	-2917.3995	-2913.7704	-2913.9848	-2917.1821
$[3b\text{-}TPPy]^+$	-1549.9314	-1547.8197	-1548.2251	-1549.5231
$[3b\text{-}TPPy]^+$···$[NTf2]^-$	-3377.8912	-3374.1049	-3374.5498	-3377.4433
$[3b\text{-}TPPy]^+$···$[NTf2]^-$-II	-3377.8816	-3374.0995	-3374.5452	-3377.4329
$[3b\text{-}TPPy]^+$···$[NTf2]^-$-III	-3377.8790	-3374.0925	-3374.5356	-3377.4329
$[3b\text{-}TPPy]^+$···$[NTf2]^-$-IV	-3377.8759	-3374.0889	-3374.5321	-3377.4297
TS^{3b}(TPPy)	-5587.1351	-5580.6420	-5581.2135	-5586.5606
$[BCFF]^-$···$[3b\text{-}TPPy]^{2+}$···$[NTf2]^-$	-5587.1403	-5580.6458	-5581.2164	-5586.5667

[TPPy-3b-TPPy]$^{2+}$···2·[NTf2]$^{-}$	-6047.6230	-6040.9699	-6041.7719	-6046.8180
[3b-THT]$^{+}$	-1163.6112	-1162.3938	-1162.5919	-1163.4101
[3b-THT]$^{+}$···[NTf2]$^{-}$	-2991.5676	-2988.6760	-2988.9115	-2991.3291
[3b-THT]$^{+}$···[NTf2]$^{-}$-II	-2991.5661	-2988.6721	-2988.9070	-2991.3282
[3b-THT]$^{+}$···[NTf2]$^{-}$-III	-2991.5650	-2988.6701	-2988.9056	-2991.3265
[3b-THT]$^{+}$···[NTf2] -IV	-2991.5609	-2988.6639	-2988.8995	-2991.3222
TS^{3b}(THT)	-5200.8073	-5195.2066	-5195.5690	-5200.4419
[BCFF]$^{-}$···[3b-THT]$^{2+}$···[NTf2]$^{-}$	-5200.8095	-5195.2079	-5195.5698	-5200.4446
[THT-3b-THT]$^{2+}$···2·[NTf2]$^{-}$	-5274.9829	-5270.1174	-5270.5006	-5274.5966
[3b-THT]$^{2+}$	-1063.4619	-1062.3720	-1062.5685	-1063.2625
[3b-py]$^{+}$	-856.4802	-855.3310	-855.5079	-856.3003
[3b-py]$^{2+}$	-756.3315	-755.3108	-755.4856	-756.1537
[3b-oPh-py]$^{+}$	-1087.6281	-1086.1593	-1086.4130	-1087.3714
[3b-oPh-py]$^{+}$	-987.4839	-986.1421	-986.3940	-987.2290
[3b-TPPy]$^{2+}$	-1449.7897	-1447.8046	-1448.2084	-1449.3829
TS$^{CF2"}$	-3734.0589	-3729.5160	-3730.0623	-3733.5096
[2b-PTol]$^{2+}$···[BCFF]$^{-}$	-3734.0699	-3729.5255	-3730.0693	-3733.5231
[2b-PTol]$^{2+}$	-1424.6776	-1422.9687	-1423.3842	-1424.2591
***para*-[PTol-2b-PTol]$^{2+}$**	-2579.3772	-2576.3293	-2577.0883	-2578.6151
***α*-[PTol-2b-PTol]$^{2+}$**	-2579.3740	-2576.3275	-2577.0897	-2578.6088
***ortho*-[PTol-2b-PTol]$^{2+}$**	-2579.3667	-2576.3103	-2577.0799	-2578.5941

Table S2. Comparison of energies obtained using different computational methods.

Computational methods				
Structure	E_0'(DCM)	$G^q{}_0$(DCM)	E_0(DCM)	G(DCM)
PCM-B3LYP-D3(BJ)/Def2TZVPP//SMD-B3LYP-D3(BJ)//Def2SVP				
1b$^{GD3BJ/PCM}$	-569.5615 -569.3223 -569.3565	-568.8285	-568.9009	-569.4862 -569.2469 -569.2811
BCF$^{GD3BJ/PCM}$	-2209.2967 -2208.4766 -2208.5595	-2206.5992	-2206.6980	-2209.1948 -2208.3747 -2208.4576
TPPy$^{GD3BJ/PCM}$	-941.9064 -941.4119 -941.4662	-940.6070	-940.8942	-941.6162 -941.1217 -941.1760
TS$^{GD3BJ/PCM}$**-1**	-3720.7627 -3719.2040 -3719.3769	-3716.0023	-3716.5136	-3720.2485 -3718.6898 -3718.8627
TS$^{GD3BJ/PCM}$**-2**	-2778.8391 -2777.7777 -2777.8936	-2775.3965	-2775.5924	-2778.6401 -2777.5787 -2777.6946
SMD-B3LYP-D3/Def2TZVPP//SMD-B3LYP-D3/Def2SVP				
1b$^{GD3/SMD}$	-569.5521 -569.3287 -569.3627	-568.8190	-568.8912	-569.4769 -569.2535 -569.2875
BCF$^{GD3/SMD}$	-2209.2560 -2208.4805 -2208.5626	-2206.5584	-2206.6572	-2209.1541 -2208.3786 -2208.4608
TPPy$^{GD3/SMD}$	-941.8686 -941.4354 -941.4894	-940.5688	-940.8559	-941.5785 -941.1454 -941.1994
TS$^{GD3/SMD}$**-1**	-3720.6707 -3719.2335 -3719.4065	-3715.9099	-3716.4206	-3720.1571 -3718.7198 -3718.8929
TS$^{GD3/SMD}$**-2**	-2778.7880 -2777.7862 -2777.9019	-2775.3450	-2775.5409	-2778.5890 -2777.5872 -2777.7029

SMD-B3LYP-D3(BJ)/Def2TZVPP//SMD-B3LYP-D3(BJ)/Def2SVP				
1b$^{GD3BJ/SMD}$	-569.5679 -569.3288 -569.3629	-568.8346	-568.9069	-569.4926 -569.2536 -569.2876
BCF$^{GD3BJ/SMD}$	-2209.3012 -2208.4808 -2208.5634	-2206.6031	-2206.7020	-2209.1993 -2208.3789 -2208.4615
TPPy$^{GD3BJ/SMD}$	-941.9299 -941.4363 -941.4903	-940.6292	-940.9170	-941.6392 -941.1455 -941.1995
TS$^{GD3BJ/SMD}$**-1**	-3720.7927 -3719.2346 -3719.4074	-3716.0310	-3716.5421	-3720.2786 -3718.7205 -3718.8932
TS$^{GD3BJ/SMD}$**-2**	-2778.8478 -2777.7875 -2777.9023	-2775.4047	-2775.6017	-2778.6477 -2777.5875 -2777.7023

References

(1) A. G. Massey, A. J. Park, *J. Organometal. Chem*. **1964**, *2*, 245.

(2) X. Zhang, Z. Wang, K. Xu, Y. Feng, W. Zhao, X. Xu, Y. Yan, W. Yi, *Green Chem.* **2016**, *18*, 2313.

(3) (a) W. J. Middleton, *J. Org. Chem*. **1975**, *40*, 574; (b) M. Hudlicky, Organic Reaction: Fluorination with Diethylaminosulfur Trifluoride and Related Aminofluorosulfuranes, Wiley: Hoboken, **1988**, *35*, 513; (c) F. Pan, B. G. Boursalian, T. Ritter, *Angew. Chem. Int. Ed.* **2018**, *57*, 16871.

(4) Gaussian 16, Revision A.03, M. J. Frisch, G. W. Trucks, H. B. Schlegel, G. E. Scuseria, M. A. Robb, J. R. Cheeseman, G. Scalmani, V. Barone, G. A. Petersson, H. Nakatsuji, X. Li, M. Caricato, A. V. Marenich, J. Bloino, B. G. Janesko, R. Gomperts, B. Mennucci, H. P. Hratchian, J. V. Ortiz, A. F. Izmaylov, J. L. Sonnenberg, D. Williams-Young, F. Ding, F. Lipparini, F. Egidi, J. Goings, B. Peng, A. Petrone, T. Henderson, D. Ranasinghe, V. G. Zakrzewski, J. Gao, N. Rega, G. Zheng, W. Liang, M. Hada, M. Ehara, K. Toyota, R. Fukuda, J. Hasegawa, M. Ishida, T. Nakajima, Y. Honda, O. Kitao, H. Nakai, T. Vreven, K. Throssell, J. A. Montgomery, Jr., J. E.

Peralta, F. Ogliaro, M. J. Bearpark, J. J. Heyd, E. N. Brothers, K. N. Kudin, V. N. Staroverov, T. A. Keith, R. Kobayashi, J. Normand, K. Raghavachari, A. P. Rendell, J. C. Burant, S. S. Iyengar, J. Tomasi, M. Cossi, J. M. Millam, M. Klene, C. Adamo, R. Cammi, J. W. Ochterski, R. L. Martin, K. Morokuma, O. Farkas, J. B. Foresman, and D. J. Fox, Gaussian, Inc., Wallingford CT, 2016.

(5) A. D. Becke, *J. Chem. Phys*. **1993**, *98*, 5648.

(6) a) S. Grimme, J. Antony, S. Ehrlich, H. Krieg, *J. Chem. Phys*. **2010**, *132.*, 154104. b) M. Bursch, E. Caldeweyherm, A. Hansen, H. Neugebauer, S. Ehlert, S. Grimme, *Acc. Chem. Res*. **2019**, *52*, 258.

(7) a) S. Miertusˇ, E. Scrocco, J. Tomasi, *Chem. Phys*. **1981**, *55*, 117.; b) J. L. Pascual-Ahuir, E. Silla, I. Tuñon, *J. Comput. Chem*. **1994**, *15*, 1127; c)V.Barone, M. Cossi, *J. Phys. Chem. A* **1998**, *102*, 1995.

(8) S. Grimme, *Chem - A Eur J*. **2012**, *18*, 9955.

(9) G. Luchini, J. V. Alegre-Requena, I. Funes-Ardoiz, R. S. Paton, *F1000Research*, **2020**, *9*, 291.

(10) F. Weigend, R. Ahlrichs, *Phys. Chem. Chem. Phys.* **2005**, *7*, 3.

(11) Y. Zhao, D. G. Truhlar, *Theor. Chem. Acc.* **2008**, *120*, 215.

(12) a) J.-D. Chai, M. Head-Gordon, *Phys. Chem. Chem. Phys*. **2008**, *10*, 6615; b) J.-D. Chai, M. Head-Gordon, *J. Chem. Phys.* **2008**, *128*, 084106.

(13) MacroModel; Schrödinger, LLC: New York, NY, 2017.

(14) D. Mandal, R. Gupta, A. K. Jaiswal, R. D. Young, *J. Am. Chem. Soc.* **2020**, *142*, 2572.